DYNAMICS AND CONTROL OF SMART STRUCTURES FOR SPACE APPLICATIONS

RYAN R. ORSZULIK

A DISSERTATION SUBMITTED TO THE FACULTY OF GRADUATE STUDIES
IN PARTIAL FULFILMENT OF THE REQUIREMENTS
FOR THE DEGREE OF

DOCTOR OF PHILOSOPHY

GRADUATE PROGRAM IN EARTH AND SPACE SCIENCE
YORK UNIVERSITY
TORONTO, ONTARIO
NOVEMBER 2013

Abstract

Smart materials are one of the key emerging technologies for a variety of space systems ranging in their applications from instrumentation to structural design. The underlying principle of smart materials is that they are materials that can change their properties based on an input, typically a voltage or current. When these materials are incorporated into structures, they create smart structures. This work is concerned with the dynamics and control of three smart structures: a membrane structure with shape memory alloys for control of the membrane surface flatness, a flexible manipulator with a collocated piezoelectric sensor/actuator pair for active vibration control, and a piezoelectric nanopositioner for control of instrumentation.

Shape memory alloys are used to control the surface flatness of a prototype membrane structure. As these actuators exhibit a hysteretic nonlinearity, they need their own controller to operate as required. The membrane structures surface flatness is then controlled by the shape memory alloys, and two techniques are developed:

genetic algorithm and proportional-integral controllers. This would represent the removal of one of the main obstacles preventing the use of membrane structures in space for high precision applications, such as a C-band synthetic aperture radar antenna.

Next, an adaptive positive position feedback law is developed for control of a structure with a collocated piezoelectric sensor/actuator pair, with unknown natural frequencies. This control law is then combined with the input shaping technique for slew maneuvers of a single-link flexible manipulator. As an alternative to the adaptive positive position feedback law, genetic algorithms are investigated as both system identification techniques and as a tool for optimal controller design in vibration suppression. These controllers are all verified through both simulation and experiments.

The third area of investigation is on the nonlinear dynamics and control of piezoelectric actuators for nanopositioning applications. A state feedback integral plus double integral synchronization controller is designed to allow the piezoelectrics to form the basis of an ultra-precise 2-D Fabry-Perot interferometer as the gap spacing of the device could be controlled at the nanometer level. Next, an output feedback linear integral control law is examined explicitly for the piezoelectric actuators with its nonlinear behaviour modeled as an input nonlinearity to a linear system. Conditions for asymptotic stability are established and then the analysis is extended to

the derivation of an output feedback integral synchronization controller that guarantees global asymptotic stability under input nonlinearities. Experiments are then performed to validate the analysis.

In this work, the dynamics and control of these smart structures are addressed in the context of their three applications. The main objective of this work is to develop effective and reliable control strategies for smart structures that broaden their applicability to space systems.

This thesis is dedicated to my family

Acknowledgements

To begin, I must thank Prof. Shan for taking me on as a graduate student, and for his advice to continue on and pursue a doctorate. He has always been willing to help and provide advice on any problem, and whose enthusiasm for research has kept me focused and motivated throughout. His push to publish, and firm belief in supporting students to attend conferences, has been greatly appreciated. The freedom he granted to pursue research topics of interest, even if they did not turn out, has turned me into a much better researcher.

I would also like to thank Prof. Zhu and Prof. Quine, for serving on my advisory committee. Our yearly meetings have provided valuable feedback and advice that has substantially improved the quality of this dissertation. I must also thank Prof. Zhu for the many reference letters he has written me over the years, as his endorsement has helped to ease the financial burden of graduate school.

To my many labmates over the years, Piotr, Mike, Ampere, Xiaogang, Yuan, Lei, Yanfang, Liu, Inseon, and Shawn, it has been fun (and educational). In par-

ticular, I would like to express my thanks to Lei, with whom I have had many conversations on the theory of control, in particular on what is typically hidden behind its mathematics.

I must also gratefully acknowledge my family, my mom and dad, Marilyn and Derek, and my sisters, Shannon and Megan, who have always encouraged me to reach for the stars (pun fully intended) while keeping me grounded. Finally, I must express my thanks to Joanne, for her patience (and feigned interest) as I go on about my work, particularly after days when things have not turned out as planned.

Table of Contents

List of Tables

List of Figures

1 Introduction

Smart materials are materials that are capable of changing their properties in a controlled fashion, typically based on a supplied input. These types of materials can be incorporated into structures to create smart, or intelligent, structures capable of sensing and reacting to changes in their operating environment. A sensor is used to monitor the system and its output is connected to a control unit which will generate a response to the sensor signal, which is then applied to the actuator to generate a desired system behaviour. There are many forms of smart materials including shape memory alloys, piezoelectrics, magnetorheological and electrorheological fluids, and magenetostrictives and electrostrictives. The possibility to change a materials property in a controlled fashion is fascinating and has found applications in a diverse number of fields including positioning, shape and vibration control, and fault detection and mitigation [1]. Within the space sector, as more is demanded of systems in increasingly complex applications in harsh environments, smart materials present themselves as one of the most viable solutions to

these engineering problems. Past, current, and future space applications of smart materials, in particular of piezoelectrics and shape memory alloys, are outlined briefly below.

Piezoelectric materials can operate as sensors via the direct piezoelectric effect whereby a voltage is generated when the material is strained. They can also operate as actuators through the converse piezoelectric effect whereby they generate strain when a voltage is applied. With proper instrumentation, they can also be used in applications that require them to operate as both sensors and actuators simultaneously. For actuation, they possess the desired qualities of high resolution, fast response time, large force output, and easy integration into structures, as they can either be embedded into the structure during the fabrication process, or bonded to it afterwards [2].

The direct piezoelectric effect is used for sensing in a variety of applications through their implementations as accelerometers and pressure sensors. For example, Meggitt PLC designed the vibration sensors for the Ariane 5 main and second engine stages. Multiple piezoelectric sensors can also be used on distributed systems for health monitoring of complex structures [3]. As actuators, one of their most prolific uses has been found in the vibration control of flexible structures. In [4], piezoelectrics were used in a space truss experiment, CASTOR, tested on the MIR space station. The purpose of the actuators is to add damping to the flex-

ible structure at specific locations, reducing the overall flexibility of the structure. Piezoelectric actuators are also commonly used in the Stewart platform for vibration isolation of sensitive instruments [5–7]. In a slightly different configuration, they are also used in active struts to help mitigate the effect of launch vibrations transmitted from the launcher to the payload [8]. A current topic of considerable interest is their application to the problem of controlling the shape and vibration of inflatable structures [9].

Another application of piezoelectrics is for motors as they don't require electrical or mechanical commutation, have a high torque density at low speed, no backlash (as no gears are required), a fast response time, and a high holding torque [10]. For space applications, motors are required that can survive high temperature and radiation environments, and from vacuum to high pressure. Current commercial motor units typically have a maximum operation temperature of approximately 200°C, although some have been constructed for up to 500°C, but these have limited lifetimes and tend to be quite large. Development of piezoelectric-based motors for drive/steering motors, manipulator joint motors, lander petal motors, ultrasonic drills, corers, and rock abrasion tools are currently in development at NASA for a possible rover mission to Venus [10].

Among the most rapidly rising uses of piezoelectric actuators is in high-resolution positioning for a variety of devices. As they are monolithic in nature, in theory,

the positioning resolution of a piezoelectric actuator is limited only by its control electronics. For instance, stack actuators were used for the position control of a telescope mirror [8], and for the tip-tilt mechanism for PHARAO, an atomic clock operated onboard the ISS [11]. They are also used for scanning probe microscopy, 6 DOF positioning, and for spectrometry. The MIDAS experiment for the ROSETTA mission employed a three degree-of-freedom (xyz) piezoelectric actuator for the scanning motion of an atomic force microscope for analyzing the dust of comets [11].

An interesting new application for piezoelectric actuators is for proportional valves of spacecraft microthrusters [12]. They can be used naturally for nominally off valves, as the piezo need only be actuated to open the valve for a short thrust duration, but they can also be used for modulating the flow of gas for the thruster.

Another popular smart material is the shape memory alloy. This material can be deformed, and when an appropriate thermal procedure is applied to it, return to a predefined shape. For actuation, they possess the desired qualities of large force output, large displacement and simple supporting electronic instrumentation. As the material itself is an alloy, the Joule heating effect can be used to create the thermal load, or an external heater can be used to create this effect.

The most popular use of shape memory alloys in space has arguably been as low-shock release mechanisms to replace high-shock pyrotechnic release mechanisms. In

these applications, the SMA is in its detwinned form and then is slowly heated until it recovers its original shape, and release occurs. Examples of these include the range of Frangibolt and Pinpuller devices from TiNi Aerospace Inc., and miniaturized versions such as Qwknut [13] and Micro Sep-Nut [14] for micro-satellites. Frangibolt was flown on the 1994 Clementine mission to the moon and was used to deploy antenna, solar arrays, and the satellite from its launch vehicle [15].

A well known application of shape memory alloys was for the Mars Pathfinder mission. Here, an SMA was used in an experiment to quantify the effect of dust on the rovers solar cells. The SMA was used to rotate a dust cover off of a clean region of the panel to compare the power output with that of regions subject to dust accumulation [16].

SMAs can also be used for vibration isolation and damping [17]. The change in stiffness from the elastic region of the SMA response to the transformation region allows for isolation while the nonlinear pseudoelastic behaviour can be employed to dissipate the mechanical energy of vibrations [18].

Among the most intriguing possibilities of use for SMAs are in the areas of deployment, inflatable structures, and shape control. The lightweight flexible solar array (LFSA) experiment [19] used a SMA at the hinge location to open a folded solar array on the EO-1 spacecraft. Another experiment was the Shape Memory Alloy Thermal Tailoring Experiment (SMATTE) [16] which was flown on MightySat

II.1 where a thin SMA foil was integrated onto the surface of a bistable polymer matrix composite. Heating the SMA would force the panel to go from one shape to another, and relieve the thermal warping of the composite caused by the thermal stress [20]. The use of SMAs for shape control of spaceraft antenna has many intriguing future possibilities.

1.1 Piezoelectric Materials

In 1880, the Curie brothers first observed the piezoelectric effect during their experiments on quartz, tourmaline, and Rochelle salt where pressure on the crystals would create electrical charge, hence 'piezo', the Greek word for pressure. This is referred to as the direct piezoelectric effect, where mechanical energy is converted into electrical energy. In 1881, Lippman predicted the existence of the converse piezoelectric effect from the laws of thermodynamics, which the Curie brothers then verified through experiment [21]. Piezoelectrics were first used in ultrasonic transducers during World War I which led to a variety of uses after the war. Discovery of piezoceramics, specifically lead zirconate titanate (PZT) in the 1950's spurred many applications of piezoelectric materials as they possess very high dielectric and piezoelectric properties [22].

Piezoelectric ceramics are made up of perovskite crystals. Each crystal has a lattice structure with large divalent metal ions and oxygen on the outside with a

smaller tetravalent metal ion inside [21]. Piezoelectric ceramics are typically formed from powders pressed into the desired shape to create mechanically strong and dense ceramics. The ceramic is then machined and has electrodes attached, after which it must then be poled. Poling is done by exposing the material to a strong electric field, typically along a specific axis, at a temperature slightly lower than the Curie temperature. This causes the dipole moments of each of the subdomains of the ceramic to align. After the electric field is removed and the material is cooled, the subdomains of the crystal remain very closely aligned to the direction of the electric field applied for poling. The piezoelectric effect can only be exhibited by materials whose crystal structure has no center of symmetry, that is, they are anisotropic [23]. This is only the case for ceramics below the Curie temperature, where the crystal has a built-in electric dipole, although the net electric dipole on a macroscopic scale is zero. Pressure creates displacement of ionic charges within the crystal structure which causes the piezoelectric effect. Without any pressure, the charge distribution in the crystal structure is symmetric and no net electric dipole moment is created [22].

Piezoelectric materials can be used as a sensor when a force is applied to it. The compression or tension force exerted on the material changes the dipole moment which creates a difference in potential between the two surfaces of the material. More specifically compression in the poled direction generates a voltage of the

same polarity as the poling voltage, while compression perpendicular to that of the poled direction generates a voltage of opposite polarity to that of the poling voltage. Piezoelectrics can also act as actuators through the converse piezoelectric effect, where it will convert electrical energy into mechanical energy. If a voltage of the same polarity as the poling voltage is applied in the poled direction, this will cause the ceramic to lengthen and reduce its width. If a voltage with polarity opposite to that of the poling voltage is applied in the poled direction, this will cause the ceramic to shorten and widen.

The IEEE standard [24] for piezoelectric materials is a linear definition which is a valid assumption for small electric fields and mechanical stress levels [21]. The relation between the applied voltage and generated strain is linear to a point which depends on the material properties. However, it is important to note that for large electric fields or stress levels, the material may exhibit nonlinear behaviour. The constitutive equations for a piezoceramic can be formulated based on the assumption that the total strain in the material is the sum of the mechanical strain and the actuation strain caused by the applied voltage. The constitutive electromechanical equations can be written in tensor form as [25]

$$S_{ij} = s^{E}_{ijkl} T_{kl} + d_{kij} E_k \tag{1.1}$$

$$D_i = d_{ikl} T_{kl} + \epsilon^{T}_{ik} E_k \tag{1.2}$$

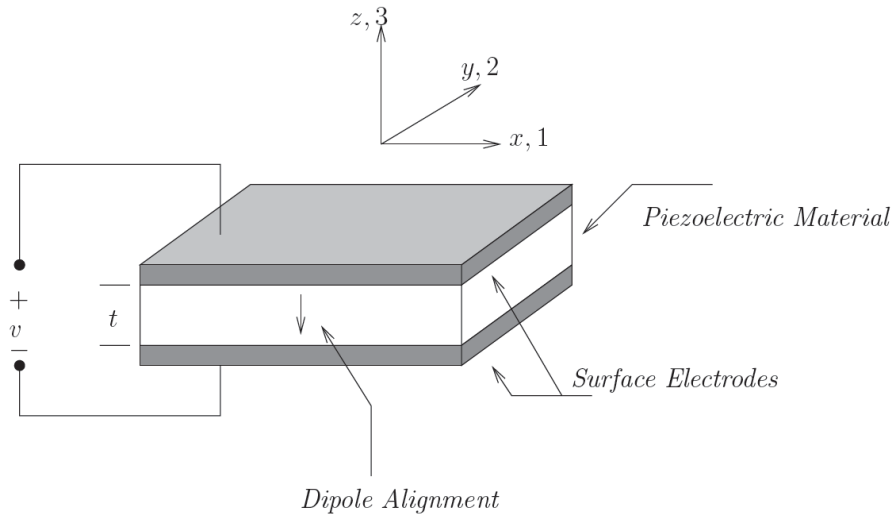

Fig. 1.1 Model of a piezoelectric material [21]

where S_{ij} is the strain tensor, s^E_{ijkl} is the compliance tensor, T_{kl} is the stress tensor, d_{kij} is the tensor of piezoelectric constants, E_k is the electric field, D_i is the electric displacement, and ϵ^T_{ik} is the dielectric constant. The convention is to take axis 3 (see Fig. 1.1) as the poling axis, as PZT is transversely isotropic in directions perpendicular to the poling direction. The constitutive equations can be rewritten in engineering notation as

$$\epsilon = S^E\sigma + dE \tag{1.3}$$

$$D = d^T\sigma + e^\sigma E \tag{1.4}$$

where ϵ is the strain vector, S is the matrix of compliance coefficients, σ is the stress vector in $\mathrm{N/m^2}$, d is the matrix of piezoelectric strain constants in m/V, E is the vector of the applied electric field in V/m, D is the vector of electric

displacements in C/m^2, e is the permittivity in F/m, and the superscripts E and σ denote measurements taken for a constant electric field and stress. Here, Eq. 1.3 represents the actuator equation and Eq. 1.4 represents the sensor equation. Since PZT is transversely isotropic, the only non-zero complicance coefficients are

$$\begin{gathered} S_{11} = S_{12} \\ S_{13} = S_{31} = S_{23} = S_{32} \\ S_{12} = S_{21} \\ S_{44} = S_{55} \\ S_{66} = 2(S_{11} - S_{12}) \end{gathered} \tag{1.5}$$

while the only non-zero dielectric coefficients are $e_{11}^{\sigma} = e_{22}^{\sigma}$ and e_{33}^{σ} and the only non-zero piezoelectric strain constants are $d_{31} = d_{32}$ and $d_{15} = d_{24}$ (this is true for PZT, not other piezoelectric materials such as PVDF). Hence, Eqs. 1.3–1.4 can be written in full as

$$\begin{bmatrix} \epsilon_1 \\ \epsilon_2 \\ \epsilon_3 \\ \epsilon_4 \\ \epsilon_5 \\ \epsilon_6 \end{bmatrix} = \begin{bmatrix} S_{11} & S_{12} & S_{13} & 0 & 0 & 0 \\ S_{12} & S_{11} & S_{13} & 0 & 0 & 0 \\ S_{13} & S_{13} & S_{33} & 0 & 0 & 0 \\ 0 & 0 & 0 & S_{44} & 0 & 0 \\ 0 & 0 & 0 & 0 & S_{44} & 0 \\ 0 & 0 & 0 & 0 & 0 & 2(S_{11} - S_{12}) \end{bmatrix} \begin{bmatrix} \sigma_1 \\ \sigma_2 \\ \sigma_3 \\ \sigma_4 \\ \sigma_5 \\ \sigma_6 \end{bmatrix} + \begin{bmatrix} 0 & 0 & d_{31} \\ 0 & 0 & d_{31} \\ 0 & 0 & d_{33} \\ 0 & d_{15} & 0 \\ d_{15} & 0 & 0 \\ 0 & 0 & 0 \end{bmatrix} \begin{bmatrix} E_1 \\ E_2 \\ E_3 \end{bmatrix} \tag{1.6}$$

$$\begin{bmatrix} D_1 \\ D_2 \\ D_3 \end{bmatrix} = \begin{bmatrix} 0 & 0 & 0 & 0 & d_{15} & 0 \\ 0 & 0 & 0 & d_{15} & 0 & 0 \\ d_{31} & d_{31} & d_{33} & 0 & 0 & 0 \end{bmatrix} \begin{bmatrix} \sigma_1 \\ \sigma_2 \\ \sigma_3 \\ \sigma_4 \\ \sigma_5 \\ \sigma_6 \end{bmatrix} + \begin{bmatrix} e_{11}^{\sigma} & 0 & 0 \\ 0 & e_{22}^{\sigma} & 0 \\ 0 & 0 & e_{33}^{\sigma} \end{bmatrix} \begin{bmatrix} E_1 \\ E_2 \\ E_3 \end{bmatrix} \tag{1.7}$$

where the piezoelectric coefficient d_{ij} is the ratio of free strain in axis j to the electric field that is applied along axis i with all external stresses constant. When a

voltage is applied in the poled direction (which is axis 3 by convention), the electric field created is

$$E_3 = \frac{V}{t} \tag{1.8}$$

hence, the strain induced in axis 1 is then

$$\epsilon_1 = \frac{d_{31}V}{t} = \frac{\Delta l}{l} \tag{1.9}$$

The elastic compliance coefficient S_{ij} is the ratio of the strain in i to the stress in j while there is no change of stress in the other directions. For subscripts higher than 3, the elastic compliance coefficient refers to the ratio of shear strain in axis i to the shear stress in axis j (also defined as $\epsilon_4 = \gamma_{23}$ and $\sigma_4 = \tau_{23}$). The dielectric coefficient e_{ij} is the charge per unit area in i due to the electric field applied in j [21]. In some applications, the relative dielectric coefficient may be used as

$$K_{ij} = \frac{e_{ij}}{\epsilon_0} \tag{1.10}$$

where in this application only, ϵ_0 refers to the permittivity of free space. While it has not been used in this discussion, the coupling coefficient k_{ij} is often used to characterize piezoelectric materials. The coupling coefficient refers to the efficiency with which the ceramic can convert mechanical energy into electrical energy and back. The coupling coefficient can be expressed in terms of other piezoelectric constants as

$$k_{ij}^2 = \frac{d_{ij}^2}{S_{ij}^E e_{ij}^\sigma} \tag{1.11}$$

1.2 Shape Memory Alloys

Shape memory alloys are metallic materials that have the ability to return to a predetermined shape when subjected to an increase in temperature past a certain threshold. While many alloys exhibit this effect to some degree [26], the term shape memory alloy is typically only applied to those alloys that can generate a significant amount of force, or recover a significant amount of strain. This effect was first seen in 1932 in a gold-cadmium alloy, but it wasn't until 1962 that the shape memory effect was observed in a nickel-titanium (NiTi) alloy that research into its effect and applications took off. NiTi (also referred to as nitinol) is the most common shape memory alloy, although copper-based alloys such as Cu-Zn-Al and Cu-Al-Ni have also been used, albeit to a much lesser extent. NiTi alloys offer the advantage over copper-based alloys in that they are much more thermally stable, exhibit a greater shape memory strain, higher ductility, and excellent corrosion resistance [26]. The desired 'memory shape' is typically created by heat treating the alloy between 500 and 800°C for a few minutes.

Shape memory alloys are a class of metallic alloys that exhibit phase transformations within their solid state. These phase transformations are created by temperature and/or stress changes and allow the material to recover what appear to be permanent strains [27]. SMAs provide large actuation forces and displacements,

however over only a low frequency bandwidth. The SMA's behaviour is due to the martensitic transformation between its martensite and austenite phases. Austenite exhibits a cubic structure and is the high temperature phase, while martensite is the low temperature phase where the material exhibits a tetragonal or monoclinic structure.

In the absence of applied stress, the SMA will change from its martensitic phase to its austenitic phase due to the application of a thermal load. This transformation will begin at the austenitic start temperature (A_s) and finish at the austenitic finish temperature (A_f). If the thermal load is then removed, as the material cools, it will begin its solid phase change at the martensitic start temperature (M_s) and become fully martensitic at its martensitic finish temperature (M_f). As can be seen in Fig. 1.2, there is hysteresis associated with the phase change as the martensitic start temperature is lower than the austenitic start temperature.

So far it has been assumed that there is no applied stress to the shape memory alloy, and in this absence there will be no macroscopic shape change of the material as it transitions from the austenite to martensite phase, as the SMA will exhibit a twinned structure. However, once a stess is applied above a certain level to the alloy in its martensitic phase, the SMA will deform in shear from twinned martensite to detwinned martensite (see Fig. 1.3). When the stress is removed, the SMA will remain in its detwinned martensite form (and hence in its changed

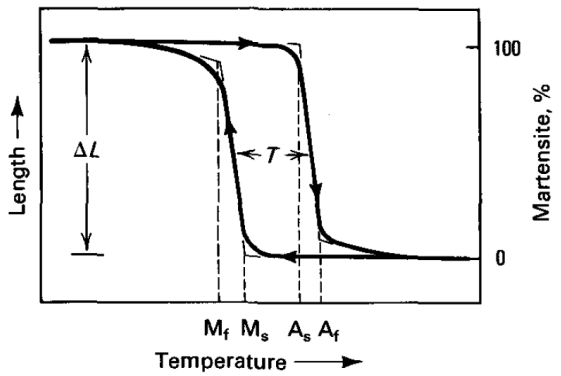

Fig. 1.2 Transformation vs. temperatue curve for SMA under constant load [26]

shape) as the crystallographic stucture of the SMA is stable in its detwinned phase. It will remain detwinned until a thermal load is applied to revert the SMA to its austenite phase, and its 'remembered' shape. If the return to the SMA's austenite phase is resisted, the SMA can generate very large forces. When the temperature is reduced, the SMA will return to its twinned martensite form. While there is a transmission path from twinned to detwinned martensite, no direct return path exists. This can be seen graphically in Fig. 1.4. This is termed the stress-free shape memory effect, where the phase change to austenite results in the recovery of what apperars to be a permanent deformation that occurs during detwinning (see Fig. 1.4). When the load is removed, the elastic portion of the total strain is recovered. The inelastic portion associated with the detwinning process remains (as the detwinned martensite structure is stable). The inelastic strain is only recovered once the SMA is reheated and returned to its austenite phase. If any plastic strain

occurs it will not be recovered.

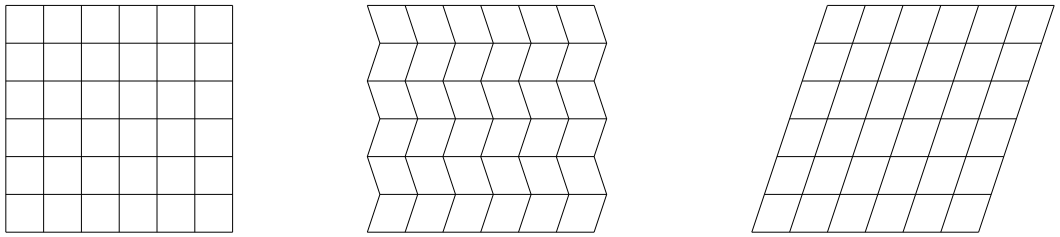

(a) (b) (c)

Fig. 1.3 Crystal phases of shape memory alloy: (a) Austenite (b) Martensite (twinned) (c) Martensite (detwinned)

Another property of the SMA is that they exhibit pseudoelastic behaviour. This is caused by a stress-induced phase transformation from austenite to detwinned martensite when the material is slightly above its transformation temperature which results in increasing strain at constant stress. When unloaded it returns to its austenite phase, but not through a temperature change, but through the reduction of stress. The Clausius-Clapeyron equation gives the critical stress for the martensitic phase change at a given temperature as [28]

$$\frac{d\sigma_c}{dT} = \frac{\Delta H}{V T_0 \Delta \epsilon} \tag{1.12}$$

where σ_c is the critical stress, T is the given temperature, T_0 is the temperature at which the phases are in equilibrium at $\sigma = 0$, V is the molar volume, $\Delta\epsilon$ is the transformation strain, and ΔH is the transformation enthalpy. In more detail, this

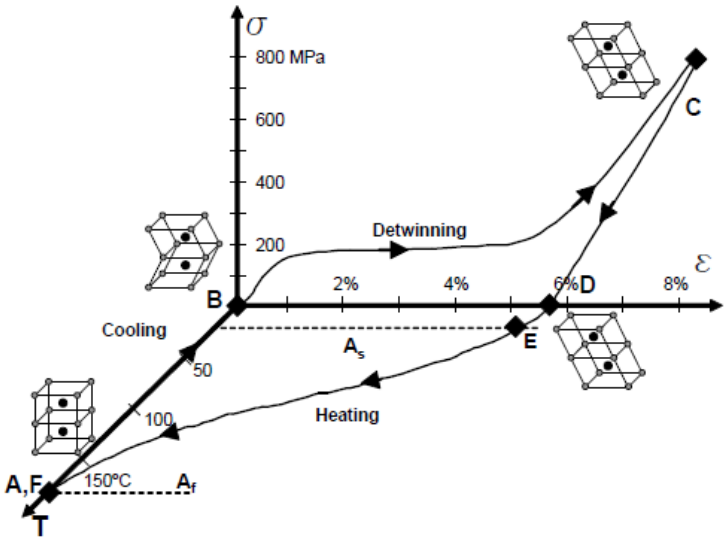

Fig. 1.4 Stress vs. strain vs. temperature curve of SMA [27]

effect can be seen in Fig. 1.5(c). Before Point A it is in its austenite phase and the SMA responds elastically. After this point, stress-induced detwinned martensite begins to form and large inelastic strains are generated through to Point B, where the material is in a detwinned martensitic phase. When loaded above this level, the SMA once again responds elastically. When the stress is lowered to Point C, the reversion to the austenitic phase starts and the inelastic strain is recovered between Point C and D, where at D, the material is in its austenitic phase once again. The constitutive relations of the SMA rely on the stress-strain-temperature space [29–32] and are given by

$$\sigma - \sigma_0 = D(\epsilon - \epsilon_0) + \Theta(T - T_0) + \Omega(\xi - \xi_0) \tag{1.13}$$

where D is the modulus of elasticity, Θ is the thermoelastic tensor, Ω is the transformation tensor, and $\xi(\sigma, T)$ is the martensitic fraction [28]. It should be noted however, that there are still many limitations in the general applicability of the consitutive equations for modeling, including the commercial finite element codes that include analysis packages for SMAs. In fact, for most space applications, little to no modeling was performed of the SMA through its constitutive equations, and the systems were designed predominantly through careful experimentation [27].

Shape memory alloys can be used as force/displacement actuators as they can exert force over a large range of motion, often for a large number of cycles. It is possible to use a shape memory alloy as a force/positioning mechanism by using only a portion of the shape recovery as the phase transformation occurs over a range of temperatures, that also depend on the stress level. For this, a bias mechanism or load force must be used to return the actuator to its detwinned martensite phase, or no macroscopic change will occur. Due to the resistance of nitinol, it can be actuated electrically by Joule heating. This occurs when an electric current is passed through the SMA and heats it enough to cause the phase transformation from martensite to austenite. This gives good control over the temperature of the SMA (and hence force or displacement), however, large currents are typically required as the resistance of NiTi is small, as it is a metal alloy. Also, as the current must flow directly through the SMA, it must be electrically isolated. A

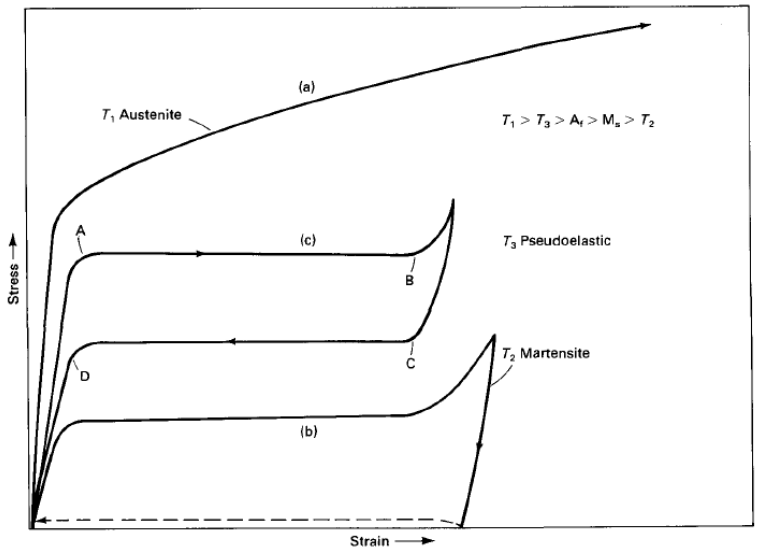

Fig. 1.5 Stress-strain curve for SMA at different temperatures [26]

heater could also be used for actuation of the SMA, however, this is both bulky and deteriorates the cooling cycle time as the surrounding heating elements must also cool sufficiently for the martensitic phase change to take place.

1.3 Research Objectives and Organization

This thesis is concerned with the application of smart materials to three specific space engineering applications: shape memory alloys for flatness control of a membrane structure, piezoelectrics for vibration control of a single-link flexible manipulator, and piezoelectric stack actuators for nanopositioning of space instrumentation.

Chapter 2 presents experimental studies on the active flatness control of a rectangular membrane structure with elliptical boundary cuts. The control is achieved by using twenty shape memory alloys as actuators, each with their own proportional control loop. In Section 2.2 a genetic algorithm (GA) is implemented to minimize the surface flatness of the membrane. A conventional GA with a single objective function is used as well as a genetic algorithm with online objective reweighting capability that is proposed here. This genetic algorithm implements an objective function that re-weights its objective online to consider both the flatness of the membrane and tension required by the actuators to achieve it. Experiments are conducted on a membrane test facility with two implementations: a static mutation rate, and an adaptive mutation rate. Finally, in Section 2.3 the control architecture for the twenty shape memory alloy actuators used in control of the membrane structure is revised. The control is based on proportional-integral control with three different types of pulse width modulation used at the output to more effectively use the available current. A duty cycle is then implemented for each of the three PWM types such that a maximum on-time for the shape memory alloys can be enforced to allow larger currents to be used without damaging the actuators. Experimental verification of the controllers is conducted, and then their use for shape control of a membrane under a time-varying thermal load is shown.

Next, Chapter 3 concerns the development of vibration control strategies for

a flexible manipulator with a collocated piezoelectric sensor/actuator pair. The experimental system is outlined and then dynamic modeling of the flexible manipulator is conducted through the finite element method. In Section 3.3 a vibration controller combining the input shaping technique with multi-mode adaptive positive position feedback is developed to suppress vibration of the flexible manipulator induced by a slew maneuver. Next, in Section 3.4 an iteratively implemented genetic algorithm is applied to the system identification problem of the flexbile manipulator. A control law based upon positive position feedback is then developed for vibration suppression. A minimization criteria based on the H_∞-norm of the closed loop system is solved by a genetic algorithm to derive optimal controller parameters. Numerical simulations and experiments are performed to verify the effectiveness of both methods.

Then, in Chapter 4, the use of piezoelectric stack actuators for nanopositioning of space instruments is presented. A linear model of the piezoelectric is first developed and then a nonlinear phenomenological model is identified from experimental data based upon the modified Prandtl-Ishlinskii model. Then, in Section 4.3 a state feedback integral plus double integral synchronization control method is developed for a parallel three-axis positioning mechanism based on piezoelectric actuators. Next, in Section 4.4 an output feedback integral control law is examined for the piezoelectric actuator considering its nonlinear behaviour as an input nonlinearity

to the state space model of the system. Conditions on the maximum integral gain are derived such that the system is asymptotically stable. Then, in Section 4.5 this method is extended to derive an output feedback integral synchronization control law for the piezoelectric actuators considering their input nonlinearities. Global asymptotic stability of the system is ensured through a Lyapunov stability analysis. Experiments and hardware in the loop (HITL) simulations are conducted for each of the above controllers.

Finally, Chapter 5 concludes this work. The results of this work are summarized, and possible future research directions are discussed.

1.4 Major Contributions

The major contributions of this dissertation are:

1. Development of active flatness controllers for membrane structures based on different methodologies, including a fast, simple control structure for many shape memory alloy actuators

2. Design of an adaptive positive position feedback controller and its combination with input shaping for vibration control of a structure with uncertain natural frequencies

3. A system identification and controller optimization technique for resonant

structures based on an iterative genetic algorithm

4. Design of an integral plus double integral synchronization controller for synchronized movement of multiple piezoelectric actuators

5. Considering the piezoelectric actuator, with its inherent hysteresis, in the context of absolute stability theory and deriving maximal integral gains for stability

6. Extending this work to the derivation of an integral synchronization controller for multiple piezoelectric actuators with consideration for the hysteresis' effect on stability

2 Active Shape Control of a Membrane Structure using Shape Memory Alloys

Membrane structures are finding applications in future space missions including synthetic aperture radar (SAR) antennae [33], solar sails [34–36], membrane mirrors [37–39], and spacecraft sunshields [40,41] among others [42]. The elements common to all gossamer spacecraft are thin-film membrane structures [43, 44] which are ultra-lightweight structures, that can be folded and deployed in-situ, and provide larger surface area to weight ratios than their rigid counterparts. A comprehensive literature review of the design, analysis, experimentation, and control of gossamer spacecraft can be found in [45].

A membrane structure has effectively no resistance to compressive stress, hence any compression in the membrane is relieved through wrinkling. Wrinkling can occur in a membrane by a number of methods, including through applied boundary tensions or a concentrated thermal load. For example, a thermal load will cause expansion, and since there is no resistance to compressive stress, wrinkles will be

induced. Such wrinkles could cause significant deterioration in the performance of membrane structures. For example, the occurrence of wrinkles could reduce surface accuracy in membrane reflectors or cause nonuniform surface heating in solar sails. Of particular interest to this study is the use of a membrane structure for a C-band synthetic aperture radar antenna. A membrane structure used for a SAR antenna has the possibility of being $\frac{1}{10}$ the cost, $\frac{1}{100}$ the launch volume, and $\frac{1}{2}$ the mass of conventional SAR systems [46]. However, the surface accuracy of the antenna becomes a critical requirement as any wrinkles in the membrane will cause degradation in the system performance due to phase shifts in the signals. A general guideline is that the surface accuracy must be maintained within $\frac{1}{10}$ to $\frac{1}{20}$ of the operation wavelength [46]. Therefore, the design of efficient membrane structures that would minimize wrinkle occurrence is of tremendous importance. Moreover, effective wrinkle control strategies are required in order to eliminate wrinkles once they occur.

Square membranes are an excellent starting point for experimental verification of numerical methods, because they admit to well-known wrinkling patterns [47]. In previous work, a considerable amount of effort has been expended to predict wrinkles under various conditions. Some attempts at analytical approximations have been made [35, 48], but in general, a full nonlinear finite element analysis must be undertaken due to the geometrically nonlinear behaviour of the membrane

[49–51]. From analysis of a rectangular membrane, it was discovered that elliptical boundary cuts reduce the stress concentrations at the corners of the membrane, so wrinkling is reduced compared to a rectangular membrane of the same size [52]. Further, adding the boundary cuts allows for tensions to be applied not only to the corners, but also at the areas between cuts. Thus, more complex tension combinations can be applied and wrinkling can be reduced with less control effort. Since we are dealing with a space application, less control effort translates directly into lower power required for wrinkle reduction, and so is a central step in proving the feasibility of membrane structures in space.

Due to the complex nature of the analysis, the computational time to solve even simple static problems can become immense, making it currently unsuitable for the testing of active flatness controllers. There have been a variety of methods proposed for shape or flatness control of membrane structures. In general, there are two major divisions, those with the control elements embedded into the membrane structure, and those with control elements along the boundaries of the membrane. The first main approach for active flatness control is that of patching/embedding smart materials into the membrane for control of surface profiles, which typically depend on piezoelectric films [53–55] to ensure the required surface accuracy. Provided a sufficient number of these elements are patched onto the surface, a large control authority can be exerted on the host structure [52]. This approach has

the drawback that the embedded sensors and actuators may interfere with the microwave components that need to be patched onto the membrane structure, and that the behaviour of the structure can become much more difficult to predict. The second main approach for active flatness control is that of manipulating the boundaries by actuators connected to the edges of the membrane, which will be used in this study.

Shape memory alloys are materials that contract when an electrical current is applied to them due to the Joule heating effect. SMAs offer suitable actuation forces and adequate response times, unfortunately, SMA's themselves suffer from nonlinear effects in the form of hysteresis. Thus, the SMA's require their own controller if they are to be used for shape control of the membrane structure. A variety of methods have been employed to control SMAs including adaptive control [56], self-tuning fuzzy PID [57], and neural networks [58] among many others. However, since twenty SMAs must be controlled in real-time, it is desirable to have a simpler and faster control architecture. Once the SMAs are properly controlled, the membrane surface flatness can be manipulated by these actuators mounted along the boundary of the membrane.

Of particular interest to this study, in [59–61] a GA-based controller was applied to a 200 mm by 300 mm rectangular membrane structure through the use of 12 SMAs and shown to produce good flatness values. This work was built upon

in [62] for a 200 mm by 300mm rectangular structure with 8 SMAs where the GA-based controller was combined with a neural network for control. Finally, in [52] an adaptive GA was applied to the same membrane structure that will be used in this paper. In Section 2.2, an active flatness control strategy using a genetic algorithm with online objective reweighting is proposed and tested on an experimental membrane facility. The standard GA objective functions are reformulated with online objective function reweighting in an attempt to reduce the total tension required by the control while keeping the original objective of maximum surface flatness satisfied. In the previous GA-based controllers, the objective function was solely the flatness value of the membrane.

However, there are a few drawbacks to the GA-based control schemes. The first is that it computes optimal tension combinations for twenty attachment points, thus the search space is considerably large and the time required and computational effort is considerable. Finally, the main drawback of the GA-based controllers is that the possible combinations must be physically tried on the membrane. A faster and simpler control scheme is desired, especially considering membrane technology is going to be applied in space, where computational resources tend to be limited. For this, a proportional-integral controller is designed in Section 2.3.2 to track a desired flatness level under changing thermal conditions. This is highly desirable due to the fact that power usage of the control system can be minimized as the

actuators will be tightened or loosened based on the current wrinkled state of the membrane.

In this chapter, the membrane structure and details of the experimental system and setup is outlined in Section 2.1. Then, in Section 2.2 the design of the GA controllers for flatness minimization is presented. Next, in Section 2.3, the design of proportional-integral (PI) controllers combined with three different types of pulse width modulation (PWM) with duty cycling is shown. In Section 2.3.2, results are presented for the shape control of the membrane structure under varying thermal loading conditions with the new SMA controllers. With the SMAs supplying the desired boundary tensions, membrane flatness can be maintained effectively through a simple PI master control loop.

2.1 Membrane Structure and Experimental Setup

Fig. 2.1 shows the membrane structure used in this study. The original rectangular membrane size is 800 mm by 550 mm. In order to reduce wrinkling, elliptical boundary cuts along membrane's edges are made, as shown in Fig. 2.1. This will reduce stress concentrations at the corners, and thus wrinkle amplitudes. Table 2.1 gives the properties of the membrane structure used in this study. For active flatness control, twenty shape memory alloy (SMA) actuators are connected to each of the twenty attachment points, along with strain gauge sensors to determine the

tension applied at the attachment points.

Table 2.1 Properties of membrane structure

Property	Value
Material	Kapton Type 100 HN film
Boundary cut shape	Elliptical
Number of cuts	20
Attachment elements	20
Actuators	Shape memory alloy
Number of actuators	20
Outside size	800 mm $\times$ 550 mm
Inside size	640 mm $\times$ 440 mm
Thickness, h	25.4 μm
Density, ρ	1420 kg/m^3
Young's modulus, E	2.5 GPa
Poisson's ratio, μ	0.34
Linear coefficient of thermal expansion	20 ppm/°C

Due to the fact that the membrane can only carry very small compressive stresses, it is expected that a concentrated heat load will cause significant wrinkling of the membrane. This is a problem due to the membrane being essentially unable to carry compressive stresses, which create localized wrinkling in the membrane as a relief mechanism. This effect is created by the thermal load causing local expansion of the membrane where it is applied, while areas further away from the heat load will not be affected. When a locally expanding area meets one that is not, compressive stresses form and the membrane will experience wrinkling. Nonlinear finite element simulations have been run previously, and the expected wrinkling of

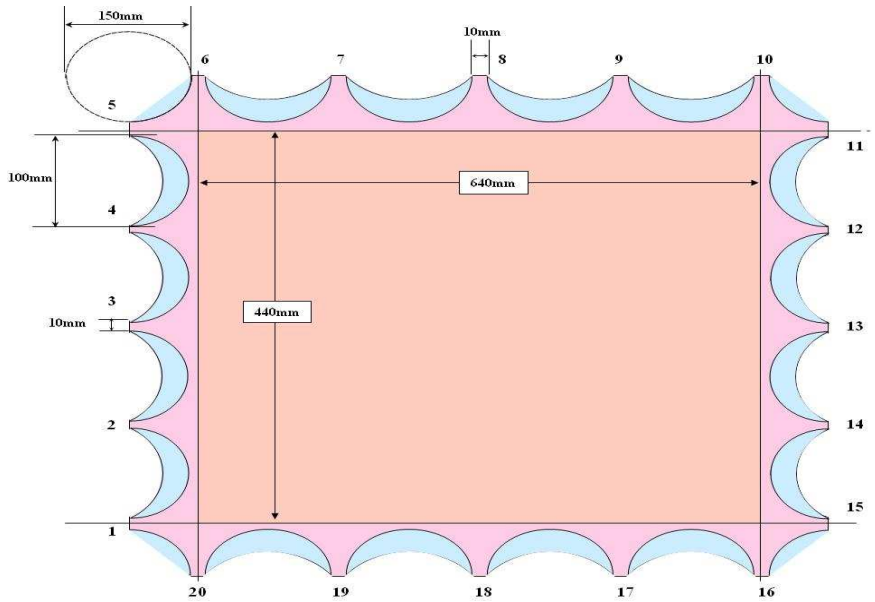

Fig. 2.1 Membrane with boundary cuts

the membrane structure can be seen in Fig. 2.2. Clearly, the surface of the membrane is distorted and its ability to operate, specifically as a SAR antenna, would be compromised. To keep the surface of the membrane maximally flat, the root mean square deviations of the membrane surface from its in-plane nature should be kept to a minimum. Fig. 2.3 shows the membrane structure active flatness control test facility. The facility consists of two main components: (a) vision system to measure the membrane flatness; (b) membrane with control electronics.

The vision system includes a 1300×1000 pixel CMOS digital camera and a light projector. The camera is calibrated in 3D world space, which allows a pixel in the camera plane to be mapped to a line (cone) radiating from the focal point in the

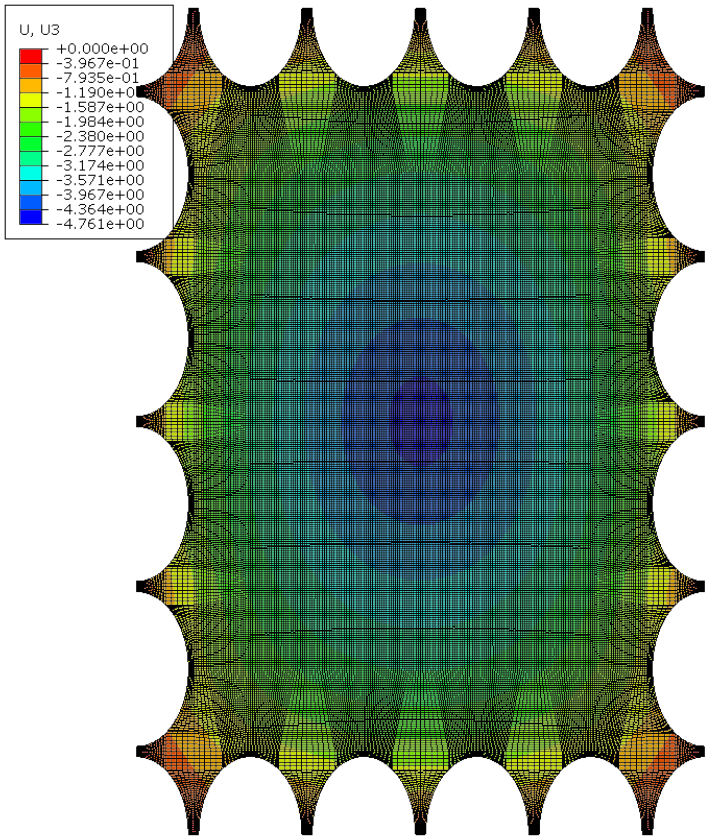

Fig. 2.2 Finite element analysis of membrane under central heat load

world coordinate system [62]. The flatness of the membrane is determined using a photogrammetry technique. The light projector projects multiple light planes onto the membrane surface, which produce lines on the membrane. These planes are calibrated in the world coordinate space. The camera observes the points on the curves projected by the projector. In order for the vision system camera to see the curves clearly, a very thin coating is put on one side of the membrane. Locations of these points and their 3-D coordinates are thus determined by the light plane and

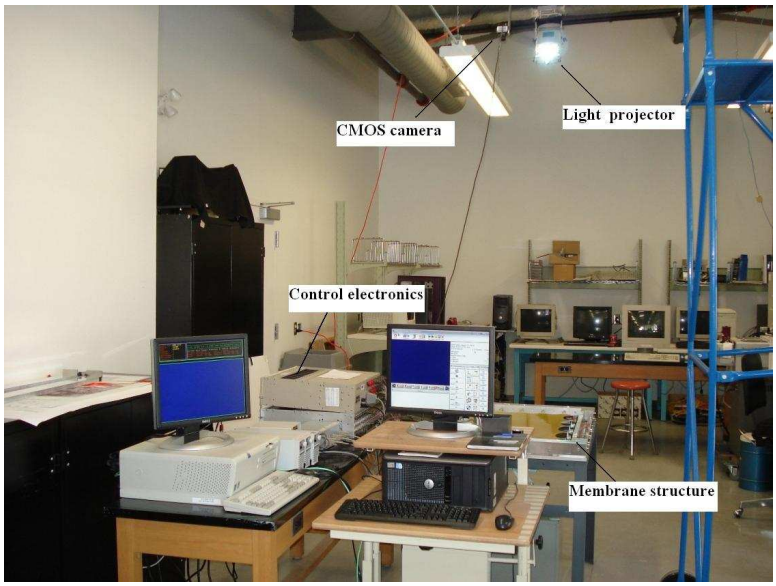

(a) Overall system

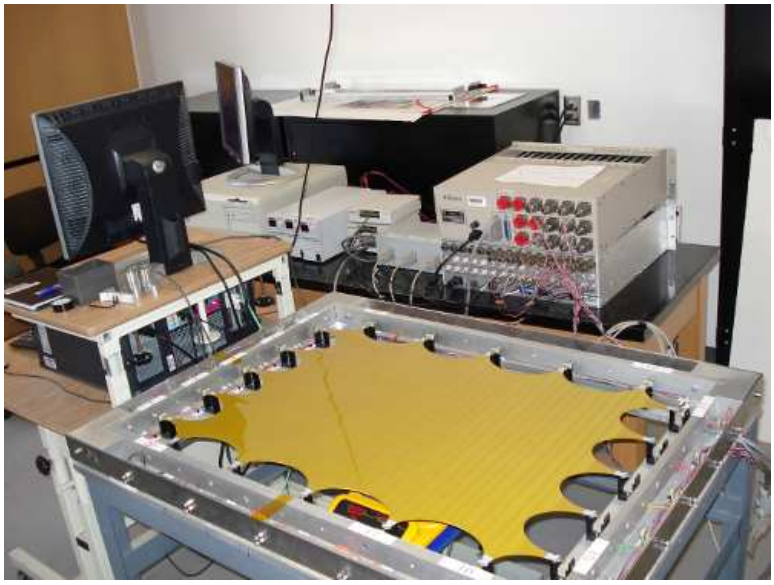

(b) Membrane structure

Fig. 2.3 Membrane structure test facility

the associated radiating line from the camera focal point. The membrane flatness is defined as the root mean square (RMS) deviation of the membrane surface from a plane of best fit which can be defined as

$$d_{rms} = \sqrt{\frac{\sum_{i=1}^{n} d_i^2}{n}} \tag{2.1}$$

where d_i is the distance of the i^{th} point on the membrane surface from the fitted plane, and n is the number of measurement points. The RMS value of the membrane surface above a plane of best fit can be determined by the vision system with sub-millimeter accuracy. Test results have shown that the vision system works very well, and further details of this method can be found in [59]. The membrane flatness data obtained from the vision system is used in the objective functions for each of the individuals in the current population of the genetic algorithm to evaluate their fitness, or as the feedback variable.

The membrane is attached to a frame through twenty attachment points by SMA actuators for use in tension control. The actuators are connected to an attachment with adjustable screws such that a small pre-tension force is applied (see Fig. 2.4). The SMAs are Nitinol type and their properties can be found in Table 2.2. The SMAs are powered with three Lambda ZUP20-10 DC power supplies with 20 V and 10 A maximums. The data is transferred through three National Instruments SCB-68 DAQ boxes. Ectron Corporation 563H boards are used to measure the actual tensions applied by the SMAs through the use of strain gauges as sensors. Real-

time control is implemented in MATLAB Real-Time Workshop and xPC Target. A master computer is used to run the vision system and control and then supply required tensions to a real-time slave computer. The real-time computer takes the tensions and runs a simple on-off proportional controller to monitor the strain gauges and supply more current to the actuator's if necessary [61].

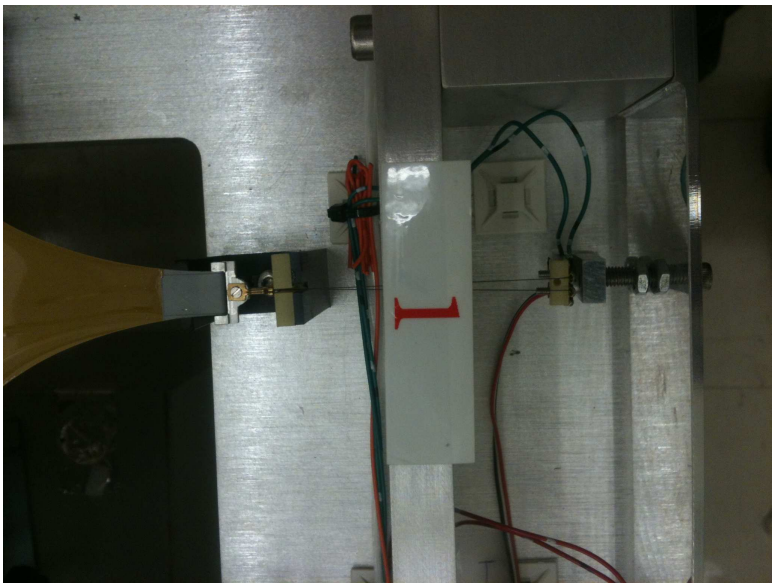

Fig. 2.4 One shape memory alloy and its attachment to the membrane and frame

In order to simulate thermal disturbance on the membrane, a ceramic heater is placed 0.1 m below the membrane surface. The heat load can be adjusted between 5°C and 540°C at a temperature interval of 5°C. In this study, two temperatures, 145°C and 205°C have been used. The first choice of temperature for this study was made in order to qualitatively compare with previous results in [52] that were

Table 2.2 Properties of the shape memory alloys

Property	Value
Material	Nitinol (NiTi)
Diameter	0.2 mm
Length	66 mm
Resistance	29 Ω/m
Maximum pull force	0.570 kg
Input Current	660 mA
Austenite finishing temperature	90°C

produced at this temperature. The second temperature choice (205°C) was made simply to run the tests at a higher temperature, while ensuring that the membrane will not be damaged. Since the heat load is not in direct contact with the membrane, this corresponds to maximum membrane temperatures of approximately 56°C and 71°C, respectively. Fig. 2.5 shows thermal distribution photos of our membrane facility taken by an infrared camera. A contour plot of the wrinkle pattern recorded by the measurement system can be seen in Fig. 2.6, with a rather large central distortion. The controllers are tested against the wrinkling caused by the two heat loads. An obvious expectation is that the larger heat load will cause more wrinkling.

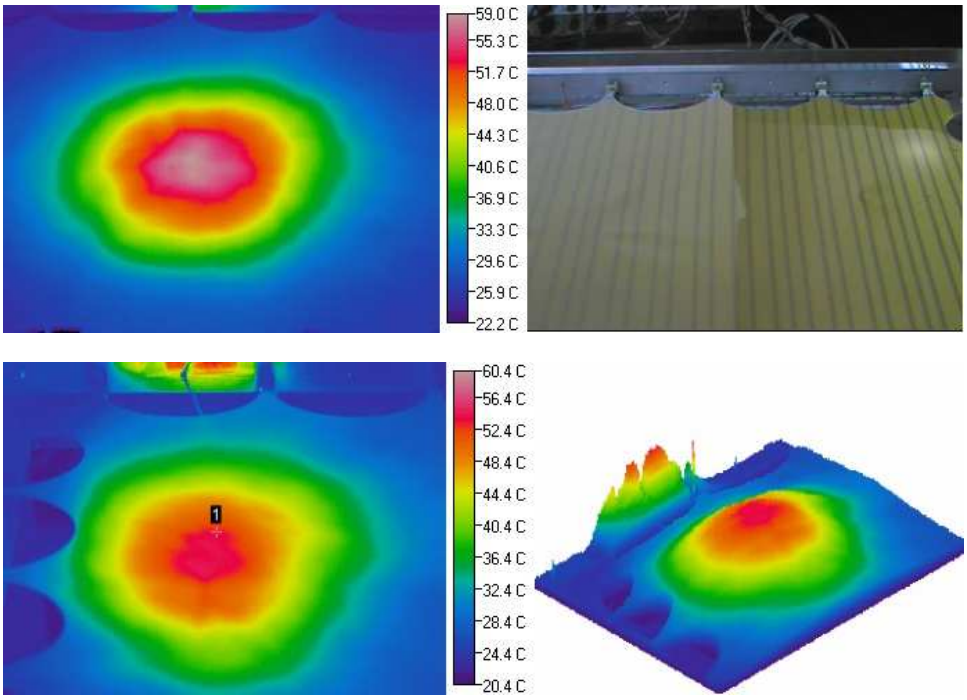

Fig. 2.5 Thermal distribution of membrane structure

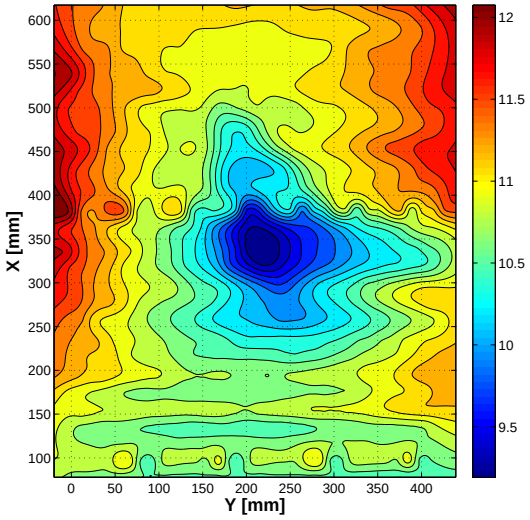

Fig. 2.6 Contour plot of central membrane area under 205°C heat load

2.2 Genetic Algorithm for Control of a Membrane Structure

The nonlinear behaviour of the membrane antenna with twenty shape memory alloy actuators is very difficult to characterize, and finding the tension combination that yields a maximally flat membrane surface can be formulated as an optimization problem. However, traditional analytical optimization techniques face significant drawbacks due to the knowledge that must be possessed of the system beforehand. Genetic algorithms on the other hand are stochastic algorithms capable of searching the entire solution space with more likelihood of finding the global optimum when the system is either hard to characterize, or little is known about it ahead of time. Here, different implementations of a GA will be used to search the 20-D parameter space for the tension combinations that lead to a minimum surface deviation of the membrane.

In [52] a genetic algorithm is developed and applied to active flatness control of membrane structure and works as follows: each member c_i of the population of individuals represents a solution to the optimization problem of flatness minimization. Each member c_i is given by twenty tensions as

$$c_i = \{T_1, \dots, T_{20}\} \tag{2.2}$$

Each candidate function is coded as a chromosome, and the population is ini-

tialized randomly. The fitness (or objective) function that is evaluated is

$$F(c_i) = d_{rms} \tag{2.3}$$

where d_{rms} is the root-mean-square deviation of the membrane surface above a plane of best fit as measured by the photogrammetry system. After each generation, the relative fitness of each individual is evaluated. If the population size is μ and the frequency of crossover is given by p_c, then the number of individuals, n_c, selected for crossover is

$$n_c = \frac{\mu p_c}{2} \tag{2.4}$$

The offspring can replace their parents in subsequent generations provided that their fitness values are superior. To avoid the possibility of zero-probability for a given solution to propagate, we allow for mutation at a rate given by p_m. Finally, the maximum number of generations, G_{max}, limits the number of times that crossover and mutation can occur while searching for optimal solutions. Once the maximum number of generations is reached, the process ends.

2.2.1 Adaptive Genetic Algorithm (AGA)

In the standard genetic algorithm, the mutation rate is static and chosen by the designer. However, the choice of parameters p_c and p_m, can drastically affect the solution. If the mutation rate is too high, then the offspring will not resemble their

parents, and the solution may oscillate [52], while if the crossover rate is too low, the search may not be able to find an improved solution, as too many individuals from a sub-optimal generation may make it through to subsequent generations.

To avoid this issue, an adaption mechanism was proposed in [52] in order to adapt the mutation rate based on the convergence of the solution. At the beginning of an experiment, the mutation rate should be high. The theory behind genetic algorithms indicates that, as time goes on, convergence tends to happen. Thus the mutation rate should be gradually decreasing. However, if a local minimum is found that is not optimal, the mutation rate is increased to avoid a "stalemate" situation. Finally, if the flatness value dramatically improves from one generation to the next, the mutation rate is decreased to preserve what is assumed to be a good set of chromosomes in the population.

The crossover rate is also changed, but less drastically. The average performance of the population is evaluated as [52]

$$\bar{F}_g = \sum_i \frac{F(c_i)}{\mu} \tag{2.5}$$

Since the crossover rate is the probability of individuals from a given population being allowed to go forward into a subsequent generation. For a high average performance value (5% in [52]), the crossover rate is set to 0.8. If the average performance is near zero, the crossover rate is set to 0.7, and if the average performance is poor (the population is becoming less fit), the crossover rate is set to 0.6

to attempt to drive the solution away from the problem.

2.2.2 Genetic Algorithm with Online Objective Reweighting

As mentioned above, a genetic algorithm has been proposed to achieve a low level of wrinkling by finding the tension combination that optimizes the objective function (minimizes d_{rms}). The genetic algorithm was also augmented to include adaptive behaviour in the mutation rate, such that premature convergence should not occur. Again with the adaptive GA, the objective function was the same.

Since the membrane structure and its active flatness control system will be applied on a spacecraft, power and computational resources are of particular concern. Ultimately, any resource that goes into flatness control cannot be used for the mission objectives. However, wrinkle control with twenty attachment points provides a twenty-dimensional search space. If we attempt to minimize both wrinkling and power consumption at the same time, the search space would increase in size, further using computational resources. The fact remains, however, that a solution from the previous GA's that minimizes wrinkling will not minimize the power required to reach that flatness level. To contend with this, an online-reweighting genetic algorithm is developed in which minimizing surface deviation takes precedence until a convergence threshold is reached. When convergence is occurring in successive generations, the difference in the flatness values (which are also the ob-

jective functions) should become small. At this point, the online reweighting GA will begin to modify its objective function to include a preferential weighting for small tension combinations that yield very similar flatness values. For example, if the membrane is wrinkled and 3 N applied to all of the actuators yields a flatness that is only 0.01 mm higher than that of 6 N on all of the actuators, clearly the first case would be preferred. Thus, the objective is reweighted based on how close the algorithm is converging, and the newly preferred combination will be kept into successive generations and used for crossover and mutation.

Since the tensions are proportionally related to the electrical current requirement, and the power requirement depends on the square of the current requirement, in an effort to minimize the amount of power used it would make sense to minimize the amount of force applied by each actuator. This leads to another problem in that having a minimum flatness and tension requirement right from the beginning may not lead to the best performance of the control algorithm. This can possibly drive the solution away from its minimum flatness value if the minimum tension constraint takes precedence. To compensate, the proposed controller minimizes first the flatness, then once it has begun to converge, the tensions are minimized. This is particularly applicable when the optimal solution exists on a large plateau in the solution space. Thus, as the primary objective function converges, the algorithm becomes more concerned with minimizing the secondary objective without

knocking the primary objective off of its plateau in the solution space.

The new objective function is then defined as

$$F(c_i) = \begin{cases} d_{rms} - \dfrac{1}{k\left[\max(d_{rms}) - \min(d_{rms})\right]\sum_{i=1}^{N} T_i}, & \text{for } \max(d_{rms}) - \min(d_{rms}) > M \\ d_{rms} - \dfrac{1}{kW}, & \text{for } \max(d_{rms}) - \min(d_{rms}) \leq M \end{cases} \tag{2.6}$$

where d_{rms} is the flatness of the membrane (and also the previous objective function defined in Eq. (2.3)), N is the number of actuators, T_i is the tension applied by the i-th actuator, and k is a control parameter. Here, W is a control parameter chosen to give a maximum weight to the minimum tension criteria when a convergence threshold M is passed. This is done to prevent the denominator from going to zero, i.e. when $\max(d_{rms}) - \min(d_{rms})$ has converged very closely, which would cause $F(c_i)$ to tend to infinity. On an experimental system this would be a highly unlikely case due to measurement errors associated with all processes, however, it has been included for mathematical completeness.

The idea here is that due to $\dfrac{1}{\max(d_{rms}) - \min(d_{rms})}$ in Eq. (2.6), as the genetic algorithm begins to converge closer and closer in flatness, the minimum tension objective will begin to play a larger role. Furthermore, in the ideal case, it will play no role in the first few generations, where reducing wrinkling is more important. Thus, as the flatness values begin to converge, the minimum tension objective will become more important, although it is important to note, not at the expense of

sacrificing any significant amount of flatness. This should be possible as it was noted in [60] that there appears to be a fairly large plateau in the 20-D solution space where there are a large number of possible tension combinations that will result in a minimal membrane flatness value.

The idea behind the adaptive genetic algorithm (AGA) was to reduce the mutation rate when the algorithm begins to converge as mutations are less helpful in this regime. The problem with this approach is that if the mutation is dropped too early, premature convergence may occur as the solution space may not be fully explored. As this may be particularly useful, the reweighting objective function was also combined with the adaptive genetic algorithm. The power of this algorithm, is that although it is very unlikely, in the event that the reweighting objective function begins to yield premature convergence due to the minimum tension criteria, the adaptive genetic algorithm should be able to pull it back out of any local optima by the introduction of new random mutations. The other benefit of this new algorithm is when the mutation rate is reduced, the difference between the maximum and minimum flatness values should become smaller within a run, and allow the minimum tension criteria to work more effectively.

2.2.3 Experimental Results

Figs. 2.7 and 2.8 show the flatness of the membrane using three different control strategies: standard genetic algorithm; reweighting genetic algorithm; and adaptive reweighting genetic algorithm. The flatness is measured as the RMS deviation above the plane of best fit to the membrane surface, with central thermal loading conditions.

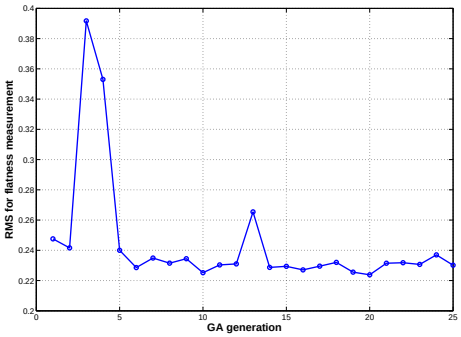

(a) Genetic algorithm

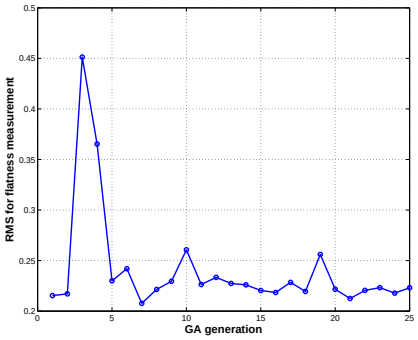

(b) Reweighting GA

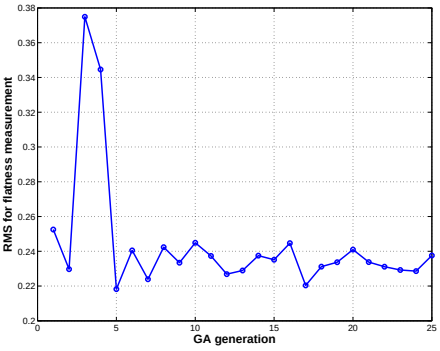

(c) Adaptive reweighting GA

Fig. 2.7 Flatness for 145°C central heat load

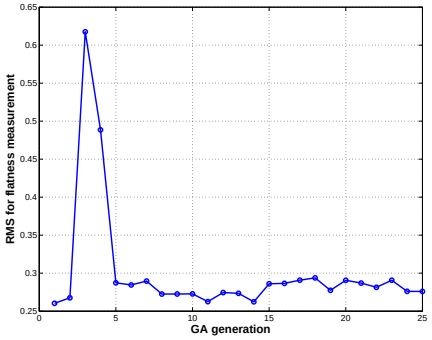

(a) Genetic algorithm

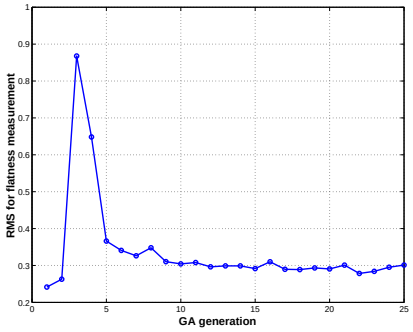

(b) Reweighting GA

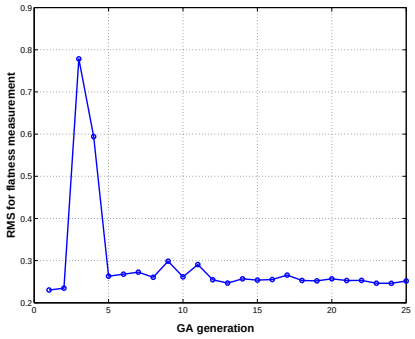

(c) Adaptive reweighting GA

Fig. 2.8 Flatness for 205°C central heat load

Since the reweighting genetic algorithm is designed with the intention of reducing control effort as well as wrinkle amplitudes, Figs. 2.9 and 2.10 show the control effort required for the central 145°C and 205°C heat loading cases, respectively. It can be seen in Figs. 2.9(b)–2.9(c) and Figs. 2.10(b)–2.10(c), that one of the main benefits of using the reweighting genetic algorithms is the reduction of the total tension required to achieve a low flatness value. The standard genetic algorithms,

Figs. 2.9(a) and 2.10(a), require higher tension to be applied.

The performance of all three controllers and their respective tension requirements have been shown in Figs. 2.7 to 2.10. In general, one form of the reweighting objective function appears to give the best results for flatness while continually yielding low tension requirements. It is also interesting to see that for a larger heat load, the adaptive part of the genetic algorithm becomes more important, possibly because the solution plateau in the parameter space is not as broad.

For the 145°C heat load, all of the final RMS deviations of the membrane surface are around 0.235 mm, and lie within 0.025 mm of each other. The required tensions for the online reweighting GA variations are 20 N and 4 N lower respectively than that of the standard GA. For the 205°C heat load, all of the final RMS deviations are around 0.265 mm and lie within 0.04 mm of each other. The required tensions for the online reweighting GA are 7 N and 17 N lower respectively than that of the standard GA. As expected, the membrane is not quite as flat, even under control, when the higher heat load is applied. It can be seen that the reweighting GA's produce surface flatness values that are just as low as the two previous GA formulations, with less tension. While for some cases the tension savings made by the reweighting GA are not huge, the fact that the power will depend on the square of these tension combinations can mean a significant required power reduction.

As a final comparison, Fig. 2.11 shows a comparison of the mutation rates

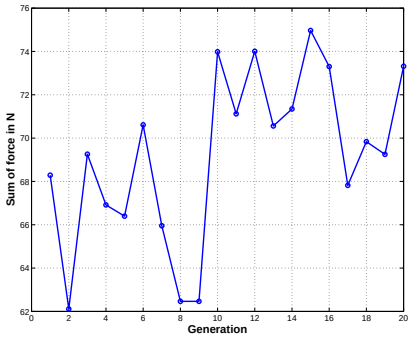

(a) Genetic algorithm

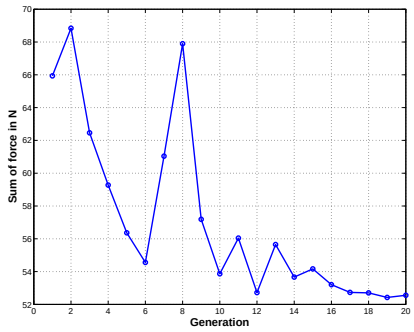

(b) Reweighting GA

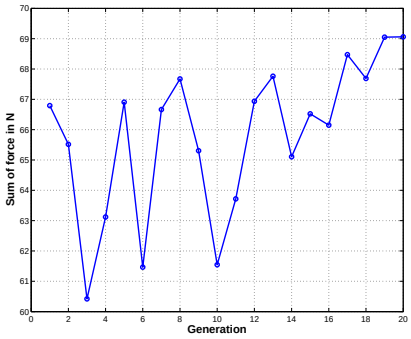

(c) Adaptive reweighting GA

Fig. 2.9 Total tensions for 145°C central heat load

between the adaptive reweighting genetic algorithms for the 145°C and 205°C cases. For the 205°C heat load case the reweighting algorithm varies its mutation rate far more as it searches for an optimal solution to the two objectives.

Finally, two points of particular importance have been noted. The first is that from looking at the flatness plots, it quickly becomes apparent that although the heat loads are the same between different controller runs, the starting flatness value

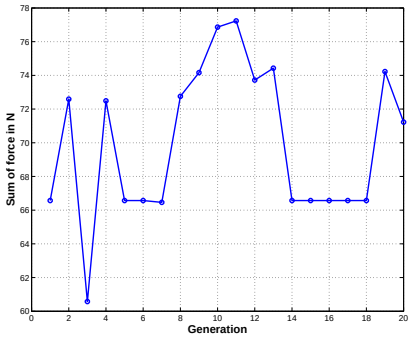

(a) Genetic algorithm

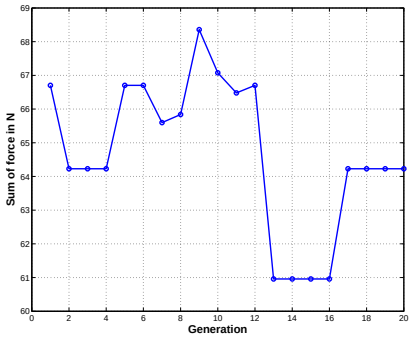

(b) Reweighting GA

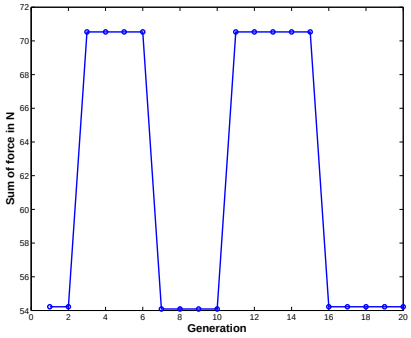

(c) Adaptive reweighting GA

Fig. 2.10 Total tensions for 205°C central heat load

is not, although it is in general similar. This is due to the fact that no tensions are applied at the beginning of the run, and only the heat load is present. Thus, the end condition of the actuators in the previous experiment will influence the first few flatness values obtained in the next experiment. Second, since the genetic algorithm is a stochastic algorithm and is seeded from random values at the beginning, exact duplicates of runs are impossible, and a change in one generation will make changes

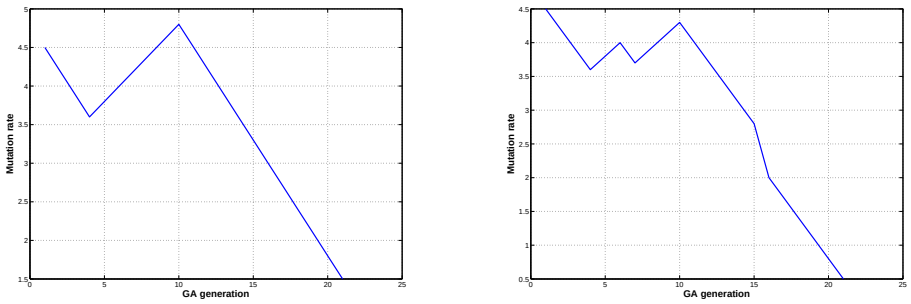

(a) Adaptive reweighting GA, 145°C (b) Adaptive reweighting GA, 205°C

Fig. 2.11 Mutation rates

in all of the rest. This can make repeatability of controller experiments an issue as the same controller, when run twice, will give different results, although the observations show that the results will converge to similar values.

2.3 PWM-PI Control of Shape Memory Alloys

While SMAs typically have a large heat transfer time constant [57,63], the previous performance was often too slow, due to the low current levels of the system. To make more current available to the actuators, and to actuate the SMAs faster and more accurately, a new PWM-PI controller was designed for each actuator. It should also be noted that in the course of this work, the vision system was substantially revised to work faster, and possess better filtering. The flatness variable is also now calculated four times for each iteration (possible due to the increased rate

of the vision system) and averaged to remove any possible dynamic effects from the data.

2.3.1 PWM-PI Control

The discrete incremental version of PI control is implemented as

$$\Delta u(t_k) = K_p[e(t_k) - e(t_{k-1})] + K_i \Delta t e(t_k) \tag{2.7}$$

where $\Delta u(t_k)$ is the force increment, K_p is the proportional gain, K_i is the integral gain, $e(t_k)$ is the error at the current time step, $e(t_{k-1})$ is the error at the previous time step, and Δt is the sampling interval. The output is calculated as

$$u(t_k) = u(t_{k-1}) + \Delta u(t_k) \tag{2.8}$$

where $u(t_{k-1})$ is the previous control commmand. In this case, the error signal is defined as the difference between the desired and measured tensions of the SMA. This type of PI controller is chosen because of its incremental nature, which tends to make the feedback loop less sensitive to the measurement noise from the strain gauges. This is due to the fact that the control signal is incremented from it's previous value as opposed to generating the full command at each time step.

The outputs from the data acquisition card are digital, thus the analog control signal must be digitized by some means. In this study, the intersective type PWM is chosen as it is computationally simple to implement. This type of PWM requires

only sawtooth waveforms (for lead or trail types) and a triangular waveform (for center type) as the modulation signals. When the reference signal, the control command $u(t_k)$ in this case, is larger than the modulation signal, the PWM signal goes on, otherwise it is in it's off state (as can be seen from Fig. 2.12). The triangular wave is shifted by half a period from how it is commonly defined such that the PWM will output in the middle of the period, rather than at the beginning and end.

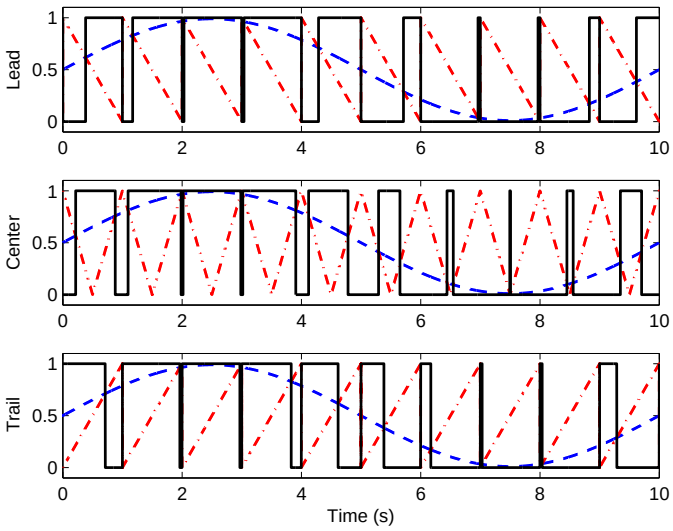

Fig. 2.12 Three types of PWM

In order to prevent the shape memory alloys from possibly being burnt out, the PWM signals to the actuators are designed to possess a duty cycle. This means that the SMA must be off for some portion of the time period specified by

its PWM frequency. For example, consider a constant input value of 1 to PWM set at a frequency of 1 Hz, which would obviously lead to a constant output of 1. Depending on the current limits in the system (and SMA thickness), this could lead to actuator burn out. However, as an example, with a 66% duty cycle, the control is forced off for at least 0.34 seconds of every cycle as can be seen in Fig. 2.13. This also allows the maximum current, under its current limits, to be used more effectively as the control signal for all actuators will not all be on simultaneously. Here, the actuators are numbered according to Fig. 2.1 and will be divided into sets based upon their location around the membrane. The corner actuators (1, 5, 6, 10, 11, 15, 16, 20) are lead type PWM, the in-between actuators (2, 4, 7, 9, 12, 14, 17, 19) are trail type PWM, and the center actuators (3, 8, 13, 18) are center type PWM. Thus it can be seen that lead type PWM will fire on the right edge of the period, trail type will fire on the left edge of the period, and center will fire in the middle of the period (hence the reason for it's time shift).

2.3.1.1 Shape Memory Alloy Tracking Results

For the experiments, the Simulink program is downloaded to the xPC target computer which is configured to have a sample rate of 1 kHz. All twenty controller's for the SMAs are set to the same parameters with the proportional gain set to 5, the integral gain to 0.2, the PWM frequency to 50 Hz, and the duty cycle to 0.75.

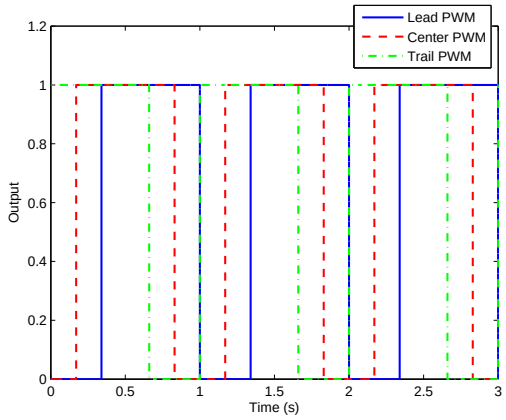

Fig. 2.13 Three types of PWM with duty cycle

In Fig. 2.14 both the tracking performance of the SMA to a step input, over short and long time periods, and the generated control signals can be seen. Here it can be seen that the SMA steps up from 2 to 5 N in less than a second with minimal overshoot or oscillation. In Fig. 2.15, the second shape memory alloy actuator is stepped from 2 N to 7 N in 5 second intervals. It can be seen that the dynamic response of the actuator is different every time. However, the actuator quickly achieves it's desired value and remains there within +/− 0.04 N for the duration of the step. The next test to run is to move all twenty actuators at the same time. An actuator from each of the three set types is selected randomly for plotting as can be seen in Fig. 2.16 (although all 20 are moving). The actuators will begin from whatever their pretensions are, and then move together to a target of 2 N. After 15 seconds, the corner actuators will be sent to 1 N, the middle actuators to

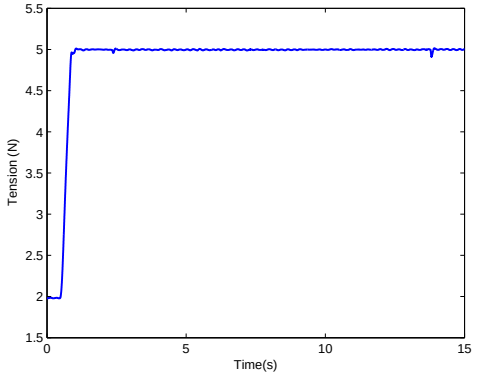

(a) Generated force (N)

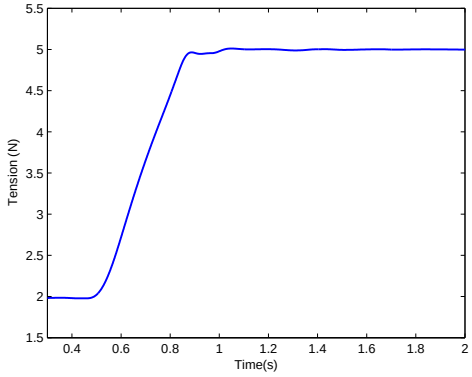

(b) Dynamic response of SMA

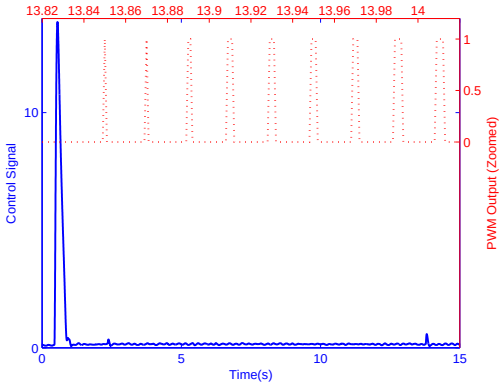

(c) Control signal and digital output

Fig. 2.14 Single SMA tracking performance

5 N, and the between actuators to 3 N as in Fig. 2.16(a). All of the actuators move to their set points, although it can be seen that it takes almost a second longer for them to move than it does for the single actuator operating on its own. This is due to the coupling that the actuator's experience to each other through the membrane, and the fact that they are current limited by the hardware. However,

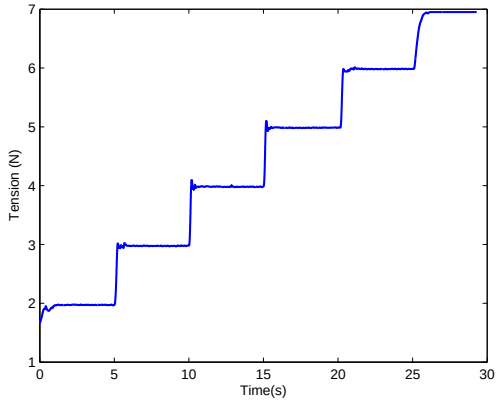

Fig. 2.15 Single SMA tracking performance to multiple steps

all of the desired forces can be maintained as before, within +/− 0.04 N of their target value. Next, in Fig. 2.16(b) all twenty actuators are again set to 2 N to begin, and then to 5 N. Again, it can be seen that it takes slightly longer for all of the actuator's to converge to their desired value. This is particularly true for the center actuator, number 8, as it moved much faster to it's objective in Fig. 2.16(a), even though it is the same set point. Again this is due to the coupling that the actuators experience to each other through the membrane. It also appears that this effect may also partially be due to the how the shape memory alloys connection to the membrane is physically supported, as it is experienced most strongly by the center actuators, and then by the between actuators, and almost not at all by the corner actuators. It is suspected that this is due to the geometry of the membrane structure and support system.

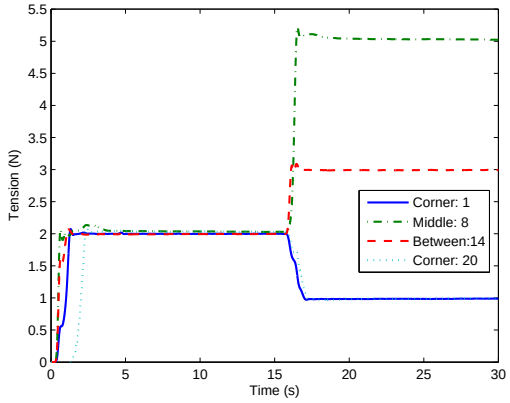

(a) Different setpoints

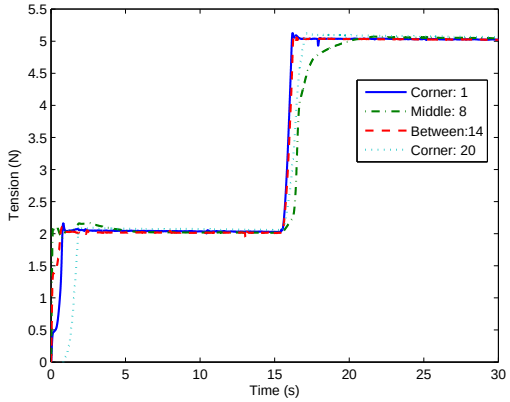

(b) All to 5 N

Fig. 2.16 Twenty actuator tracking performance

2.3.2 Membrane Controller Design

Application of identical tension forces on all the attachment points will cancel out most of the wrinkles which in principle is a very simple controller to implement [64], as it requires only one PI controller that would then implement a tension

for all the actuators. This PI controller was implemented in Matlab to use the membrane flatness as its feedback variable. The control is implemented with a discrete incremental PI controller in the same way as done for the SMA controllers in Eq. 2.7 and 2.8. However, in this case, the error signal is defined as

$$e(t_k) = d_{rms} - d_d \tag{2.9}$$

where d_{rms} is the membrane flatness, d_d is the desired flatness, and $u(t_k)$ will be the desired actuator tension.

2.3.2.1 Experimental Results on Active Flatness Control

At the beginning of the experiment there is no heat applied to the membrane, then for the next two iterations, a 205°C heat load is applied to the membrane. The ceramic heater, and thus the membrane, is allowed to warm up for five minutes before the second measurement. Then, the PI controller is turned on and allowed to run for 30 iterations. Then, the heat load is turned off and the control runs for another 30 iterations. Finally, the ceramic heater is turned back on to 145°C and the control continues for another 30 iterations (the vertical lines in Fig. 2.17-2.18 represent the boundaries of each portion of the experimental run). The PI controller should track the desired RMS deviation of 0.24 mm while either increasing its desired tensions when a heat load induces wrinkling, or loosening its desired tensions when a heat load is not being applied. The camera is the only sensor

providing a feedback variable (d_{rms}) in the master control loop. The calculated tensions will then be supplied to the target computer where the SMAs are being controlled. For the master control loop, the gains are chosen to be $K_p = 1.7$, and $K_i = 0.25$.

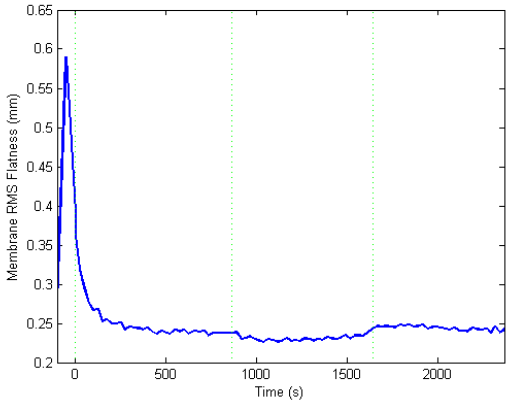

Fig. 2.17 Membrane flatness

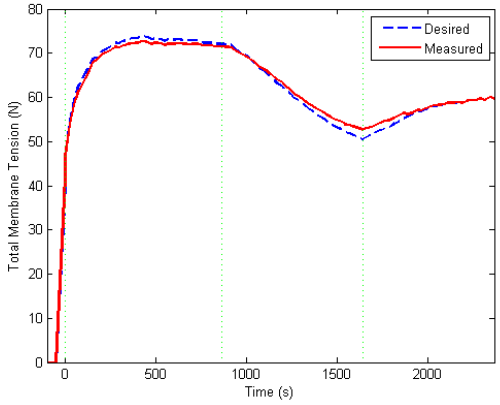

Fig. 2.18 Desired and actual tensions on the membrane

In Fig. 2.17 the time history of the membrane flatness can be seen. The spike before $t = 0$ is when the heater has been on for five minutes, and before any tensions are supplied to the membrane, besides the pretension forces. At $t = 0$, 2 N is applied on all the actuators, and the membrane flatness falls from 0.59 to 0.42. However, the desired flatness value is 0.24, thus, the master PI control loop will increase the tensions up to approximately 73 N total and then level off as can be seen in Fig. 2.18. When the heat load is removed, it can be seen that the RMS flatness will slowly begin to rise, as the tension supplied to the membrane is slowly decreasing. The slow fall of the tensions is due to the membrane beginning to cool down, as it will still be subjected to some thermal loading as the ceramic heater below it also cools down. Finally, when the 145°C heat load is applied in the third section of the plot, it can be seen that once again the tensions will begin to trend upwards as the membrane warms up. After an initial jump in the flatness due to the heat coming on, the control will bring it back down to its desired level. It should be noted that this controller does take a relatively long time as the sampling interval is limited to 25 seconds. This is mainly due to the vision system as four images must be analyzed per interval and the resulting flatness averaged in an attempt to reduce any dynamical effects on the membrane. This process is what takes the most amount of time, as it is rather computationally intensive. However, the shape memory alloy's perform quite satisfactorily in following the desired tension

trajectory on the membrane, with a small error as can be seen in Fig. 2.18.

3 Vibration Control of a Flexible Manipulator using Piezoelectric Sensors and Actuators

Flexible manipulator systems exhibit many advantages over their rigid counterparts. They possess a higher load ratio, and a large increase in the speed of the links is possible. They require less power to produce the same acceleration as the rigid links which have the same load carrying capacity, hence inexpensive and smaller actuators are sufficient. Because of the high performance requirements, consideration of structural flexibility in robots arms is a real challenge. Unfortunately, taking into account the flexibility of the arm leads to the appearance of oscillations at the tips of the links during the motion. These oscillations make the control problems of such systems very difficult. There has been extensive research on active vibration control of flexible systems, see for example [65]. Many control strategies have been used in the control of lightweight flexible structures. These control strategies include, but are not limited to: adaptive control [66], fuzzy logic control [67], H_∞ control [68], and time-optimal control [69].

With the developments in sensor/actuator technologies, many researchers have concentrated on vibration control using smart materials such as shape memory alloys (SMA) and piezoelectric transducers, among others. Piezoelectric materials have been applied in structural vibration control as well as in structural acoustics because of their advantages of fast response, large force output and the fact that they generate no magnetic field in the conversion of electrical energy into mechanical motion. Positive Position Feedback (PPF) was devised by Goh and Caughey [70] and has several distinguished advantages. It has been shown to be a solid vibration control strategy for flexible systems with smart materials, particularly with the PZT (lead zirconium titanate) type of piezoelectric material [71–74]. PPF is essentially a second order filter that is used to apply high frequency gain stabilization by improving the frequency roll-off of the system [23]. Alternatively, PPF works by using a second-order system which is forced by the position response of the structure. This response is then fed back to give the force input to the structure. To apply PPF, the natural frequencies of the structure should be known. The effectiveness of PPF will deteriorate when the natural frequencies are poorly known or have changed due to, for example, the presence of a tip mass.

One of the most successful methods used to control flexible structures is that of input shaping, which can be seen in Fig. 3.1. With this method, a command is convolved with a sequence of impulses, called an input shaper, to produce a

shaped command that causes less vibration than the original unshaped command [75]. The earliest work on input shaping (or command shaping) was conducted by O. J. Smith in the late 1950's [76]. The posicast method proposed by Smith effectively took two impulses whose vibrations were self-canceling and convolved them with the baseline reference command. Due to its sensitivity to frequency uncertainty, the input shaping method was not widely used until robust methods were developed in [75]. So far, more than 700 papers on this subject have been published [77] and input shaping has been implemented on a variety of systems including a large space-based antenna [78], long-reach manipulator [79], crane [80], flexible manipulator [81, 82], and flexible spacecraft [83–89].

There are various versions of the input shaping control technique, such as ZV (Zero-Vibration) shaper [75], ZVD (Zero-Vibration-Derivative) shaper [75], ZVDD (Zero-Vibration-Derivative-Derivative) shaper [75], SI (Specified-Insensitivity) shaper [90], and EI (Extra-Insensitive) shaper [85, 91]. These input shapers can suppress residual vibrations if the system parameters are well known, or the change in model-

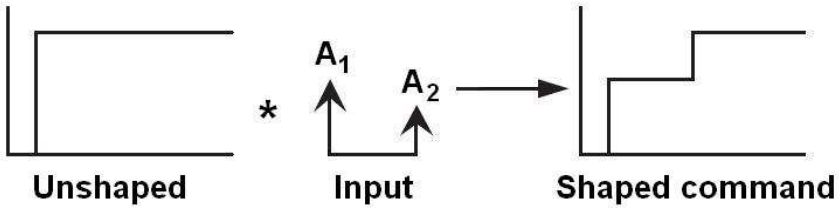

Fig. 3.1 Principle of input shaping

ing parameters is limited to within a reasonable bound. However, if the system has a large range of unknown or varying frequencies, then another approach is needed to make the control methods more robust [92]. One approach is to use adaptive input shaping techniques. Tzes and Yurkovich have proposed online adaptive schemes to update the input shaper parameters [93]. Bodson has used a recursive least-squares technique to tune the input shaper parameters [94]. Kojima and Singhose have proposed an adaptive deflection-limiting input shaping control for slewing flexible space structures [92].

Section 3.3 presents a new approach to overcome the problem of large parameter uncertainties. Rather than using adaptive input shaping techniques, a control strategy is proposed here to combine the input shaping with a multi-mode adaptive PPF control law in order to suppress vibration while slewing the flexible system. Input shaping is used to shape the command in order to minimize the flexible vibration induced by the maneuver. Any residual vibrations will be suppressed by the PZT actuator and the proposed multi-mode adaptive PPF. Hu and Ma have previously combined input shaping with PPF and showed good results for vibration control of a flexible spacecraft [88]. However, for this control method to be effective, the frequencies must be known accurately. A few different forms of adaptive PPF have been developed for constrained stuctures in [95–97], which vary in the way they are implemented. In this portion of the work, input shaping will be

combined with multi-mode adaptive PPF to suppress the vibrations of a slewing flexible manipulator with frequency uncertainty.

As an alternative to adaptation, a genetic algorithm based system identification technique is examined in Section 3.4 for offline identification. There are many standard formulations for system identification, the majority of which are calculus-based. Many procedures have been suggested for system identification including least squares, the prediction error method, and subspace methods among others. However, these methods typically all have drawbacks such as issues with noise, dealing with nonlinearities, and the possibility of getting trapped in local minima. Genetic algorithms (GA), on the other hand are stochastic algorithms that can be guaranteed to converge to within some very close vicinity of the global optima, provided of course that the solution space is well defined. However, GAs sacrifice speed, and typically do poorly at hill-climbing in the vicinity of the global optima, which can be problematic for resonant systems. In [98–101] GAs have been applied for system identification purposes, and in [102] a GA was used to identify a plate structure. In [103], a solution was proposed that combined the GA for global search and a gradient-based search method for hill-climbing when in the vicinity of the global optimum. While this method was shown to give good results, it has a few disadvantages, namely that it can still fail due to nonlinearities or a noisy environment, and that the user is forced to develop two distinct optimization

routines. A system identification is proposed in Section 3.4 based on an iterative implementation of a GA. The solution at the end of one GA run is used to restart the genetic algorithm with a condensed search space based upon the weighted standard deviation of the individuals within the old population. While this method sacrifices speed it allows for a very precise solution and also does not require significant tuning of the genetic algorithm parameters in order to guarantee convergence. Also, the genetic algorithm in this case is used to search for all of the transfer function coefficients. A precise system identification is imperative in this case since the optimality of the controller will depend upon the accuracy of the identification procedure.

Genetic algorithms can also be applied to the controller design problem. In [104] a GA was applied to the problem of designing a pole placement controller, and in [105] to finding the optimal coefficients in the weighting matrix of a LQR/LQG controller. Also, in [106] a fuzzy logic integrated GA was used for vibration control of a cylindrical shell. For PPF it can be time consuming to design each controller, with no guarantee that they will result in optimal vibration suppression. Since, in general, one controller is targeted to one mode, the number of parameters rises rapidly with the number of modes that need to be controlled. In [107] an optimization criteria based on the H_∞-norm of the closed loop systems transfer function is posed. A nonlinear search technique is used to solve for the optimal parameters,

however, a careful initialization procedure must be followed to ensure the solution does not fall into local minima. Using a genetic algorithm in this case offers the additional advantages of lacking an initialization step and being fast and easy for extending the control to any desired number of modes. Some previous attempts have been made to solve for the control parameters of PPF with a genetic algorithm by a far different minimization criteria [108–110], however, only the controller natural frequency parameter is searched for with associated damping and gain parameters assumed. In Section 3.4, the H_∞ criteria posed in [107] is minimized by a genetic algorithm that searches for all the parameters of a two-mode PPF controller. Further, using genetic algorithms for both procedures offers two advantages. The first is that the core GA code is easily extended to more or less modes with trivial alterations. The second is that the exact same GA is used for both the system identification and controller optimization routines.

This chapter is organized as follows: Section 3.1 presents the experimental system and Section 3.2 develops its dynamic model through the finite element method to take into account the presence of the collocated sensor/actuator pair. Section 3.3 presents the development of the combined input shaping plus adaptive positive position feedback control method and its verification through both simulation and experiment. Finally, Section 3.4 presents the development of the GA-based system identification and controller optimization technique. Again, both simulation and

experimental results are presented.

3.1 Experimental System

The experimental setup is shown in Fig. 3.2 and its correpsonding parameters can be seen in Table 3.1. Here the system consists of a very flexible beam with a collocated piezoelectric sensor/actuator pair that is mounted on a DC motor. The two piezoelectrics are Mide QP10W that have been epoxy bonded to the beam. One PZT patch acts as the sensor, and will output a voltage when the beam undergoes deformation, the other patch will act as the actuator, and will strain based upon the voltage supplied to it by the control system. The sensor data can in theory be acquired from the PZT without any additional circuitry, however this is not possible since the terminal board has a finite impedance. This causes the capacitance of the piezoelectric to appear in parallel with the resistance of the measurement device which creates a high pass filtering effect. A simple circuit essentially consisting of a unity gain buffer amplifier with high impedance was built to push the cutoff frequency of the high pass filter well below the frequency range of interest. For the slew experiments, a 4:1 voltage divider is placed before the op amp circuit to prevent saturation due to the large magnitude signals that the slew maneuver produces in the piezoelectric sensor. The piezoelectric actuator is driven by the QPA200 high voltage amplifier which accepts signals between +/– 10 V and can amplify them

linearly to an output range of +/− 200 V. The flexible manipulator is mounted on a HarmonicDrive DC motor RHS-20-3007-E100Al with a rated torque of 24 N·m/A with a differential quadrature encoder generating 4096 pulses/revolution for angular position feedback. The DC motor is controlled by an Advanced Motor Controls Digiflex DPRANIE-015A400A digital servo drive powered by a 24 V DC power supply from OMRON. The sample rate for the control system is chosen as 1 kHz and the entire process is controlled from Simulink through Quanser's Q8 data acquisition board and QuaRC interface for real-time control.

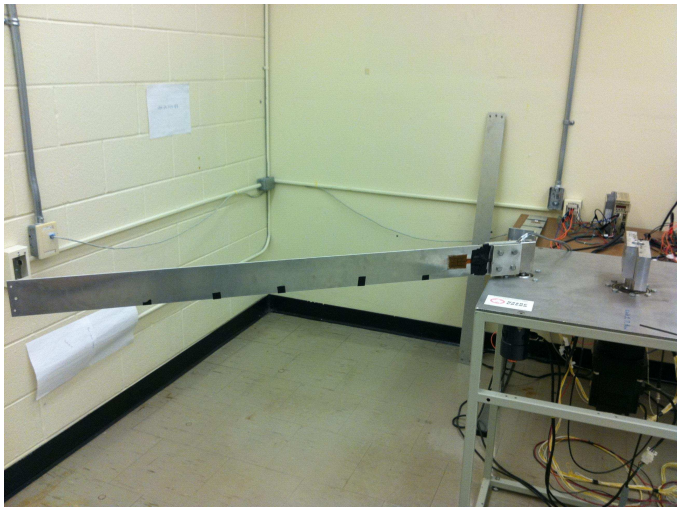

Fig. 3.2 Single-link flexible manipulator

3.2 Dynamic Modeling

Fig. 3.3 shows the diagram of the flexible manipulator being modeled. The flexible manipulator system consists of a rigid hub, a flexible beam, a tip mass, and a collocated piezoelectric sensor/actuator pair. In this study, the flexible manipulator without the piezoelectric sensor/actuator pair will be modeled first using the finite element method and the dynamics equations will be augmented later to consider the effects of the piezoelectric sensor/actuator pair.

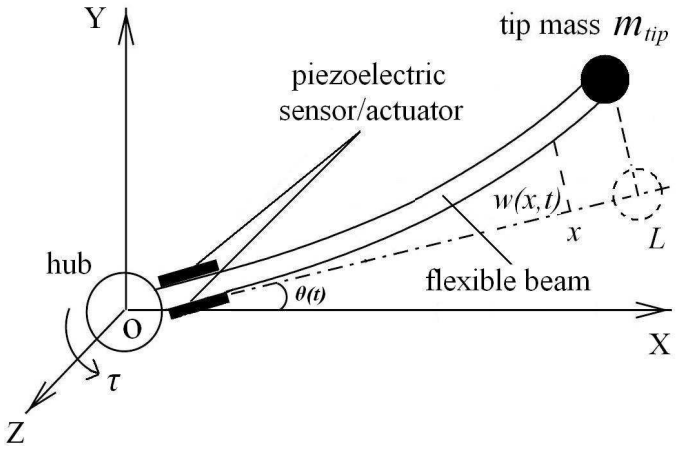

Fig. 3.3 Diagram of flexible manipulator

The kinetic energy of the system assuming an Euler-Bernoulli beam is [111]

$$T = \frac{1}{2}I_h\dot{\theta}^2+\frac{1}{2}\int_0^L \rho A\left[\dot{w}+(b+x)\dot{\theta}\right]^2 dx+\frac{1}{2}m_{tip}\left[(b+L)\dot{\theta}+\dot{w}(L,t)\right]^2+\frac{1}{2}I_{tip}\left[\dot{\theta}+\dot{w}'(L,t)\right]^2 \tag{3.1}$$

where the first term is due to the rigid hub, the second term is due to the energy

of the beam with respect to its velocity normal to x, the third term is due to the tip mass, and the last term is due to the inertia of the tip mass.

The potential energy of the system remains the same as that for a simple beam due to the fact that a rigid body will make no contribution to this term. It can be seen that after discretizing the body into elements, the first elements kinetic energy expression is given by

$$T_1 = \frac{1}{2} I_h \dot{\theta}^2 + \frac{1}{2} \int_0^l \rho A \big[\dot{w} + (b + x + x_i)\dot{\theta}\big]^2 dx \tag{3.2}$$

where l is the length of the element. The i-th element, where $i = 2$ to $n - 1$ will have kinetic energy

$$T_i = \frac{1}{2} \int_0^l \rho A \big[\dot{w} + (b + x + x_i)\dot{\theta}\big]^2 dx \tag{3.3}$$

where x_i is the distance from the root of the beam to the closest side of the i-th beam element. The last element of the beam will have kinetic energy

$$T_n = \frac{1}{2} \int_0^l \rho A \big[\dot{w} + (b + x + x_i)\dot{\theta}\big]^2 dx + \frac{1}{2} m_{tip} \big[(b + L)\dot{\theta} + \dot{w}(L, t)\big]^2 + \frac{1}{2} I_{tip} \big[\dot{\theta} + \dot{w}'(L, t)\big]^2 \tag{3.4}$$

This naturally leads to an augmentation of the traditional Euler-Bernoulli finite

element shape functions to

$$[N]^T = \begin{bmatrix} (b + x_i + x) \\ 1 - 3\left(\frac{x}{l}\right)^2 + 2\left(\frac{x}{l}\right)^3 \\ \frac{x}{l} - 2\left(\frac{x}{l}\right)^2 + \left(\frac{x}{l}\right)^3 \\ 3\left(\frac{x}{l}\right)^2 - 2\left(\frac{x}{l}\right)^3 \\ -\left(\frac{x}{l}\right)^2 + \left(\frac{x}{l}\right)^3 \end{bmatrix} \tag{3.5}$$

While strictly speaking, x_i is a variable in the global sense, it can be treated simply as a constant in the local coordinate system of the elements as it is simply a length offset, which allows the shape functions to be augmented as above.

The mass matrix of each element can then be seen as [111]

$$[M^e] = \rho A \int_0^l [N]^T [N] dx = \begin{bmatrix} M^e_{\theta\theta} & M^e_{\theta w} \\ M^{eT}_{\theta w} & M^e_{ww} \end{bmatrix} \tag{3.6}$$

where

$$M^e_{\theta\theta} = \frac{\rho A l}{3}\left[(x_i + b)^2 + (x_i + b + l)(x_i + b) + (x_i + b + l)^2\right] \tag{3.7}$$

$$M^e_{\theta w} = \rho A l \begin{bmatrix} \frac{3}{20}l + \frac{1}{2}(x_i + b) \\ \frac{1}{30}l^2 + \frac{1}{12}l(x_i + b) \\ \frac{7}{20}l + \frac{1}{2}(x_i + b) \\ -\frac{1}{20}l^2 - \frac{1}{12}l(x_i + b) \end{bmatrix}^T \tag{3.8}$$

$$M^e_{ww} = \frac{\rho A l}{420}\begin{bmatrix} 156 & 22l & 54 & -13l \\ 22l & 4l^2 & 13l & -3l^2 \\ 54 & 13l & 156 & -22l \\ -13l & -3l^2 & -22l & 4l^2 \end{bmatrix} \tag{3.9}$$

As indicated in the kinetic energy expression for the first element, there will be a contribution from the inertia of the rigid hub, thus for the first element $M^e_{\theta\theta}$ becomes

$$M^e_{\theta\theta} = I_h + \frac{\rho A l}{3}\left[(x_i+b)^2 + (x_i+b+l)(x_i+b) + (x_i+b+l)^2\right] \tag{3.10}$$

Similarly, for the last element, there will be a contribution from the mass and inertia of the tip mass, thus for the last element $M^e_{\theta w}$ and M^e_{ww} become

$$M^n_{\theta w} = M^e_{\theta w} + M^e_{\theta t} = \rho A l \begin{bmatrix} \frac{3}{20}l + \frac{1}{2}(x_i+b) \\ \frac{1}{30}l^2 + \frac{1}{12}l(x_i+b) \\ \frac{7}{20}l + \frac{1}{2}(x_i+b) \\ -\frac{1}{20}l^2 - \frac{1}{12}l(x_i+b) \end{bmatrix}^T + \begin{bmatrix} 0 \\ 0 \\ m_{tip}(b+L) \\ I_{tip} \end{bmatrix}^T \tag{3.11}$$

$$M^n_{ww} = M^e_{ww} + M_{wt} = \frac{\rho A l}{420}\begin{bmatrix} 156 & 22l & 54 & -13l \\ 22l & 4l^2 & 13l & -3l^2 \\ 54 & 13l & 156 & -22l \\ -13l & -3l^2 & -22l & 4l^2 \end{bmatrix} + \begin{bmatrix} 0 & 0 & 0 & 0 \\ 0 & 0 & 0 & 0 \\ 0 & 0 & m_{tip} & 0 \\ 0 & 0 & 0 & I_{tip} \end{bmatrix} \tag{3.12}$$

Taking the second spatial derivative of the shape function matrix $[N]$ gives

$$[B]^T = \begin{bmatrix} 0 \\ \frac{1}{l^2}\left[-6 + 12\left(\frac{x}{l}\right)\right] \\ \frac{1}{l}\left[-4 + 6\left(\frac{x}{l}\right)\right] \\ \frac{1}{l^2}\left[6 - 12\left(\frac{x}{l}\right)\right] \\ -\frac{1}{l}\left[2 - 6\left(\frac{x}{l}\right)\right] \end{bmatrix} \tag{3.13}$$

which is simply the shape function matrix for a beam augmented by a zero term. Thus, the element stiffness matrix will be

$$[K^e] = \frac{EI}{l^3}\begin{bmatrix} 0 & 0 & 0 & 0 & 0 \\ 0 & 12 & 6l & -12 & 6l \\ 0 & 6l & 4l^2 & -6l & 2l^2 \\ 0 & -12 & -6l & 12 & -6l \\ 0 & 6l & 2l^2 & -6l & 4l^2 \end{bmatrix} \tag{3.14}$$

For the purpose of illustration, the assembled mass and stiffness matrices of the system for two elements after reduction would look like

$$[M] = \begin{bmatrix} I_h + M^1_{\theta\theta} + M^2_{\theta\theta} & M^1_{\theta w}(1,3) + M^2_{\theta w}(1,1) & M^1_{\theta w}(1,4) + M^2_{\theta w}(1,2) \\ & M^1_{ww}(3,3) + M^2_{ww}(1,1) & M^1_{ww}(3,4) + M^2_{ww}(1,2) \\ & & M^1_{ww}(4,4) + M^2_{ww}(2,2) \\ & symmetric & \\ & & M^2_{\theta w}(1,3) + M_{\theta t}(1,3) \quad M^2_{\theta w}(1,4) + M_{\theta t}(1,4) \\ & & M^2_{ww}(1,3) \quad M^2_{ww}(1,4) \\ & & M^2_{ww}(2,3) \quad M^2_{ww}(2,4) \\ & & M^2_{ww}(3,3) + M_{wt}(3,3) \quad M^2_{ww}(3,4) \\ & & M^2_{ww}(4,4) + M_{wt}(4,4) \end{bmatrix} \tag{3.15}$$

$$[K] = \begin{bmatrix} 0 & 0 & 0 & 0 & 0 \\ & K^1_{ww}(3,3) + K^2_{ww}(1,1) & K^1_{ww}(3,4) + K^2_{ww}(1,2) & K^2_{ww}(1,3) & K^2_{ww}(1,4) \\ & & K^1_{ww}(4,4) + K^2_{ww}(2,2) & K^2_{ww}(2,3) & K^2_{ww}(2,4) \\ & & & K^2_{ww}(3,3) & K^2_{ww}(3,4) \\ & symmetric & & & K^2_{ww}(4,4) \end{bmatrix} \tag{3.16}$$

The assembled and reduced system variables are now

$$\mathbf{q} = \begin{bmatrix} \theta \\ w_2 \\ \theta_2 \\ w_3 \\ \theta_3 \end{bmatrix} \tag{3.17}$$

where w_n and θ_n are the deflection and rotation variables of the nodes.

3.2.1 Piezoelectric Elements in Full System Model

The piezoelectric elements are bonded to both the bottom and top of the beam, and are assumed to have two structural degrees of freedom like the regular beam element. In addition, the piezoelectric element has one electrical degree of freedom which is the voltage. This single degree of freedom is due to the fact that the voltage generated by the piezoelectric is constant over the electrode. The single electrical degree of freedom is used as a sensor or actuator voltage when the material is used as a sensor or actuator.

Voltage can be used as a control input to the actuator, which will cause the actuator to apply moments that are equal and opposite to each other at either end of the element. The bending moment resulting from the voltage input will add a positive bending moment at node 2 and a negative bending moment at node 1. It is assumed that the displacement functions of the PZT will remain the same as that of the regular beam element and that the moments exerted by the piezoelectric actuator act at the nodal points.

In derivation of the piezoelectric beam element, it is assumed that the sensor and actuator have the same width and thickness, and form a collocated sensor-actuator pair. With this assumption, the piezoelectric beam element can be seen as

a sandwich with the regular beam element in the middle with a piezoelectric element bonded on top of it (as actuator) and a piezoelectric element bonded underneath it (as sensor). More details of this method can be found in [73, 112].

Making the same assumptions as for the derivation of the regular beam element, the piezoelectric beam element mass matrix can be obtained as

$$[M^{pe}] = \rho A \int_0^l [N]^T [N] dx \tag{3.18}$$

where

$$\rho A = \rho_b b_b t_b + 2\rho_p b_p t_p \tag{3.19}$$

where l is the length of the piezoelectric element, b_b is the height (or width of the beam), b_p is the width of the piezoelectric material, ρ_b is the density of the beam, ρ_p is the density of the piezoelectric material, t_b is the thickness of the beam, and t_p is the thickness of the piezoelectric patch. Upon inspection, it can be clearly seen that the mass matrix of the piezoelectric element can be written as

$$[M^{pe}] = [M^e] + 2[M_p^e] \tag{3.20}$$

which is the sum of the mass matrix of the regular element, $[M^e]$, plus the mass matrix for the piezoelectric elements on the top and bottom of the beam, $[M_p^e]$.

The piezoelectric beam element stiffness matrix can be obtained as

$$[K^{pe}] = EI \int_0^l [B]^T [B] dx \tag{3.21}$$

where $EI = E_b I_b + 2E_p I_p$, E_b is Young's modulus for the beam, I_b is the inertia of the beam, E_p is Young's modulus for the piezoelectric material, and I_p is the inertia of the piezoelectric element with respect to the neutral axis of the beam. From the parallel axis theorem, $I_p = \frac{1}{12} b_p t_p^3 + b_p t_p \left(\frac{t_p + t_b}{2} \right)^2$.

As for the mass matrix, $[K^{pe}]$ can also be written as

$$[K^{pe}] = [K^e] + 2[K_p^e] \tag{3.22}$$

provided that the inertia of the piezoelectric component is properly defined.

3.2.1.1 Piezoelectric Sensor Equations

The equations for a piezoelectric sensor can be derived from the direct piezoelectric equation under the assumption that there is no external electric field applied to the sensor layer. Thus, the electric displacement is directly proportional to the strain acting on it. For the sensor, the poling will be done along the thickness direction with electrodes on the upper and lower surfaces. Thus, the only non-zero electric displacement component is D_z, which is given by (assuming no external electric field)

$$D_z = d_{31} \sigma_1 \tag{3.23}$$

From Hooke's law in one dimension, it is known that the stress is related to the

strain through the modulus of elasticity, E, as

$$\sigma_1 = E_p \epsilon_1 \tag{3.24}$$

Therefore, the electric displacement becomes

$$D_z = d_{31} E_p \epsilon_1 \tag{3.25}$$

where d_{31} is the relevant electric displacement coefficient. The total charge developed by the strain in the structure will be

$$Q = \iint_A D_z dA \tag{3.26}$$

which upon substitution for D_z becomes

$$Q = d_{31} E_p b_p \int_0^l \epsilon_1 dx \tag{3.27}$$

Since the strain in Euler-Bernoulli beam theory has only one non-zero component of strain, which is along the x-axis, the strain through the beam is given by (here, for simplicity in the derivation, the coordinate corresponding to the rigid mode has been omitted from $\mathbf{q}$ and only the flexible structure is considered)

$$\epsilon_1 = \left(\frac{t_b}{2} + t_p \right) [B]\mathbf{q} \tag{3.28}$$

which upon substitution into the equation for charge [112] becomes

$$Q = d_{31} E_p b_p \left(\frac{t_b}{2} + t_p \right) \int_0^l [B]\mathbf{q} dx \tag{3.29}$$

and evaluating gives

$$Q = d_{31} E_p b_p \left(\frac{t_b}{2} + t_p \right) \left[\begin{array}{cccc} 0 & -1 & 0 & 1 \end{array} \right] \mathbf{q} \tag{3.30}$$

The capacitance of the piezoelectric sensor [21] can be shown as

$$C = \frac{l b_p e_{33}^{\sigma}}{t_p} \tag{3.31}$$

which means that the voltage generated by the sensor is given as

$$V_s = G_s \frac{Q}{C_p} = \frac{G_s d_{31} E_p t_p \left(\frac{t_b}{2} + t_p \right) \left[\begin{array}{cccc} 0 & -1 & 0 & 1 \end{array} \right] \mathbf{q}}{l e_{33}^{\sigma}} \tag{3.32}$$

where G_s is the sensor signal conditioning gain. Letting

$$\mathbf{p} = \frac{G_s d_{31} E_p t_p \left(\frac{t_b}{2} + t_p \right)}{l e_{33}^{\sigma}} \left[\begin{array}{c} 0 \\ -1 \\ 0 \\ 1 \end{array} \right] \tag{3.33}$$

the equation for the voltage developed can be simplified to

$$V_s(t) = \mathbf{p}^T \mathbf{q} \tag{3.34}$$

3.2.1.2 Piezoelectric Actuator Equations

For the piezoelectric actuator, the sensor voltage is typically applied as a control signal to the actuator after being modified by a control law, and then multiplied by another gain G_a, which is usually supplied by means of an amplifier. Therefore the actuator voltage is given by

$$V_a(t) = G_a V_{in}(t) \tag{3.35}$$

The applied electric field in the actuator is due to the applied voltage, therefore the electric field is given by

$$E_f = \frac{V_a(t)}{t_p} \tag{3.36}$$

The strain created in the actuator by the applied electric field can then be described as

$$\epsilon_a = d_{31} E_f \tag{3.37}$$

and once again using Hooke's law in one dimension gives the stress as

$$\sigma_a = \frac{E_p d_{31} V_a(t)}{t_p} \tag{3.38}$$

Due to the stress in the structure, bending moments will act in an equal and opposite manner at the two nodal points. Since the piezoelectric element will typically have a small cross-section, it is assumed that the moments exerted by the patch essentially act at the nodal points [112]. The expression for the bending moment in the small cross-section is given by

$$M_a = b_p \int_{\frac{t_b}{2}}^{\frac{t_b}{2}+t_p} \sigma_a z dz \tag{3.39}$$

which upon substitution for the stress gives

$$M_a = \frac{E_p d_{31} V_a(t) b_p}{t_p} \int_{\frac{t_b}{2}}^{\frac{t_b}{2}+t_p} z dz \tag{3.40}$$

which upon evaluation of the integral gives

$$M_a = E_p d_{31} V_a(t) b_p \left(\frac{t_p + t_b}{2} \right) \tag{3.41}$$

The control force, or force exerted by the actuators due to the applied control voltage can be derived as (here again note that the rigid coordinate has been omitted)

$$\mathbf{f}_p = E_p d_{31} b_p V_a(t) \left(\frac{t_p + t_b}{2} \right) \int_0^l [B]^T dx \tag{3.42}$$

which after carrying through the integration and substituting in Eq. (3.35) becomes

$$\mathbf{f}_p = E_p d_{31} b_p G_a V_{in}(t) \left(\frac{t_p + t_b}{2} \right) \begin{bmatrix} 0 \\ -1 \\ 0 \\ 1 \end{bmatrix} \tag{3.43}$$

Letting

$$\mathbf{h} = G_a E_p d_{31} b_p \left(\frac{t_p + t_b}{2} \right) \begin{bmatrix} 0 \\ -1 \\ 0 \\ 1 \end{bmatrix} \tag{3.44}$$

the control force equation becomes

$$\mathbf{f}_p = \mathbf{h} V_{in}(t) \tag{3.45}$$

3.2.2 Additional Piezoelectric Considerations

For completeness it should be noted that the vectors **p** and **h** will have all of their elements shifted down one position to make room for a zero at the location of the first element corresponding to the fact that their influence is not exerted at the location of the hub.

3.2.3 System Assembly, Reduction, and Modal Decoupling

The entire second-order differential equation can be assembled using the standard finite element technique with Rayleigh damping included as

$$[M]\ddot{\mathbf{q}} + [D]\dot{\mathbf{q}} + [K]\mathbf{q} = \mathbf{F} \tag{3.46}$$

where $[M]$, $[D]$, and $[K]$ are the global mass, damping, and stiffness matrices.

Modal decoupling can be performed to obtain the normal mode system through similarity transformations [113] giving

$$\ddot{\mathbf{x}} + Z\dot{\mathbf{x}} + \Omega\mathbf{x} = S_m^T\mathbf{F} \tag{3.47}$$

where S_m is the matrix of mass normalized eigenvectors.

3.3 Combined Input Shaping and Adaptive Positive Position Feedback

The slewing motion of the hub is controlled using a simple PD feedback law as

$$\tau(t) = K_p(\theta_d - \theta) + K_d(\dot{\theta}_d - \dot{\theta}) \tag{3.48}$$

where θ is the actual hub angle, θ_d is the desired angle, K_p and K_d are the proportional and derivative gains, respectively. Of course for either disturbance rejection or step-following, the slewing motion of the hub generates vibrations in the flexible

appendage which need to be controlled using other control laws. To do this, the PD controller will be combined with input shaping.

3.3.1 Input Shaping

Basically, any type of input shaper can be combined with the proposed multi-mode adaptive PPF control for vibration suppression. Here, for simplicity, three simple shapers (ZV, ZVD, and ZVDD) will be used.

The ZV shaper is a 2-impulse input shaper that can achieve zero vibration after the last (2nd) impulse. The amplitudes and time instants of two impulses are as follows

$$\begin{aligned} A_1 &= \frac{1}{1+K}, \qquad t_1 = 0 \\ A_2 &= \frac{K}{1+K}, \qquad t_2 = \frac{\pi}{\omega_d} \end{aligned}$$

where $K = \exp\left(-\frac{\xi\pi}{\sqrt{1-\xi^2}} \right)$, ξ is the damping ratio, ω_d is the damped natural frequency. The ZV shaper can be used to achieve zero vibration if the natural frequency and damping ratio are known exactly. However, the residual vibration will be large if the uncertainty in the natural frequency is large. In other words, the ZV shaper is not robust.

The robustness of the input shaper to uncertainty in the system's natural frequencies can be increased by setting the derivative to zero. Setting the derivative to

zero is the equivalent of producing small changes in vibration with corresponding changes in the natural frequency [114]. This yields a three-impulse ZVD shaper with parameters

$$\begin{aligned} A_1 &= \frac{1}{1+2K+K^2}, & t_1 &= 0 \\ A_2 &= \frac{2K}{1+2K+K^2}, & t_2 &= \frac{\pi}{\omega_d} \\ A_3 &= \frac{K^2}{1+2K+K^2}, & t_3 &= 2t_2 \end{aligned}$$

The robustness of the input shaper can further be increased by setting the second derivative to zero. Similarly, this yields a four-impulse ZVDD shaper with parameters

$$\begin{aligned} A_1 &= \frac{1}{1+3K+3K^2+K^3}, & t_1 &= 0 \\ A_2 &= \frac{3K}{1+3K+3K^2+K^3}, & t_2 &= \frac{\pi}{\omega_d} \\ A_3 &= \frac{3K^2}{1+3K+3K^2+K^3}, & t_3 &= 2t_2 \\ A_4 &= \frac{K^3}{1+3K+3K^2+K^3}, & t_4 &= 3t_2 \end{aligned}$$

The sensitivity curves for these three input shapers are shown in Fig. 3.4. It can be seen that, for the same residual vibration level, the ZVDD shaper allows much more uncertainty in the frequency than the ZV shaper.

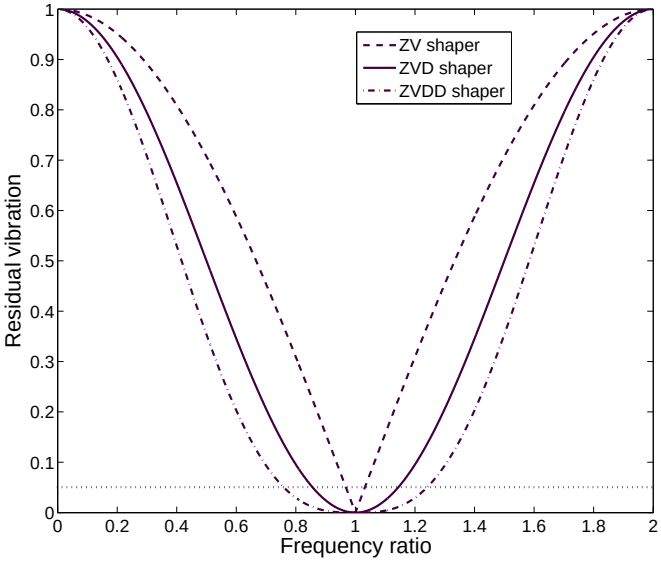

Fig. 3.4 Sensitivity curves of various input shapers

3.3.2 Positive Position Feedback

Considering the scalar case first, PPF can be described by two coupled differential equations where the first equation describes the structure, and the second describes the compensator [72] as

$$\begin{aligned} \ddot{\xi} + 2\zeta\omega\dot{\xi} + \omega^2\xi &= g\omega^2\eta \\ \ddot{\eta} + 2\zeta_f\omega_f\dot{\eta} + \omega_f^2\eta &= \omega_f^2\xi \end{aligned} \tag{3.49}$$

where ξ is the modal coordinate, η is the filter coordinate, ζ and ζ_f are the structural damping and filter damping ratios, ω and ω_f are the structural natural frequency and filter frequency, and g is the scalar gain. It is shown in [72] that the necessary

and sufficient condition for stability is

$$0 < g < 1 \tag{3.50}$$

The major advantage of PPF is that the transfer function of the controller rolls off quickly, as can be seen from its Bode plot in Fig. 3.5. This is good because it makes the PPF controller well-suited for control of low-frequency modes of a structure with well-separated modes. This is also a major advantage due to the fact that the system will be not be influenced by unmodeled high frequency dynamics. Hence, all spillover into uncontrolled or unmodelled modes is stabilizing [72].

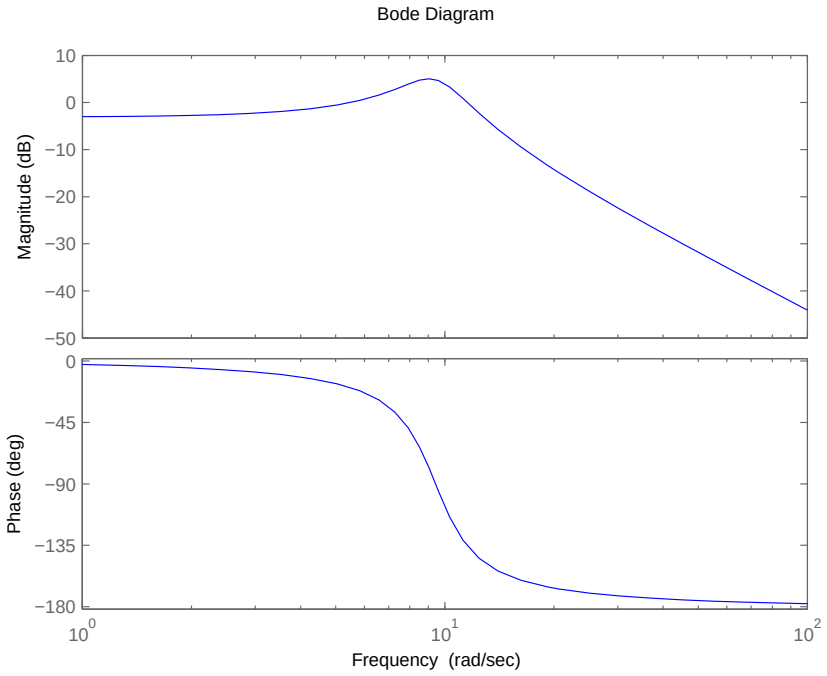

Fig. 3.5 Bode plot for a single mode PPF controller

There are three possible output conditions for a PPF controller based upon the choice of controller frequency ω_c: *active flexibility*, *active damping*, or *active stiffness* [74]. In order to effectively damp out a structural mode, obviously the case of active damping is required. Thus the controller frequency should be selected to be close to the modal frequency.

In theory, a flexible manipulator has infinite vibrational modes, and sometimes there is more than one dominant mode. In order to damp the dominant modes, multiple PPF controllers are required in parallel, where each controller is tuned to the natural frequency of the mode it is to damp. In our system, the first two vibration modes are dominant and need to be suppressed. This means that the frequency of η_1 is chosen to be close to that of ξ_1 while the frequency of η_2 is chosen to be close to that of ξ_2.

For the general multi-variable case, the system of equations becomes

$$\begin{aligned} \ddot{\boldsymbol{\xi}} + D\dot{\boldsymbol{\xi}} + \Omega\boldsymbol{\xi} &= C^T G\boldsymbol{\eta} \\ \ddot{\boldsymbol{\eta}} + D_f\dot{\boldsymbol{\eta}} + \Omega_f\boldsymbol{\eta} &= \Omega_f C\boldsymbol{\xi} \end{aligned} \tag{3.51}$$

where G is the diagonal gain matrix, C is the participation matrix, Ω and Ω_f are the diagonal modal and filter frequency matrices, and D and D_f are the diagonal modal and filter damping matrices. In this case, stability can be guaranteed [72] if and only if

$$\Omega - C^T GC > 0 \tag{3.52}$$

Considering for a moment, only the flexible modes of the structure, a positive position feedback controller is developed in this section for the beam using a single collocated PZT sensor/actuator pair. The dynamic equation of the structure in modal coordinates is

$$\ddot{x} + Z_s\dot{x} + \Omega_s x = S_m^T h u \tag{3.53}$$

where x is the vector of modal coordinates, Z_s is the damping matrix, Ω_s is the frequency matrix, S_m^T is the matrix of mass normalized eigenvectors of the system, h is the actuator influence matrix, and u is the input to the actuator (voltage in this case). The sensor (or output) equation can be seen as

$$y = p^T S_m x \tag{3.54}$$

where p is the sensor influence matrix.

The equation describing the controller is given as

$$\ddot{\eta} + Z_f\dot{\eta} + \Omega_f \eta = \Omega_f E y \tag{3.55}$$

where η is the vector of controller coordinates, Z_f is the controller damping matrix, Ω_f is the controller frequency matrix, and E is the modal participation factor matrix, which will be defined shortly. The actuator input equation is given as

$$u = E^T G \eta \tag{3.56}$$

where G is the gain matrix.

Since S_m^T is the matrix of mass normalized eigenvectors, the modal participation factor matrix can be defined as

$$E = S_m^T M r \tag{3.57}$$

where M is the global mass matrix of the system, and r is a matrix of ones with the same number of rows as M, and the number of columns equal to the number of collocated sensor/actuator pairs.

The four equations, i.e. Eqs. (3.53–3.56), describing the system can be combined into two second order differential equations as

$$\ddot{x} + Z_s \dot{x} + \Omega_s x = S_m^T h E^T G \eta \tag{3.58}$$

$$\ddot{\eta} + Z_f \dot{\eta} + \Omega_f \eta = \Omega_f E p^T S_m x \tag{3.59}$$

Now the structure and controller equations will be placed into state space (or first order form) for ease of analysis. The structural equations become

$$\dot{\hat{x}} = A\hat{x} + Bu \tag{3.60}$$

$$y = C\hat{x} \tag{3.61}$$

where

$$A = \begin{bmatrix} 0 & I \\ -\Omega_s & -Z_s \end{bmatrix} \quad B = \begin{bmatrix} 0 \\ S_m^T h \end{bmatrix} \quad C = \begin{bmatrix} p^T S_m & 0 \end{bmatrix}$$

and the controller equations become

$$\dot{\hat{\eta}} = \hat{A}\hat{\eta} + \hat{B}y \tag{3.62}$$

$$u = \hat{C}\hat{\eta} \tag{3.63}$$

where

$$\hat{A} = \begin{bmatrix} 0 & I \\ -\Omega_f & -Z_f \end{bmatrix} \quad \hat{B} = \begin{bmatrix} 0 \\ \Omega_f E \end{bmatrix} \quad \hat{C} = \begin{bmatrix} E^T G & 0 \end{bmatrix}$$

3.3.3 Adaptive Parameter Estimation

Since the structural transfer function is single-input and single-output (SISO), it can be put in transfer function form through

$$G(s) = \frac{Z(s)}{R(s)} = C(sI - A)B \tag{3.64}$$

where

$$R(s) = s^n + a_{n-1}s^{n-1} + ... + a_1 s + a_0 \tag{3.65}$$

$$Z(s) = b_m s^m + ... + b_1 s + b_0 \tag{3.66}$$

which allows the adaptive law to be developed generically.

The output of the system is of the following form

$$y = G(s)u = \frac{Z(s)}{R(s)}u \tag{3.67}$$

where u is the input of the plant, and the output can also be expressed as [115]

$$y^{(n)} + a_{n-1}y^{(n-1)} + ... + a_1\dot{y} + a_0 y = b_m u^{(m)} + ... + b_1\dot{u} + b_0 u \tag{3.68}$$

Lumping all of the unknown parameters into the vector

$$\Phi = \begin{bmatrix} b_m & ... & b_0 & a_{n-1} & ... & a_0 \end{bmatrix}^T \tag{3.69}$$

and filtering both sides of Eq. (3.68) with the following monic Hurwitz polynomial [115]

$$\frac{1}{\Lambda(s)} = \frac{1}{s^n + \lambda_{n-1}s^{n-1} + ... + \lambda_1 s + \lambda_0} \tag{3.70}$$

the static parametric model can be obtained as [115]

$$z = \Phi^T \phi \tag{3.71}$$

where

$$\begin{aligned} z &= \frac{s^n}{\Lambda(s)} y \\ \phi &= \begin{bmatrix} \frac{s^m}{\Lambda(s)}u & \cdots & \frac{1}{\Lambda(s)}u & -\frac{s^{n-1}}{\Lambda(s)}y & \cdots & -\frac{1}{\Lambda(s)}y \end{bmatrix}^T \end{aligned}$$

The estimation model can now be defined as

$$\hat{z} = \hat{\Phi}^T \phi \tag{3.72}$$

where $\hat{z}$ and $\hat{\Phi}$ is the estimate of z and Φ at each time t. The estimation error can then be defined as

$$\epsilon = \frac{z - \hat{z}}{m_s^2} = \frac{z - \hat{\Phi}^T \phi}{m_s^2} \tag{3.73}$$

where m_s^2 is referred to as the normalizing signal and is designed to bound ϕ from above [115]. A typical choice for the normalizing signal is

$$m_s^2 = 1 + \alpha \phi^T \phi \tag{3.74}$$

where $\alpha > 0$.

The cost function is a convex function of $\hat{\Phi}$ with a global minimum and is given by

$$J(\hat{\Phi}) = \frac{1}{2}\int_0^t e^{-\beta(t-\tau)}\frac{[z(\tau) - \hat{\Phi}^T(t)\phi(\tau)]^2}{m_s^2(\tau)}d\tau + \frac{1}{2}e^{-\beta t}(\hat{\Phi} - \hat{\Phi}_0)^T Q_0(\hat{\Phi} - \hat{\Phi}_0) \quad (3.75)$$

where $Q_0 = Q_0^T > 0$, $\beta > 0$ are design constants, and $\hat{\Phi}_0 = \hat{\Phi}(0)$ is the initial parameter estimates of the unknowns.

This cost function serves to deweight previous data and includes a penalty on the error in the initial guess. The recursive least squares algorithm with forgetting factor is obtained as [115]

$$\dot{\hat{\Phi}} = P\epsilon\phi \quad (3.76)$$

$$\dot{P} = \begin{cases} \beta P - P\dfrac{\phi\phi^T}{m_s^2}P & \|P\| \leq R_0 \\ 0 & \text{otherwise} \end{cases} \quad (3.77)$$

where $P(0) = P_0 = Q_0^{-1}$. Here, R_0 is a scalar that serves as an upper bound for $\|P\|$, since in this case, with $\beta > 0$, $P(t)$ may grow without bound.

3.3.4 Combining the System

Considering the full system, the state space model can be transformed into transfer function form through the relation

$$H(s) = C(sI - A)^{-1}B + D \quad (3.78)$$

Due to the fact that there are two outputs (hub angle and sensor voltage) and two inputs (torque and actuator voltage) in the system, $H(s)$ becomes a 2×2 transfer function matrix, given for the open loop by

$$\begin{bmatrix} \theta(s) \\ V_s(s) \end{bmatrix} = \begin{bmatrix} G_{11}(s) & G_{12}(s) \\ G_{21}(s) & G_{22}(s) \end{bmatrix} \begin{bmatrix} \tau \\ V_c \end{bmatrix} \tag{3.79}$$

As a generic case, which can be extended or simplified with relative ease, the system is chosen to consider the rigid mode and two flexible modes with A, B, and C given as

$$A = \begin{bmatrix} 0 & 0 & 0 & 1 & 0 & 0 \\ 0 & 0 & 0 & 0 & 1 & 0 \\ 0 & 0 & 0 & 0 & 0 & 1 \\ 0 & 0 & 0 & 0 & 0 & 0 \\ 0 & -\Omega_1 & 0 & 0 & -z_1 & 0 \\ 0 & 0 & -\Omega_2 & 0 & 0 & -z_2 \end{bmatrix} \quad B = \begin{bmatrix} 0 & 0 \\ 0 & 0 \\ 0 & 0 \\ a & b \\ c & d \\ e & f \end{bmatrix} \quad C = \begin{bmatrix} p & q & r & 0 & 0 & 0 \\ t & u & v & 0 & 0 & 0 \end{bmatrix}$$

In this case, the four transfer functions can be found through Eq. (3.78) as

$$\begin{aligned} G_{11}(s) &= \frac{m_1 s^4 + m_2 s^3 + m_3 s^2 + m_4 s + m_5}{s^2(s^2 + z_1 s + \Omega_1)(s^2 + z_2 s + \Omega_2)} \\ G_{12}(s) &= \frac{(qd + rf)s^2 + (rfz_1 + qdz_2)s + (rf\Omega_1 + qd\Omega_2)}{(s^2 + z_1 s + \Omega_1)(s^2 + z_2 s + \Omega_2)} \\ G_{21}(s) &= \frac{(uc + ve)s^2 + (vez_1 + ucz_2)s + (ve\Omega_1 + uc\Omega_2)}{(s^2 + z_1 s + \Omega_1)(s^2 + z_2 s + \Omega_2)} \\ G_{22}(s) &= \frac{(ud + vf)s^2 + (vfz_1 + udz_2)s + (vf\Omega_1 + ud\Omega_2)}{(s^2 + z_1 s + \Omega_1)(s^2 + z_2 s + \Omega_2)} \end{aligned}$$

where $m_1 = (qc + re + pa)$, $m_2 = (rez_1 + qcz_2 + paz_1 + paz_2)$, $m_3 = (pa\Omega_2 + paz_1z_2 + re\Omega_1 + pa\Omega_1 + qc\Omega_2)$, $m_4 = (paz_1\Omega_2 + pa\Omega_1z_2)$, and $m_5 = pa\Omega_1\Omega_2$. In the simplification of the last three transfer functions the fact that b and t tend to

zero have been used to reduce the order of the individual transfer functions. This simplification is made due to the fact that if b tends to zero, this implies that control voltage on the piezos does not directly affect the hub angle, and with t tending to zero implies that the hub angle does not directly affect the sensor voltage produced.

For the control system, the step command is shaped by an input shaper outside of the loop, with a PD controller inside the closed-loop for the rigid hub motion. The estimator is on at the beginning with arbitrary initial guesses, and is set up to adapt on $G_{21}(s)$, which is between the sensor voltage and the torque. The estimator is modified to turn off when the error

$$\epsilon = \frac{z - \hat{z}}{m_s^2} = \frac{z - \hat{\Phi}^T \phi}{m_s^2} < 0.1 \tag{3.80}$$

for longer than one second, and then to turn on the multi-mode adaptive PPF controller. This is done since at this point, the parameter estimates will have converged within a reasonable amount (as ϵ represents the difference between the actual transfer function and estimated transfer function), and adaptation is no longer needed. The second reason this is done, is that after a few seconds of running, the PPF controller may start to eliminate the vibrations in the structure and the persistence of excitation condition may no longer be valid, leading to possibly erroneous estimates of the natural frequencies as control is applied.

3.3.5 Simulation Results

The physical properties of the system and the simulation parameters are listed in Table 3.1. Finite element analysis shows that the actual frequencies of the first two vibration modes are 1.7141 Hz and 10.4337 Hz, and they are assumed to be known with uncertainties. It is desired to slew the rigid hub 0.5 radians which is done by a PD control law. Saturation is included on the input and output of the PZT sensor and actuator at +/− 10 V to keep the system physically realistic.

Table 3.1 System and simulation parameters

Parameter	Value	Description
I_h	10 kg·m^2	Hub inertia
b	0.11715 m	Hub radius
l	1.1365 m	Length of the beam
t	0.00258 m	Thickness of the beam
h	0.0828 m	Height of the beam
ν	0.33	Poisson's ratio of the beam
ρ	2700 kg/m^3	Density of the beam
E	70 GPa	Modulus of elasticity for the beam
l_p	0.05084 m	Length of the piezoelectric
b_p	0.03806 m	Width of the piezoelectric
t_p	0.00038 m	Thickness of the piezoelectric
ν_p	0.3	Poisson's ratio of the piezoelectric
ρ_p	7700 kg/m^3	Density of the piezoelectric
E_p	68 GPa	Modulus of elasticity for the piezoelectric
m_{tip}	0	Tip mass
I_{tip}	0	Inertia of tip mass
d_{31}	-171 x 10^{-12} C/N	Electric displacement coefficient
e^{σ}_{33}	1.5317 x 10^{-8} F/m	Permittivity
G_s	1	Sensor gain
G_a	20	Actuator amplifier gain
s_p	0.06559 m	Start location of piezoelectric from root of beam

In this study, three simulation scenarios are considered: (1) PD control only; (2) PD control with adaptive PPF; and (3) PD control with input shaping and adaptive PPF. The proportional gain is chosen to be $K_p = 55$ and the derivative gain is set to be 45 and the initial parameter guess as $\hat{\Phi}_0 = [1 \;\; 1 \;\; 1 \;\; 1 \;\; 1 \;\; 1 \;\; 1]^T$.

First, PD feedback is applied to control the hub angle, however, neither input shaping nor multi-mode adaptive PPF is used. Since no active vibration control is used, the vibration of the flexible beam is quite large, as seen in Fig. 3.6.

To suppress flexible vibration, in the next simulation, the proposed multi-mode adaptive PPF controller is added to suppress the vibration of the first two modes. The simulation results are shown in Fig. 3.6 for comparison. It can be seen from the simulation results that the flexible vibration has been suppressed to a very low level after 18 sec using the proposed adaptive PPF controller. It also shows that, at about 10 sec, the parameter estimator successfully estimated the first two natural frequencies to be 1.7143 Hz and 10.4327 Hz, respectively, which are very close to the true values. Once the estimation is done, the PPF controllers are turned on.

Finally, the input shaping and adaptive positive position feedback are combined to suppress vibration. Input shaping is designed to suppress the first flexible vibration mode during slewing. Due to the frequency uncertainty, however, there will be residual vibration, which will be suppressed through the PZT actuator with multi-mode adaptive PPF. Here, three input shapers are used in the simulations,

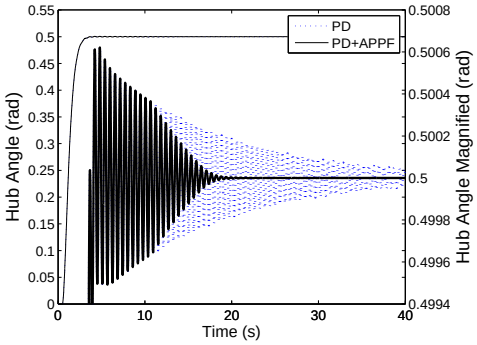

(a) Hub angle response

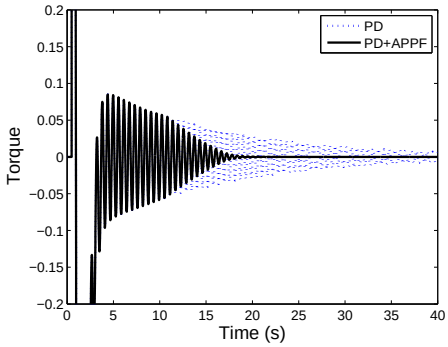

(b) Output control torque

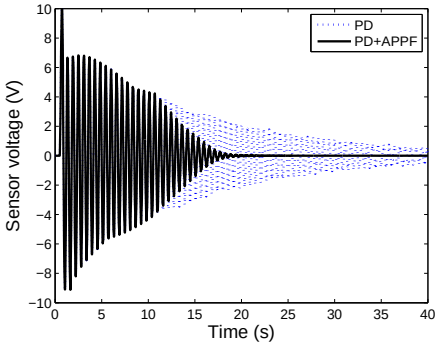

(c) PZT sensor voltage

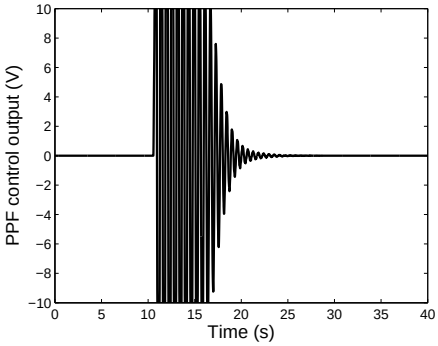

(d) Control voltage from PPF

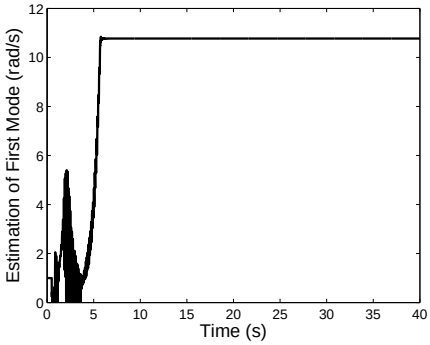

(e) Estimation of the first natural frequency

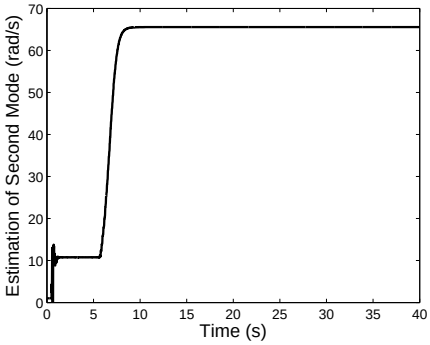

(f) Estimation of the second natural frequency

Fig. 3.6 Simulation results of PD control with multi-mode adaptive PPF

the ZV shaper, ZVD shaper, and ZVDD shaper. Moreover, two frequency uncertainty levels (10% high and 50% high) are considered for the first vibration mode. For comparison purposes, PD control with input shaping is also applied to slew the manipulator in order to suppress the vibration. The simulation results have been included in the figures corresponding to which shaper the adaptive PPF is combined with. Figs. 3.7–3.12 show the hub angle response, torque control output, PZT sensor output, PZT actuator control input and frequency estimation for those simulations. Table 3.2 shows the estimated frequencies of the first two vibration modes and the times for the estimation to be done. It can be seen that (i) the frequencies of the first and second mode can be estimated accurately for all the cases; (ii) the vibrations have been suppressed very well and quickly by combining the input shaping and the adaptive PPF strategy.

Table 3.2 Estimation results of the first two frequencies (Hz)

Input shaper type	Estimated frequencies	
	Frequency uncertainty: +50%	Frequency uncertainty: +10%
ZV	1.7141, 10.4323 (∼5 sec)	1.7141, 10.4308 (∼6 sec)
ZVD	1.7141, 10.4323 (∼6 sec)	1.7141, 10.4223 (∼7 sec)
ZVDD	1.7141, 10.4323 (∼5 sec)	1.7130, 10.4209 (∼10 sec)

In Fig. 3.7, the results of applying the ZV shaper, and the ZV shaper with the adaptive PPF can be seen for the case when the first mode is off by +50%. The advantages of using the combined control law (PD+IS+APPF) can be seen as the ZV shaper alone will still have residual vibration at the end of the simulation, while

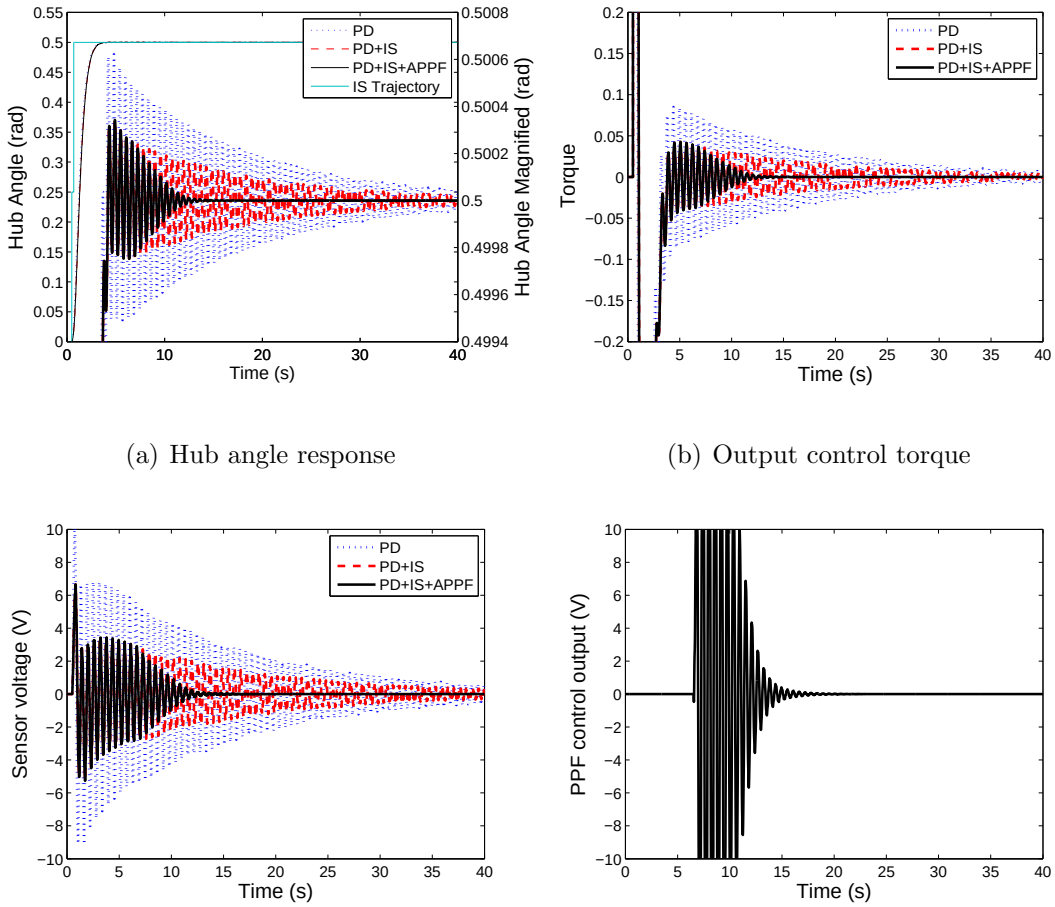

(a) Hub angle response

(b) Output control torque

(c) PZT sensor voltage

(d) Control voltage from PPF

Fig. 3.7 Simulation results with multi-mode adaptive PPF and ZV input shaper (frequency uncertainty: +50%)

the combined law has no residual vibration after roughly 12 seconds. When the frequency uncertainty is only +10% as in Fig. 3.8, the control with only the ZV shaper will again still have residual vibration at the end of the simulation (although at a much lower level than that of the previous case). Here, the combined law has

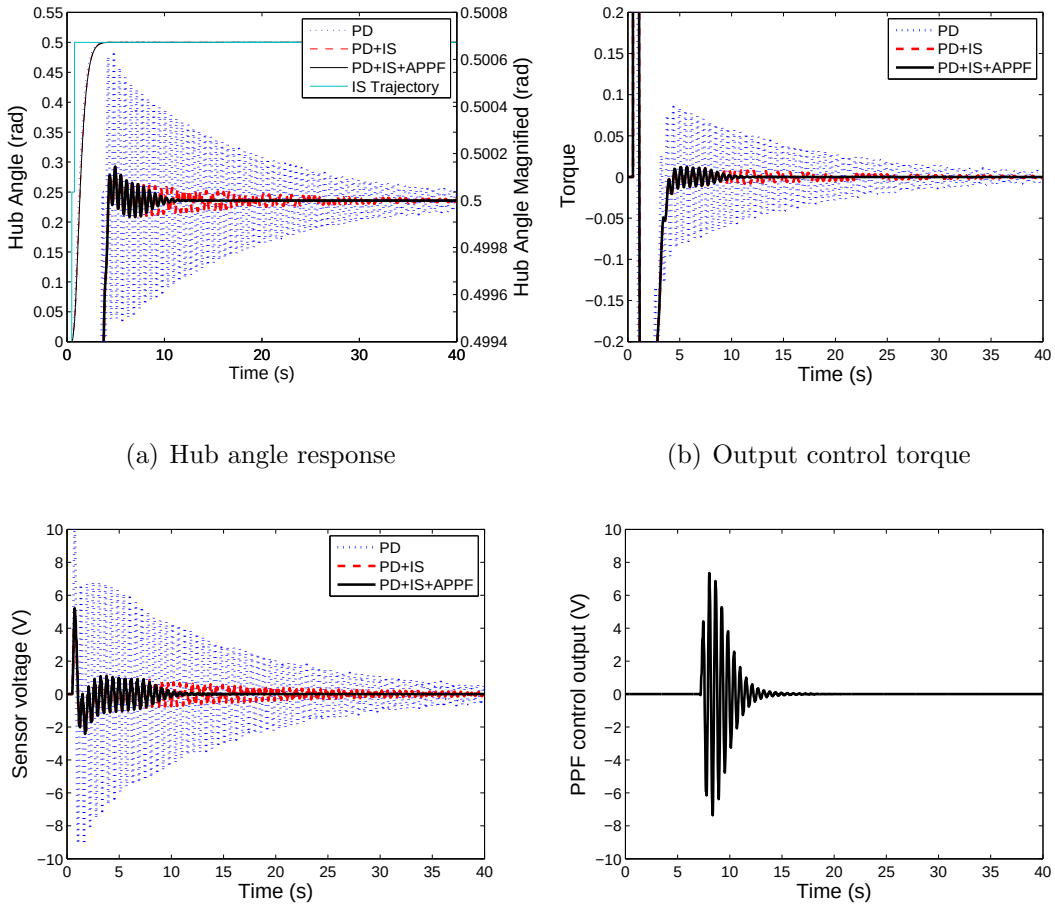

(a) Hub angle response

(b) Output control torque

(c) PZT sensor voltage

(d) Control voltage from PPF

Fig. 3.8 Simulation results with multi-mode adaptive PPF and ZV input shaper (frequency uncertainty: +10%)

damped out the residual vibrations of the manipulator in about 11 seconds.

In the next case, when the ZV shaper is replaced with a ZVD shaper, it is expected that the residual vibration will be lower for both cases. In Fig. 3.9 when the frequency error is +50%, it can again be seen that there will be residual vibration

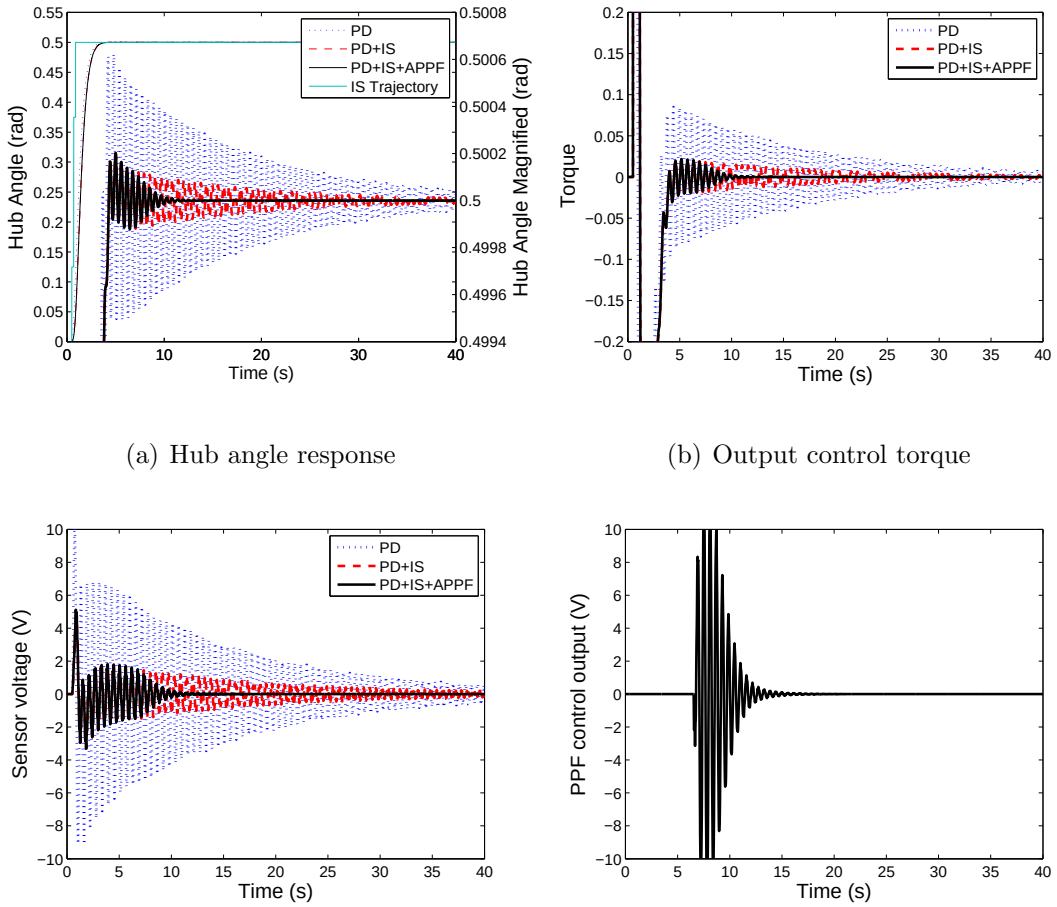

(a) Hub angle response

(b) Output control torque

(c) PZT sensor voltage

(d) Control voltage from PPF

Fig. 3.9 Simulation results using multi-mode adaptive PPF and ZVD input shaper (frequency uncertainty: +50%)

for the ZVD shaper control only at the end of the simulation, while again, with the combined law, it is damped out within 12 seconds. In Fig. 3.10 when the frequency error is +10%, the effect of the input shaper becomes much stronger, and there is only a small amount of residual vibration. Here again, however, in roughly 11

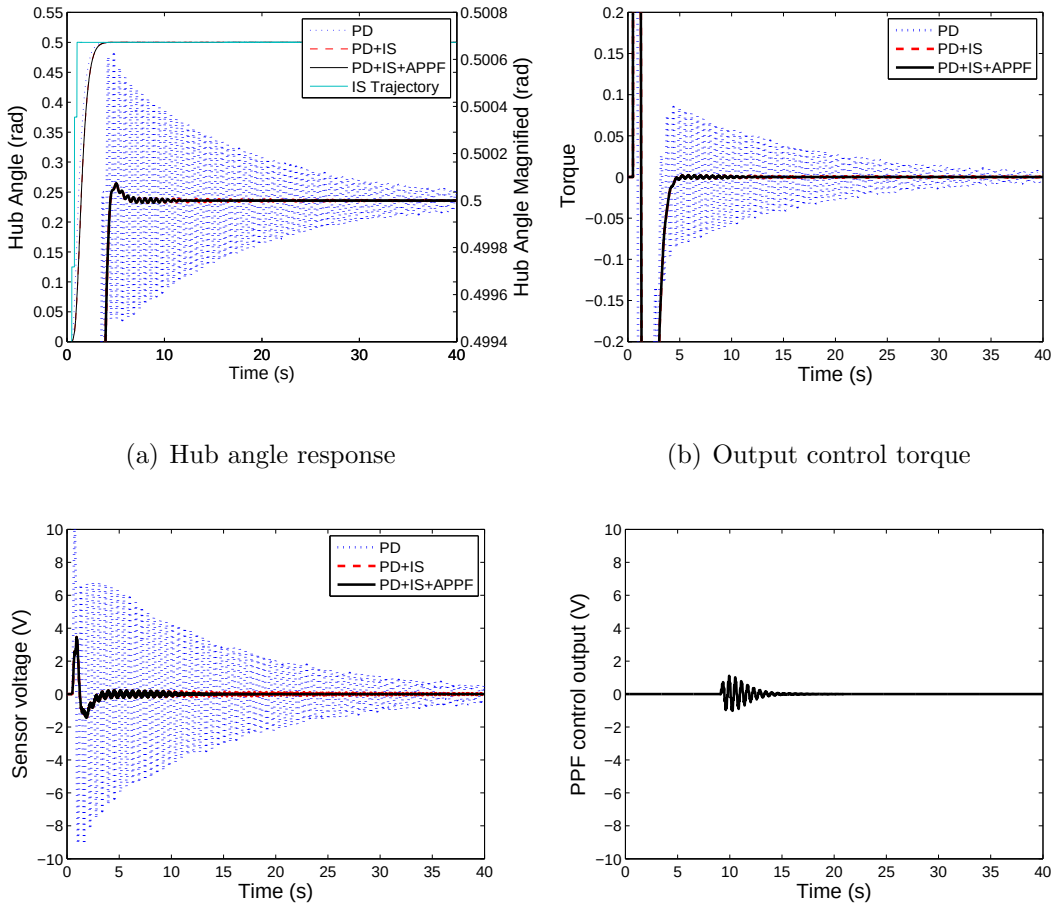

(a) Hub angle response

(b) Output control torque

(c) PZT sensor voltage

(d) Control voltage from PPF

Fig. 3.10 Simulation results using multi-mode adaptive PPF and ZVD input shaper (frequency uncertainty: +10%)

seconds, the combined law has suppressed the vibrations of the manipulator.

For the last shaper considered, the ZVDD, it is again expected that the amount of residual vibration will be smaller than that of the ZVD and ZV shaper due to the fact that it is more robust. For a frequency error of +50% in the shaper, it can

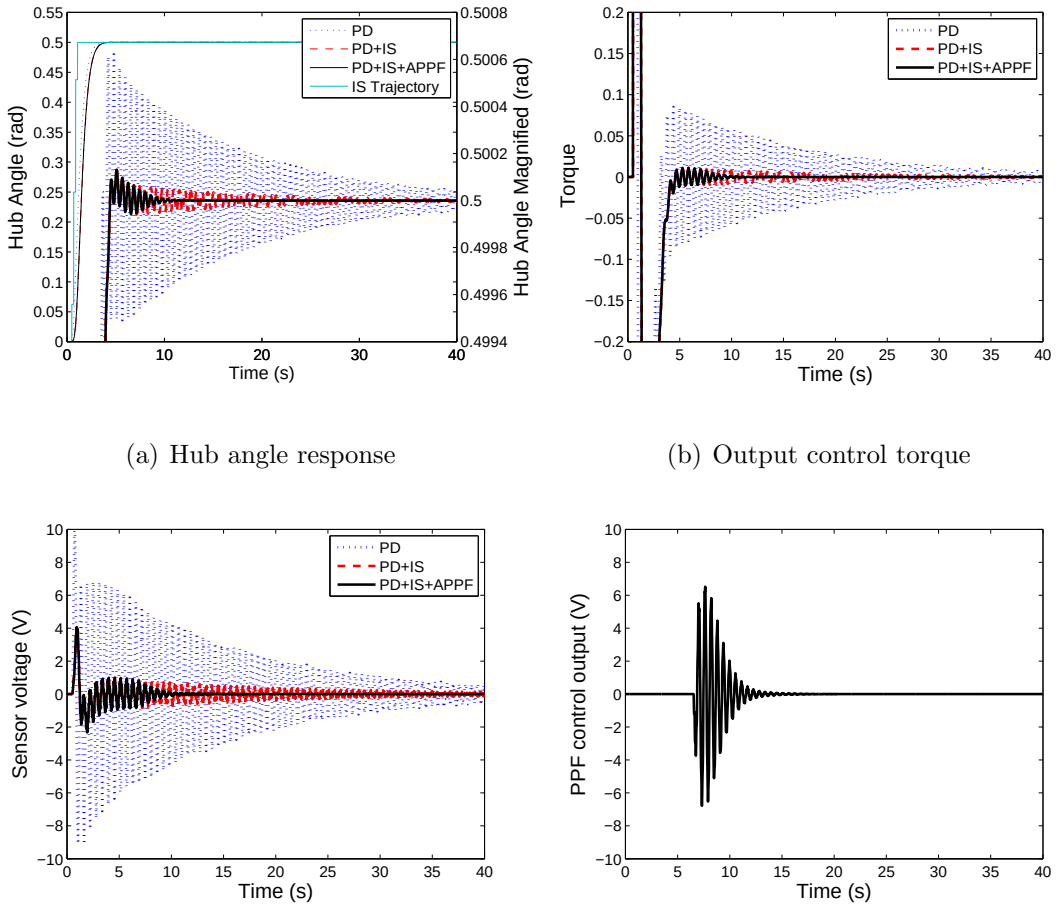

(a) Hub angle response

(b) Output control torque

(c) PZT sensor voltage

(d) Control voltage from PPF

Fig. 3.11 Simulation results using multi-mode adaptive PPF and ZVDD input shaper (frequency uncertainty: +50%)

be seen in Fig. 3.11 that with the ZVDD shaper, there is still residual vibration again at the end of the simulation, again however, at a lower level than that of the ZVD shaper. When the ZVDD shaper is combined with the adaptive PPF law, the vibrations again have been removed in roughly 11 seconds. For the next case,

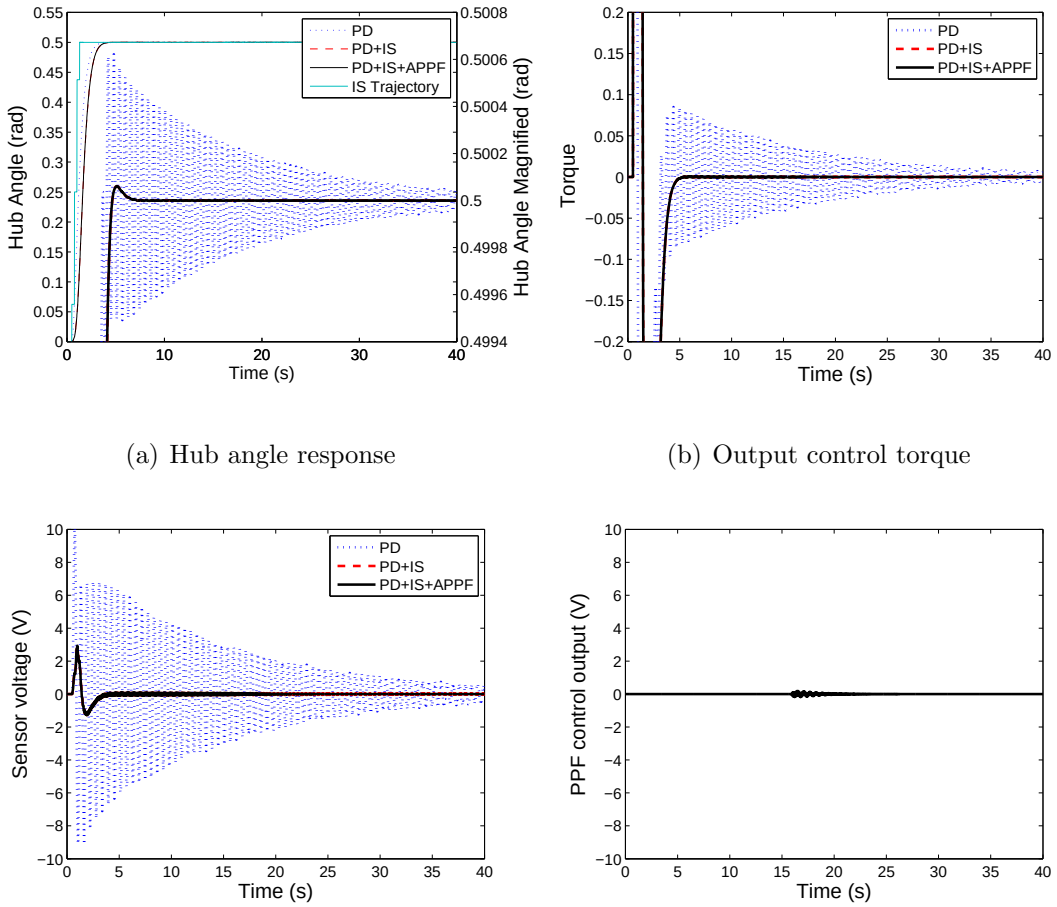

(a) Hub angle response

(b) Output control torque

(c) PZT sensor voltage

(d) Control voltage from PPF

Fig. 3.12 Simulation results with multi-mode adaptive PPF and ZVDD input shaper (frequency uncertainty: +10%)

when the error is +10% (in Fig. 3.12), the residual vibration is very, very small for the ZVDD shaper, and it could be argued that in experiment, this would be very difficult to pick up out of noise. The combined law again suppresses what little residual vibration there is left in the system.

The simulation results indicate that the proposed adaptation law works and can adapt to the actual parameter values. Moreover, the results show that better vibration suppression performance can be obtained by combining input shaping with the proposed multi-mode adaptive PPF controller. When the design frequency of an input shaper is close to the true value, the first vibration mode is more effectively suppressed and the second mode is not as excited by the slewing motion. As the initial value chosen for the first natural frequency of the system becomes less accurate, the vibration suppression capability of the input shaper obviously decreases and more vibrations are seen in the system, and here the multi-mode adaptive PPF algorithm shows its benefits. Also, as expected, as the robustness of an input shaper increases, the amount of system vibration decreases, even when the shapers are badly tuned.

3.3.6 Experimental Results

In this section, two sets of experiments will be conducted. The first is termed the constrained case as the motor is disabled, hence the vibration will be externally induced in the system. The second set of experiments is termed the unconstrained case as the manipulator will be slewed by the motor. Due to issues with the motor and gearbox, including a large deadzone on the command, only the ZV shaper will be used for the unconstrained experiments.

It was also found through experiments that the system possessed quite a large feedthrough (or direct energy transmission) term. In the following section, conditions for the stability of PPF are derived for systems with feedthrough.

3.3.6.1 Modification to the PPF Control Structure for Systems with Feedthrough

To prove the stability of PPF in the presence of feedthrough, the structural equations can be rewritten in matrix form as

$$\ddot{x} + 2Z_s\Omega_s\dot{x} + \Omega_s^2 x = K^T u \tag{3.81}$$

$$y = Kx + Du \tag{3.82}$$

where $x = [x_1, x_2, ..., x_n]^T$, $Z_s = diag\{[\zeta_1, \zeta_2, ..., \zeta_n]\}$, $\Omega_s = diag\{[\omega_1, \omega_2, ..., \omega_n]\}$, and $K = [\sqrt{k_1}, \sqrt{k_2}, ..., \sqrt{k_n}]$. The controller equation can now be written as

$$\ddot{\eta} + 2Z_f\Omega_f\dot{\eta} + \Omega_f^2\eta = \Omega_f G^T y \tag{3.83}$$

$$u = G\Omega_f\eta \tag{3.84}$$

where $\eta = [\eta_1, \eta_2, ..., \eta_m]^T$, $Z_f = diag\{[\zeta_{f_1}, \zeta_{f_2}, ..., \zeta_{f_m}]\}$, $\Omega_f = diag\{[\omega_{f_1}, \omega_{f_2}, ..., \omega_{f_m}]\}$, and $G = [\sqrt{g_1}, \sqrt{g_2}, ..., \sqrt{g_m}]$. The notation $z_i = 2\zeta_i\omega_i$ and $z_{f_i} = 2\zeta_{f_i}\omega_{f_i}$ may also be used interchangeably. By combining equations to form the closed loop system [72]

$$\begin{bmatrix} \ddot{x} \\ \ddot{\eta} \end{bmatrix} + \begin{bmatrix} 2Z_s\Omega_s & 0 \\ 0 & 2Z_f\Omega_f \end{bmatrix} \begin{bmatrix} \dot{x} \\ \dot{\eta} \end{bmatrix} + \begin{bmatrix} \Omega_s^2 & -K^T G\Omega_f \\ -\Omega_f G^T K & \Omega_f^2 - \Omega_f G^T D G\Omega_f \end{bmatrix} \begin{bmatrix} x \\ \eta \end{bmatrix} = \begin{bmatrix} 0 \\ 0 \end{bmatrix} \tag{3.85}$$

which can then be written compactly as

$$\ddot{\hat{x}} + \hat{Z}\dot{\hat{x}} + \hat{\Omega}\hat{x} = 0 \tag{3.86}$$

Since $\hat{Z} > 0$, it must only be shown that $\hat{\Omega}$ is also positive definite. By taking the Schur complement of the closed loop stiffness matrix, $\hat{\Omega}$, the two conditions that guarantee stability of PPF for a system with feedthrough are found as [107]

$$C_1 = \Omega_f^2 - \Omega_f G^T D G \Omega_f > 0 \tag{3.87}$$

and

$$C_2 = \Omega_s^2 - K^T G \Omega_f C_1^{-1} \Omega_f G^T K > 0 \tag{3.88}$$

3.3.6.2 Constrained Experiments

From the FFT of the open loop response, the actual natural frequencies of the system can be found as 10.0091 rad/s and 60.4882 rad/s respectively, although they are assumed unknown. To excite vibrations in a repeatable manner, the piezoelectric actuator is used to excite vibration using the addition of two sinusoidal signals at the beam's first two natural frequencies along with a noise component for 10 seconds (not shown in the plots). The actuator is then switched off at which point the estimation and control can begin. The three parameters for the estimation algorithm are chosen to be: $\beta = 5$, $Q_0 = 10^9 I$, and the initial paramter estimate is taken as a vector of ones implying no prior knowledge of the system. During the

control run, the estimator finds the first two natural frequencies to be 10.0246 rad/s and 60.0935 rad/s respectively, which are very close to the true values. It takes the estimator approximately three seconds to converge on the correct frequency values as can be seen in Figs. 3.15 and 3.16.

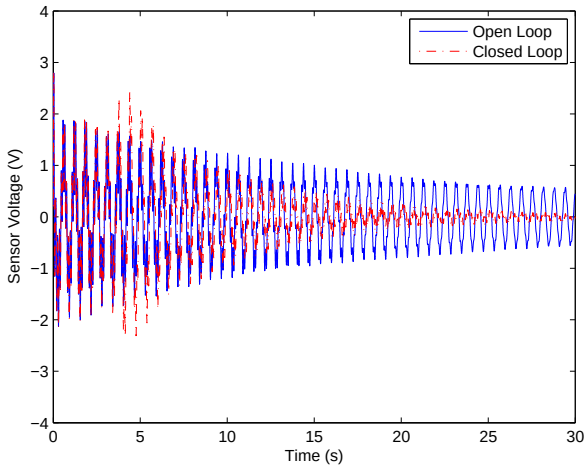

Fig. 3.13 Piezoelectric sensor voltage due to vibration

The PPF control takes approximately 25 seconds to damp out the vibrations as can be seen in Fig. 3.13, with the corresponding control voltage seen in Fig. 3.14. This is relatively quick due to the beam's extremely small intrinsic damping and given that free vibration would continue in time into the minute range. One important effect should be discussed in Fig. 3.13. When the control comes online at approximately 3 seconds it can be seen that the voltage detected by the piezoelectric sensor rises before being damped out by the PPF control. This is due to the effect

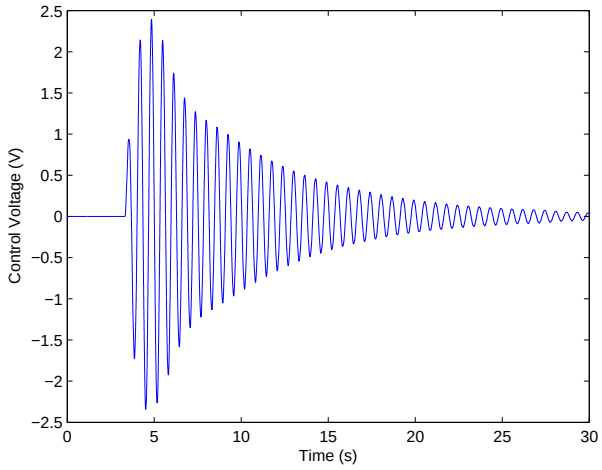

Fig. 3.14 Voltage supplied by control to amplifier

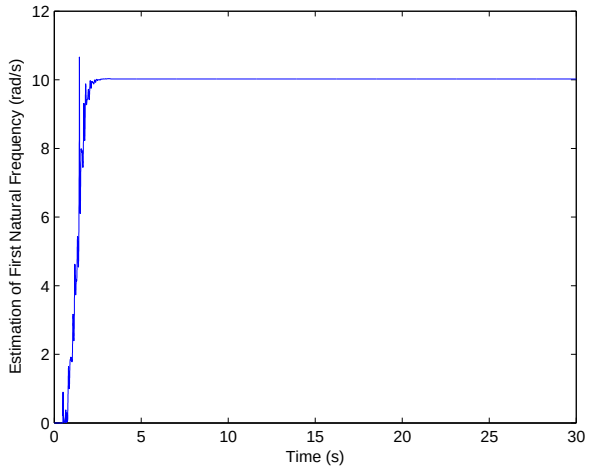

Fig. 3.15 Estimation of the first natural frequency in rad/s

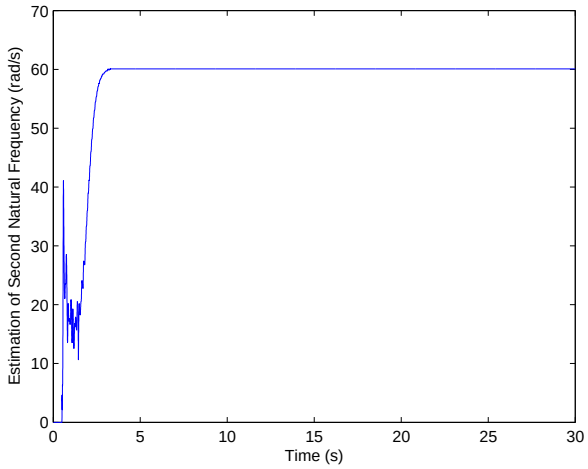

Fig. 3.16 Estimation of the second natural frequency in rad/s

of feedthrough, which collocated piezoelectric sensor/actuator pairs are particularly susceptible to [23]. From a mathematical point of view, for the first three seconds, when the control is off, the tranfer function is simply that of a monic vibrating system subjected to an arbitrary impulse. When the control comes on, the transfer function that describes the input-output relationship between the sensor and actuator takes over, however, its denominator remains the same, while its numerator will be altered [116, 117]. Physically, this is due to the fact that for the collocated pair there will be some direct energy transmission from the actuator to the sensor. Thus the sensor voltage is made up of two components, that of the beam response due to the actuator, and some direct transmission of the strain energy due to the collocation of the actuator [117].

3.3.6.3 Unconstrained Results

To experimentally test the effectiveness of combining input shaping and adaptive PPF, the simplest input shaper, the ZV shaper is chosen. Also, the motor is fairly powerful and has a large amount of static friction, thus a direct comparison of different shapers is unfeasible due to saturation of the vibration signal on the measurement electronics, even with the 4:1 voltage divider on the input. A bang-bang torque command is set up as 0.5 V for 1.115 seconds which is convolved with the ZV shaper. The estimator is on at the beginning with arbitrary initial guesses, and is set up to adapt on $G_{21}(s)$. Since the coefficients of the transfer function denominator are being estimated, the individual modal frequencies are retrieved from these parameters via a numerical root-finding method at each time step. The estimator is modified to turn off when

$$\frac{1}{\gamma + \int_0^t \sqrt{|\epsilon(\tau)|} d\tau} < \delta \tag{3.89}$$

where δ is the threshold for convergence to have occurred, and γ is a small positive bias term such that the division remains defined. This is done since at this point the parameter estimates will have converged within a reasonable amount, as ϵ represents the difference between the actual transfer function and estimated transfer function, and adaptation is no longer needed. The second reason this is done, is that after a few seconds of running, the PPF controller may start to eliminate the vibrations

in the structure and the persistence of excitation condition may no longer be valid, leading to possibly erroneous estimates of the natural frequencies as control is applied. The estimator parameters are chosen as λ=64, β=3, $\hat{\Phi}_0 = [1,1,1,1]^T$, Q_0=$10^{11}I$, R_0=10^{16}, δ=1, and γ=0.1. The control parameters for PPF are chosen to be g_1=0.25, g_2=0.015, ζ_1=0.25, and ζ_2=0.015.

In Fig. 3.17 the results with the ZV shaper tuned to $1.5\omega_1$ can be seen. The result for the ZV shaper shows that vibration is still present at 60 seconds. With the adaptive control law, the vibrations are suppressed to a low level much faster than with only the input shaper. The estimator produces the first two frequencies of the system as 1.6011 and 9.8915 Hz in roughly 4.3 seconds. In Fig. 3.18 the results for the ZV shaper tuned to $1.1\omega_1$ are presented. While the vibration level is lower than that for the ZV shaper at $1.5\omega_1$ there is still a large amount of residual vibration in the system. The estimator produces the system frequencies in this case as 1.5931 and 9.8390 Hz in roughly 4.6 seconds. In both cases the final motor position is achieved within 1.5 seconds and the position error is limited to within 3% of the maneuver, which is acceptable given the large amount of friction present in the system. The use of the shapers is advantageous in the fact that the residual vibrations after the maneuver are smaller than they would be for the bang-bang input. This also allows the APPF controller to suppress the vibrations faster. In both cases the estimator identifies the frequencies quickly and the PPF control law

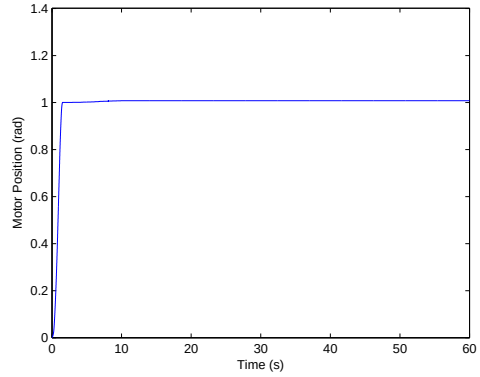

(a) Hub angle response

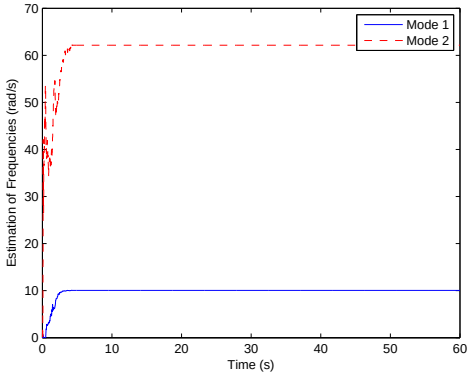

(b) Estimation of the system frequencies

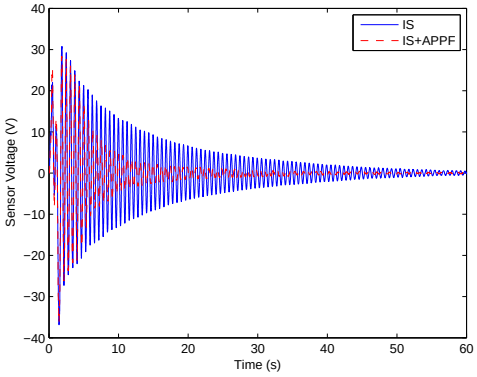

(c) PZT sensor voltage

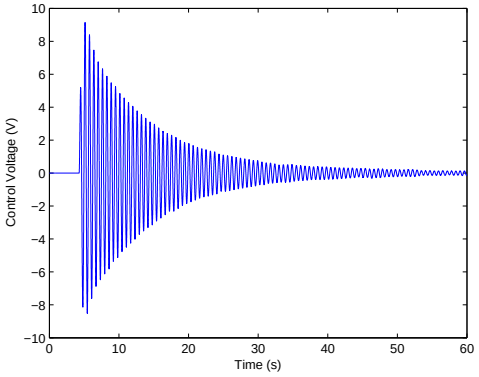

(d) Control voltage from PPF

Fig. 3.17 Experimental results with multi-mode adaptive PPF and ZV input shaper (tuned to $1.5\omega_1$)

comes online to more effectively suppress the system vibration.

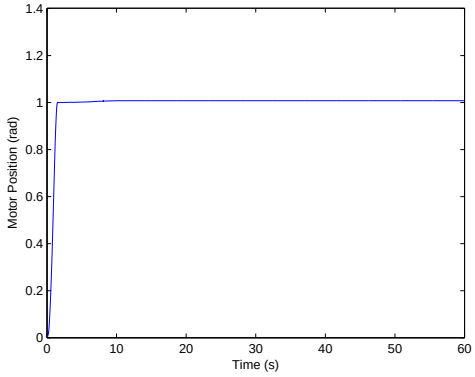

(a) Hub angle response

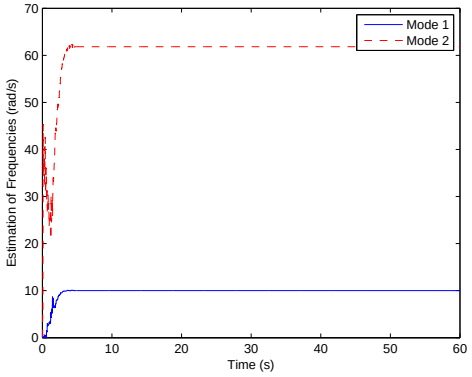

(b) Estimation of the system frequencies

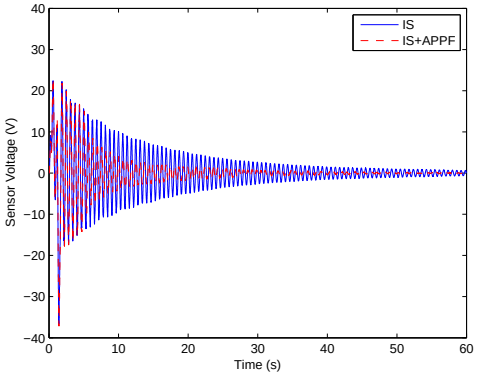

(c) PZT sensor voltage

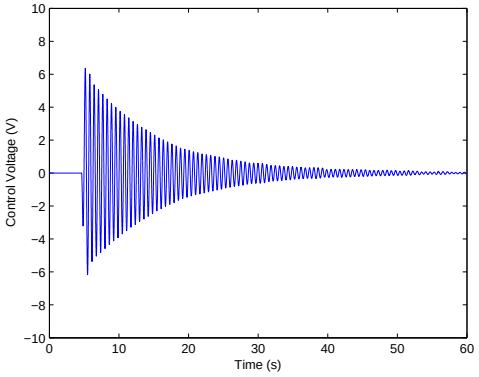

(d) Control voltage from PPF

Fig. 3.18 Experimental results with multi-mode adaptive PPF and ZV input shaper (tuned to $1.1\omega_1$)

3.4 Genetic Algorithm for System Identification and Controller Optimization

Most conventional optimization methods are based upon calculus and require a good initial guess of the parameter as well as derivatives of the objective function. Conventional methods can fall into local minima, rather than the the global minimum, as they are point-to-point search techniques. Genetic algorithms on the other hand are stochastic algorithms capable of searching the entire solution space with more likelihood of finding the global optimum when the system is either hard to characterize, nonlinear, or little is known about it ahead of time. Genetic algorithms are based on Darwin's 'survival of the fittest' principle of evolution and consist of a population of individuals that each represent a possible solution to the optimization problem. This population of possible solutions is then used to create a new population by evolutionary means such as selection, crossover, and mutation. By searching in parallel, the algorithm is much less likely to fall into local minima, and more likely to find the global minima. Moreover, GAs were also shown to have no issues in dealing with measurement noise as the error was typically around the noise level [103]. However, GAs are typically much more computationally intensive to run than conventional optimization methods, and thus take longer to produce a solution.

A genetic algorithm works as follows: first, a population is initialized randomly where each individual in the population represents a possible solution to the optimization problem. A string of symbols makes up each individual and can be encoded in a variety of ways (binary, real, etc.). In this case, binary encoding is chosen, however, Gray coding is used to avoid Hamming cliffs. Each individual in the population is evaluated by an objective function, and it is the genetic algorithms goal to optimize this objective function. Clearly, the objective function will depend on the specific problem to be optimized. Based on how well each individual in the population minimizes (or maximizes) the objective function, they will be assigned a rank. Here the fitness function is based on rank and can be defined as

$$Fitn = 2 - SP + 2(SP - 1)\frac{P - 1}{N - 1} \tag{3.90}$$

where N is the number of individuals, P is their rank, and SP is the selective pressure. A linear ranking allows values of SP between 1 and 2, and 2 is used in this case to give a proportionately larger weight to better individuals. A new population will be created by merging two individuals from the current generation (crossover operator) or by randomly modifying an individual (mutation operator). A new generation will be formed by keeping the parents and children (selection operator) with the highest fitness values and rejecting those with poor ones, ensuring the population stays the same size. Due to these operations, the best individual (or solution) should begin to emerge over successive generations.

3.4.1 Modifications to Simulation Model

Placing the structure in transfer function form gives

$$G_{plant}(s) = \sum_{i=1}^{\infty} \frac{k_i}{s^2 + 2\zeta_i\omega_i s + \omega_i^2} \tag{3.91}$$

where k_i is the gain, ζ_i is the damping, ω_i is the frequency, and i is the mode number. In practice, only a certain bandwidth is of interest and a modal truncation is usually performed to keep only those modes belonging to the frequency range of interest. However, straight modal truncation can cause problems for collocated systems as the effect of the poles and zeros from the higher modes will be ignored. While the poles of the truncated system will lie at the correct frequencies, the locations of the zeros will be distorted due to the omission of the higher order modes [116]. This can cause a large difference between the theoretically predicted closed loop performance and the actual performance, and in the worst case possibly lead to instability due to overestimation of the maximum allowable controller gain. A feedthrough term can be added to the transfer function to compensate for this effect as

$$G_{plant}(s) = \sum_{i=1}^{n} \frac{k_i}{s^2 + 2\zeta_i\omega_i s + \omega_i^2} + D \tag{3.92}$$

where n is the number of modes kept in the model and the feedthrough term D is given by [116]

$$D = \frac{1}{2\omega_c} \sum_{i=n+1}^{\infty} \frac{k_i}{\omega_i} \ln\left(\frac{\omega_i + \omega_c}{\omega_i - \omega_c}\right) \tag{3.93}$$

where ω_c is an ideal lowpass filter cutoff frequency between mode n and $n+1$.

3.4.2 GA for System Identification

Using a genetic algorithm for system identification should offer the advantages of being able to find an optimal solution without getting stuck in local minima, and also being very robust to measurement noise. Unfortunately, genetic algorithms do poorly at hill-climbing in the general vicinity of the global optimum. This problem becomes even more pronounced for highly resonant systems, such as a vibrating beam due to the importance one paramter, specifically frequency in this case, plays over another. Consider for example, the objective function (which will be discussed below) in Fig. 3.19 that is evaluated over a 1000-point mesh over a defined search space. A small dip in what appears to be a well-behaved solution space is observed, which corresponds to the correct frequency. If the 1000-point mesh is shrunk into a much smaller region it becomes clear that even small variations in frequency or gain can drastically change the objective function values. While the GA finds the frequency region of interest very easily, it does not converge to the exact minimum within this area quickly.

To overcome the problems associated with genetic algorithms and hill-climbing, an iterative solution is proposed. However, before that can be done, the objective function, which in this case is equivalent to the minimal error index, must be defined

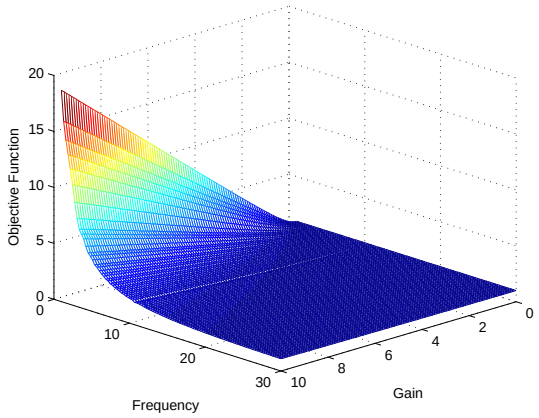

(a) Full search space

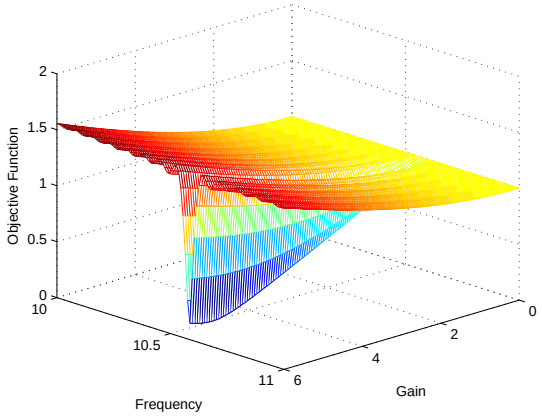

(b) Dense search space

Fig. 3.19 Objective function versus frequency and gain

as

$$ObjF = \sqrt{\frac{\sum_{i=1}^{N}(y_i - \hat{y}_i)^2}{\sum_{i=1}^{N} y_i^2}} \tag{3.94}$$

where y_i is the measured response, and $\hat{y}_i$ is the estimated response. Importantly, $\hat{y}_i$ must be generated for each individual in the population, which in this case precludes

the use of frequency-domain matching due to the huge computational burden this would create.

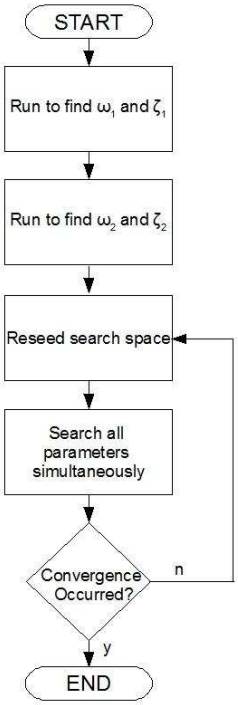

Fig. 3.20 Identification flow chart

The algorithm is shown in Fig. 3.20. In more detail, the first two steps are run separately due to the highly resonant nature of the system. When both frequencies are searched for in one GA run, one can outweigh the other not leading to a small enough region for the next search. Next the standard deviation of each variable at

the end of a run can be calculated from

$$w_{sd} = \sqrt{\frac{\sum_{i=1}^{N} w_i (x_i - \bar{x}_w)^2}{\frac{(N'-1)}{N'} \sum_{i=1}^{N} w_i}} \tag{3.95}$$

where N is the number of individuals, w_i is the weight, x_i is the parameter, $\bar{x}_w$ is the weighted mean, and N' is the number of non-zero weights. Here, the weights w_i become easy to choose as the weight of each individual can be determined by their fitness value. The weighted mean is more likely to lie close to the true solution, while the weighted standard deviation is more likely to determine good bounds. The parameter $\pm r$ can be used to determine how large of a search space around the weighted average is kept. For example, if $r = 1$ the search space is reduced to one standard deviation on each side of the weighted mean, while if $r = 0.5$, half a standard deviation on each side of the weighted mean. One of the main advantages of this implementation is that careful tuning of each of the GA parameters is not required. In many problems a full analysis of what the best parameters are for solving the problem is done on successive GA searches, and then a set of the best parameters is selected for the search.

3.4.3 GA for Optimal PPF

Multiple PPF controllers can be implemented in parallel, one for each mode, tuned to the natural frequency of the mode it is to damp as

$$G_{PPF}(s) = \sum_{i=1}^{m} \frac{g_i \omega_{f_i}^2}{s^2 + 2\zeta_{f_i}\omega_{f_i} s + \omega_{f_i}^2} \tag{3.96}$$

where i is the mode number, m is the number of modes to be controlled, g_i is the controller gain, ζ_{f_i} is the controller damping, and ω_{f_i} is the controller frequency. In [107] the optimization problem for picking the PPF control parameters was suggested as

$$\min_{\omega_{f_i}, \zeta_{f_i}, g_i} ||G_{CL}(iw)|| \tag{3.97}$$

where the H_∞-norm of the closed loop transfer function is to be minimized. However, in [107] the optimization problem was solved by using a nonlinear search, which needed a good initialization scheme, otherwise the optimization problem could fall into local minima.

For this structure, it is desired to control the first two modes of vibration, therefore six parameters need to be picked, three for each PPF controller. It can be time consuming to choose these parameters, and there is no guarantee that they will result in the best possible performance. Since the frequencies are assumed known, the search space is divided in the frequencies to give reasonable bounds on either side of the expected frequency, while the damping term of each controller must

lie between zero and one. The only difficulty lies in choosing the search space for the two PPF controller gains that will result in a closed loop system that can be guaranteed stable. This is an issue due to the fact that the H_∞-norm of an unstable closed loop system can still be well defined, as opposed to the H_2-norm which will become infinite when the closed loop system is unstable. Thus, the search space for the g_i must be bounded according to the stability conditions outlined in Section 3.3.6.1. The H_∞-norm is also a particularly appropriate minimization criteria for vibration control, as it corresponds to the peak gain of the frequency response. Thus, the resonant frequencies will be targeted by this norm. A genetic algorithm naturally lends itself to this nonlinear optimization problem as each candidate in the population can represent one controller, and the resulting closed loop norm can easily be calculated. One note is that carrying out the design for an optimal controller on each mode and combining will yield a suboptimal controller. The result can actually be substantially worse, as the controller for the second mode can seriously degrade the performance on the first mode. Thus, the control design must be done for all modes simultaneously.

3.4.4 Simulation Results

The model parameters chosen for the finite element model of the beam can be seen in Table 3.1. The sensor/actuator pair is chosen to lie near the root of the

beam since the optimal location for the actuator is where the strain energy of the structure is highest [118]. Collocation of the sensor is required by the PPF control law such that the system is minimum phase. The full model is put into transfer function form and the modal parameters of each of the transfer functions found can be seen in Table 3.3.

Table 3.3 System parameters

Parameter	Mode 1	Mode 2	Mode 3	Mode 4
k_i	5.4681	108.9400	322.9974	153.8421
ζ_i	0.0006	0.0033	0.0091	0.0177
ω_i	10.5833	65.5031	181.8815	354.3648
D		0.2159		

3.4.4.1 System Identification

To identify the plant, a chirp signal with an amplitude of 5 V is applied to the control actuator with a frequency that varies from 0.1 to 20 Hz over 30 seconds. The response is recorded and this signal is used to compare the system response against candidate transfer functions in the genetic algorithm. The GA is set up as follows: the number of individuals per subpopulation is selected as 50, with a mutation rate of 0.05, a crossover rate of 0.7, and a generation gap of 0.9, which is somewhat of an elitist strategy as the 5 best individuals will always propagate forward. The number of generations is selected as 50 and the chromosomes have a 20-bit gray-coded binary representation for each variable. In the first two steps

of the algorithm, only the frequency and damping terms are being searched for while in the iterative part of the algorithm, all seven parameters are being searched for simultaneously. For the individual initial searches, the damping and frequency search spaces are selected as

$$\begin{gathered} \zeta_1, \zeta_2 = (0, 1) \\ \omega_{f_1} = (0, 30) \text{ rad/s} \\ \omega_{f_2} = (30, 100) \text{ rad/s} \end{gathered} \tag{3.98}$$

In Fig. 3.21 the minimization history of the first searches for the damping and frequency values for each mode can be seen. The results for the first mode show a larger minimization, this is due to the fact that the first mode is the more dominant signal, thus leading to a better match than for the second mode. The initial search yields values: $\omega_1 = 10.5806$ rad/s, $\omega_2 = 65.5037$ rad/s, and $\zeta_1 = \zeta_2 = 1.0095 \times 10^{-4}$. These values are already very close to their true values, and now with $r = 0.5$ ranges for the full search can be established as

$$\begin{gathered} \zeta_1 = (0, 0.1033] \\ \zeta_2 = (0, 0.1275] \\ \omega_{f_1} = [10.2714, 11.0705] \text{ rad/s} \\ \omega_{f_2} = [65.2217, 66.1367] \text{ rad/s} \\ k_1 = (0, 20] \\ k_2 = [50, 120] \\ D = (0, 1) \end{gathered} \tag{3.99}$$

By reseeding the GA, it offers the advantage of starting fresh with a new search space and being able to populate a specific region more densely, thus leading to better matches. In Fig. 3.22 the minimization history of the first run can be seen where the best individual in the first generation results in an error index of 68% (or

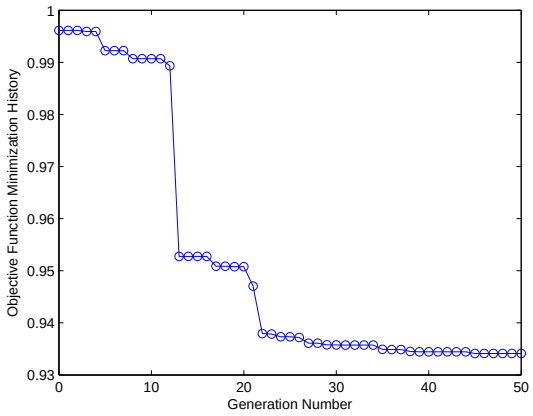

(a) Mode 1

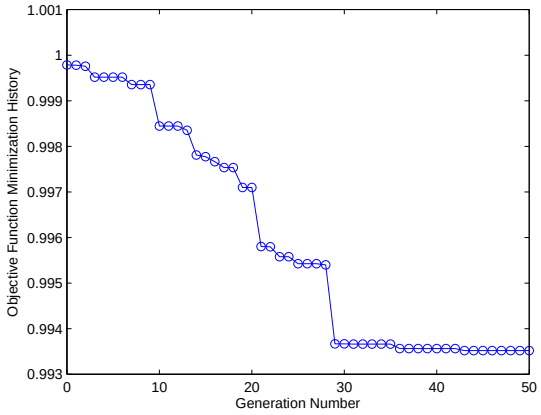

(b) Mode 2

Fig. 3.21 Minimization history of initialization searches

0.68) and by the end, the error has been reduced to about 8.5%. This figure also shows the iteration history of the multiple genetic algorithm runs (where iteration 0 denotes the best individual in the first generation of the first GA run). Clearly, after the third iteration, very little improvement is being made in terms of minimizing the

error index. Thus the genetic algorithm could be stopped here, and the parameters found used as those for the identified transfer function. Where exactly to stop the GA run will depend on a variety of factors such as how good the match needs to be, how much noise there is in the system, and how quickly the parameters converge. Stopping after iteration 3 yields an error of 1.9%. The parameters found are: $k_1 = 5.5403$, $k_2 = 104.3349$, $\zeta_1 = 1.0095 \times 10^{-4}$, $\zeta_2 = 0.0031$, $\omega_1 = 10.5834$ rad/s, $\omega_2 = 65.5036$ rad/s, $D = 0.2291$. It is important to point out that the feedthrough term will be larger in the identified plant than in the actual four mode model due to the fact that it corrects for the neglected modes. Fig. 3.23 shows a comparison of output signals from a chirp input and the transfer functions bode plots. The plant transfer function can clearly be seen to be identified very closely.

Fig. 3.24 shows the comparison of the actual transfer function, to the identified transfer function when subjected to the summation of two sinusoidal signals of 2 V, one at 1 Hz and the other at 5 Hz. It can be seen that the output signals are very close, thus confirming that the system identification has worked properly.

3.4.4.2 Controller Design

The genetic algorithm is set up with the exact same parameters as for the system identification. All six control parameters will be searched for simultaneously, and with respect to guaranteeing stability of the closed loop system, the search space

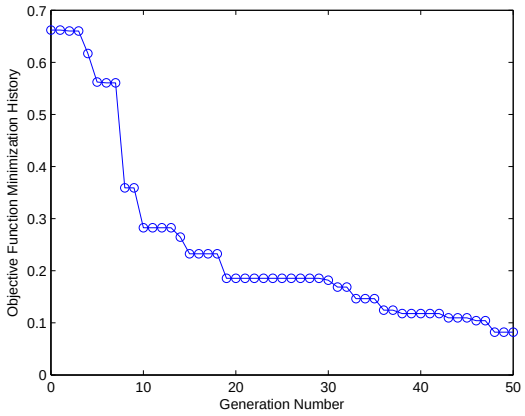

(a) Search history for first full GA run

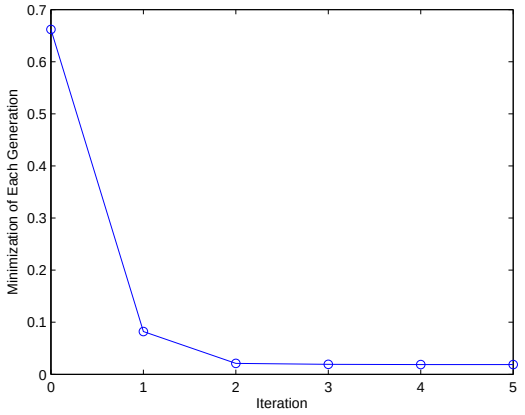

(b) Iteration history of the genetic algorithm

Fig. 3.22 Minimization history

for the genetic algorithm can be defined as

$$\begin{gathered} \zeta_{f_1}, \zeta_{f_2} = (0, 1) \\ \omega_{f_1} = (0, 30) \text{ rad/s} \\ \omega_{f_2} = (30, 100) \text{ rad/s} \\ g_1, g_2 = (0, 1.6) \end{gathered} \tag{3.100}$$

For the GA to run, each individual candidate PPF transfer function is con-

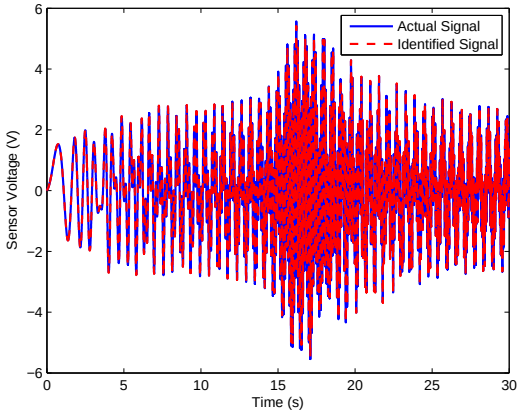

(a) Sensor output due to input chirp signal

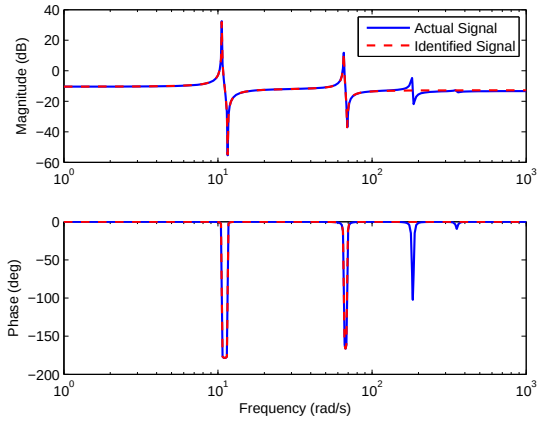

(b) Bode plots

Fig. 3.23 Comparison of identified transfer function to actual transfer function

structed, and then the closed loop H_∞-norm of the system is calculated. In Fig. 3.25 the minimization history of the norm can be seen over all of its generations. Also, in Fig. 3.26, the convergence of the individual PPF controller parameters can be seen in 3D where each of the variables for one controller represents one axis. It can

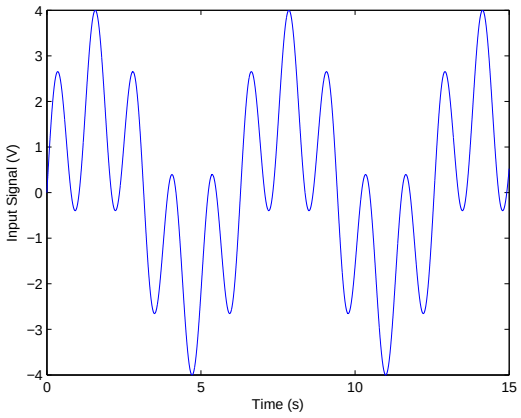

(a) Input Signal

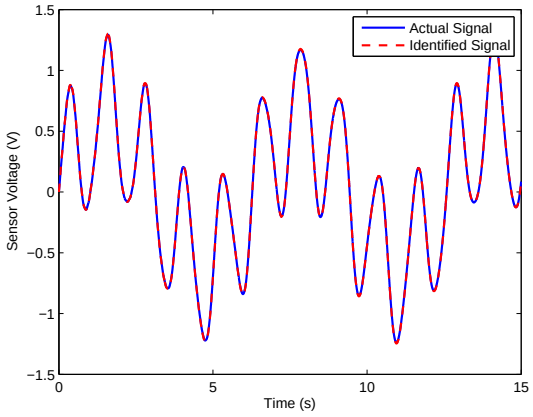

(b) Output Signals

Fig. 3.24 Comparison of identified transfer function response to actual response

be seen that to a large degree the parameters have converged to within a specific region in this space.

At the end of the search, the optimal control parameters are found to be: $g_1 = 0.9212$, $g_2 = 0.3738$, $\zeta_{f_1} = 0.2800$, ζ_{f_2}=0.0698, ω_{f_1}=10.2071 rad/s, and ω_{f_2}=63.3633

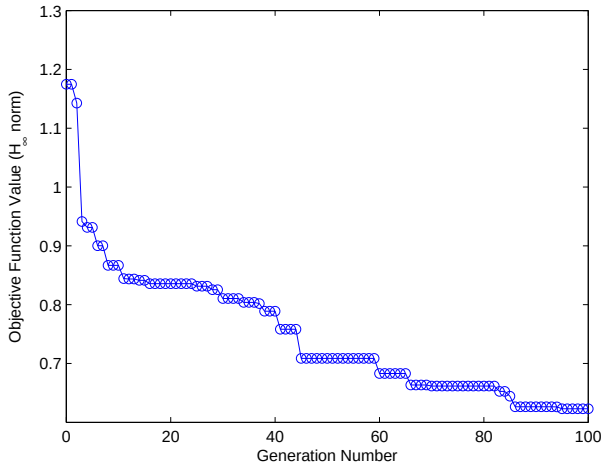

Fig. 3.25 Minimization history of H_∞-norm

rad/s. This results in a reduction of the system's H_∞-norm from 42.3512 to 0.6234, or a reduction from 32.5373 dB to -4.1047 dB. It is good to see that both controller frequencies chosen are near the natural frequencies of the system, which is as expected. It is also interesting to note that they are both slightly smaller than their actual target frequencies at approximately $0.965\omega_i$. This means that for an optimal PPF controller, the frequency should be placed slightly in front of the system natural frequency. Another important point is that the controller gains are well within their stability bounds, thus, even if there is a substantial error in the system identification, the controller should remain stable. In Fig. 3.27 the bode plots for the uncontrolled and controlled system can be seen, where the system response has been significantly attenuated near the resonant frequencies. In addition, it should

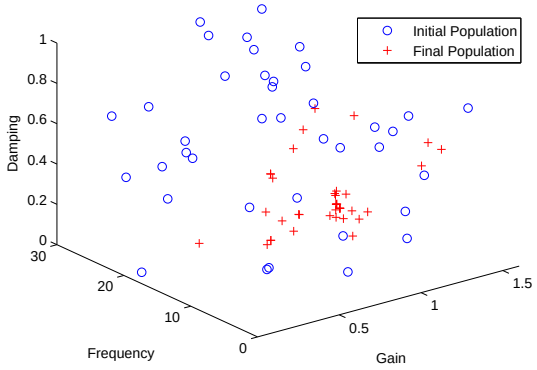

(a) Mode 1

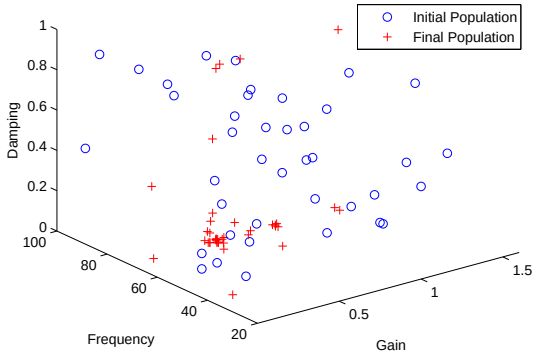

(b) Mode 2

Fig. 3.26 Convergence of individual PPF controller parameters

be noted that it is necessary to minimize the H_∞-norm with both modes of the PPF controller instead of each individual controller for optimal performance. Since the minimization criteria is H_∞, which is minimization of the peak gain, the criteria will not allow spillover from the second controller to reduce the controller effective-

ness on the first mode as this would violate the minimization criteria itself. Hence, it can be seen that the magnitude plot for the closed loop system is very nearly flat across the bandwidth of interest and that the first and second mode peaks are at similar magnitudes. Finally, the designed controller is applied for vibration suppression in Fig. 3.28(a). The plant is subjected to the summation of two 4 V sinusoidal inputs near its first two resonant frequencies for five seconds. After this point, the input signal is switched off and the PPF controllers are turned on and suppress the vibrations in less than 15 seconds. For verification that the control command generated by the designed PPF controller is both reasonable and able to be physically implemented, Fig. 3.28(b) shows the generated control signal.

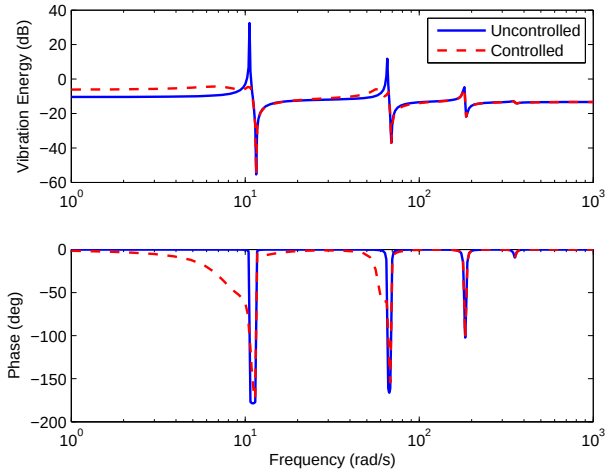

Fig. 3.27 Bode plots of uncontrolled and controlled system

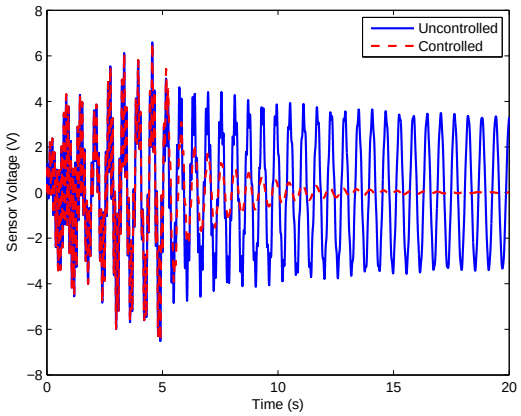

(a) Sensor voltage with and without control

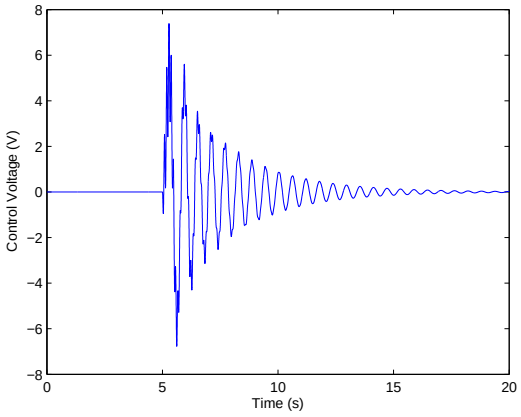

(b) Control voltage

Fig. 3.28 Results of vibration suppression

3.4.5 Experimental Results

Now, the algorithm is verified on the experimental system. For system identification, a chirp signal that varies from 1 to 125 rad/s in 30 seconds with an amplitude of 5 V is applied to the piezoelectric actuator. For the genetic algorithm

to be applied, some bounds must be chosen and some knowledge of the structure from mathematical models is helpful. Where the frequencies lie is roughly known, and given the fact that typical values for structural damping for this type of system are very low, the search ranges can be set up accordingly. The values for the k_i and D_i are harder to define from the models, thus larger ranges are used for them. Thus, the total search space can be set up as

$$\begin{gathered} \zeta_1 = (0, 0.1] \\ \zeta_2 = (0, 0.1] \\ \omega_{f_1} = [1, 25] \text{ rad/s} \\ \omega_{f_2} = [30, 100] \text{ rad/s} \\ k_1 = (0, 20] \\ k_2 = [20, 120] \\ D = (0, 1) \end{gathered} \tag{3.101}$$

In Fig. 3.29 the minimization history of the first iteration can be seen. The best individual from the first iteration gives parameters of: k_1=1.8817, $z_1 = 0.0471$, $\omega_1 = 10.0990$ rad/s, $k_2 = 44.8780$, and $z_2 = 0.2684$, $\omega_2 = 62.6228$ rad/s, and $D = 0.9755$. These values are already fairly close to their true values, and now with $r = 1$ ranges for the next iteration can be established as

$$\begin{gathered} z_1 = [0.0075, 0.0523] \\ z_2 = [0.2073, 0.6001] \\ \omega_{f_1} = [8.9520, 11.2401] \text{ rad/s} \\ \omega_{f_2} = [60.3597, 65.5057] \text{ rad/s} \\ k_1 = [0.6120, 2.5816] \\ k_2 = [28.5363, 65.6717] \\ D = [0.9212, 0.9973) \end{gathered} \tag{3.102}$$

In Fig. 3.29 the minimization history of the first search can be seen where the best individual of the first generation gives an error index of 38% (or 0.38) and by

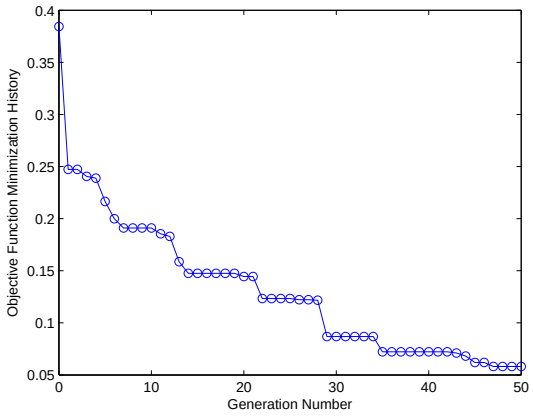

(a) First iteration search history

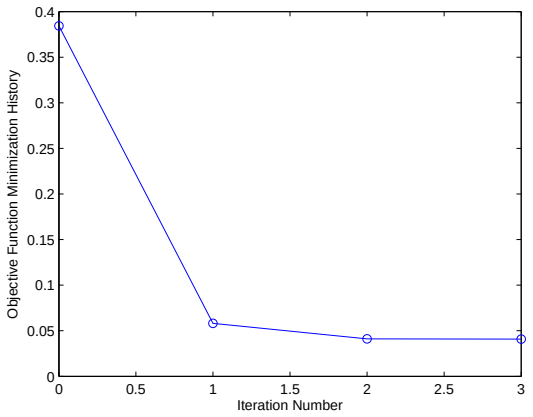

(b) Iteration search history

Fig. 3.29 Minimization history

the end, the error has been reduced to about 6%. In this case since the controller will only be as good as the system identification, thus, it is necessary to have a very good match. The search space is then reseeded into a denser area, and the genetic algorithm is run again. At the end of the third iteration the error is

4.0%, which compared to the simulation results error of 1.9%, is very good. The remaining difference can be largely attributed to the small measurement noise of the system. After the third iteration, very little improvement is being made in terms of minimizing the error index. Thus the genetic algorithm is stopped here, and the parameters found used as those for the identified transfer function. The final parameters are: $k_1 = 2.4249$, $k_2 = 38.4899$, $z_1 = 0.0388$, $z_2 = 0.2343$, $\omega_1 = 10.0842$ rad/s, $\omega_2 = 62.6054$ rad/s, $D = 0.9710$. The feedthrough term here is much larger than that predicted theoretically using the correction for beam theory. However, the beam is very thin and contains collocated piezoelectrics, thus it is suspected that even with the feedthrough correction, the neglection of the membrane strains induced by the piezoelectrics causes this rather substantial difference [23].

Fig. 3.30 shows a comparison of the actual chirp signal to that simulated by the identified transfer function and the agreement is very good. There are some very small differences in the very low frequencies (near 1 rad/s) due to the fact that some remnants of the high pass filtering effects are still present that the lab built signal conditioning circuit cannot completely correct for. A comparison of the experimentally obtained bode plot is also shown against that of the identified plant proving that the identification is accurate in the frequency domain. Finally, Fig. 3.31 shows the comparison of the actual transfer function, to the identified transfer function when subjected to a different input signal, albeit, still sinusoidal.

Given the nature of the beam-piezo system, it is not very practical or meaningful to use another signal type. For this test, the plant is subjected to a summation of two sinusoidal signals of 1 V, one at 1 Hz and the other at 8 Hz.

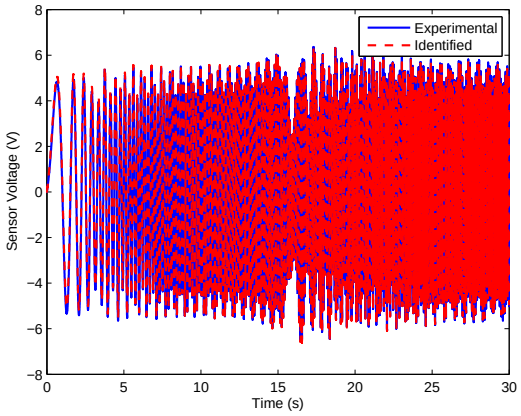

(a) Sensor output due to input chirp signal

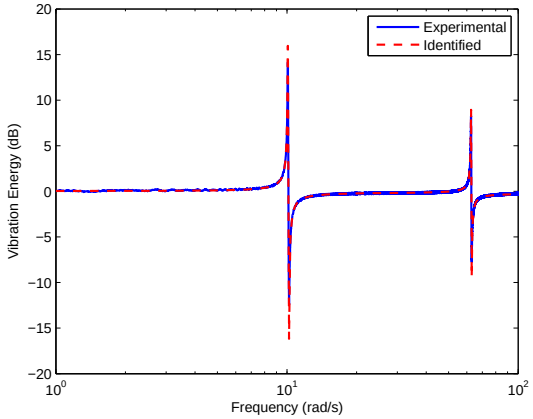

(b) Bode plots

Fig. 3.30 Comparison of identified transfer function to actual transfer function

With respect to guaranteeing stability of the closed loop system for the experi-

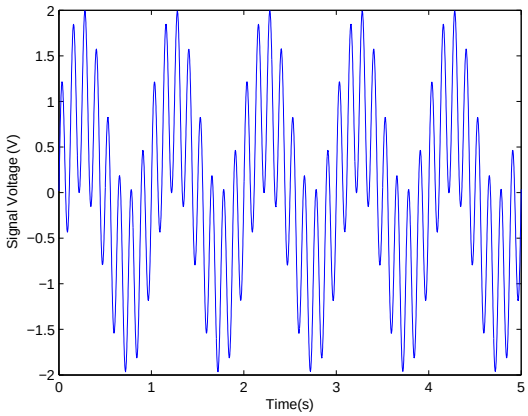

(a) Input Signal

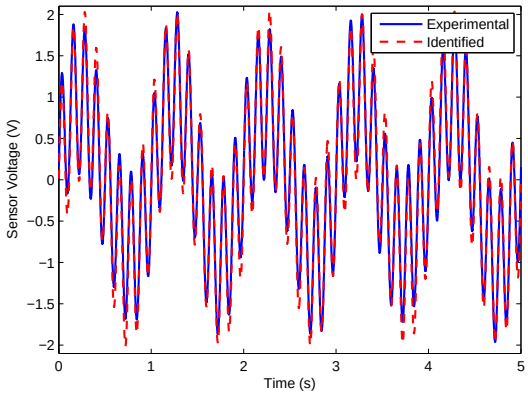

(b) Output Signals

Fig. 3.31 Comparison of identified transfer function response to actual response

ment, the search space for the six control parameters can be defined as

$$\begin{aligned} \zeta_{f_1}, \zeta_{f_2} &= (0, 1) \\ \omega_{f_1} &= (0, 30) \text{ rad/s} \\ \omega_{f_2} &= (30, 100) \text{ rad/s} \\ g_1, g_2 &= (0, 0.4976) \end{aligned} \tag{3.103}$$

Each individual candidate PPF transfer function is then constructed, and then the closed loop H_∞-norm of the system is evaluated. Due to the strong feedthrough,

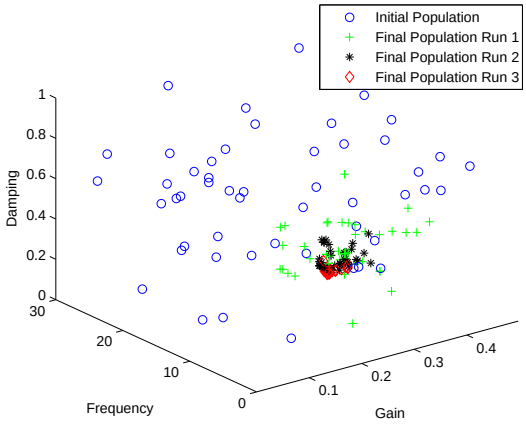

(a) Mode 1

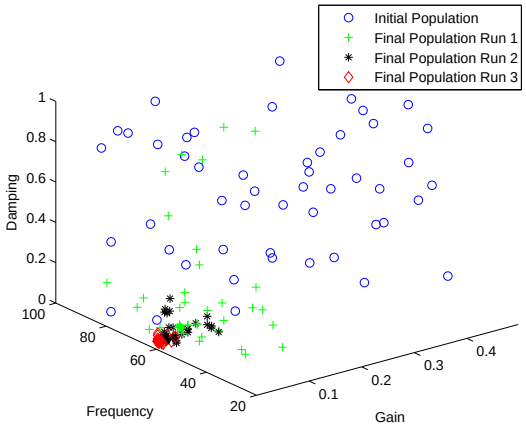

(b) Mode 2

Fig. 3.32 Convergence of individual PPF controller parameters

the iterative implementation used for the system identification will be applied, with the exact same parameters, to refine the choice of control parameters. In Fig. 3.32, the convergence of the individual PPF controller parameters can be seen in 3D over each iteration. It can be seen that after each iteration, the controller parameters

have converged to a smaller region within the parameter space. At the end of the search, the optimal control parameters are found to be: $g_1 = 0.2644$, $g_2 = 0.0136$, $\zeta_{f_1} = 0.2529$, ζ_{f_2}=0.0170, ω_{f_1}=9.9167 rad/s, and ω_{f_2}=62.2707 rad/s. This results in a reduction of the open loop H_∞-norm from 6.3504 to 1.5234, or a reduction from 16.0561 dB to 3.6560 dB as can be seen in Fig. 3.33(a). Fig. 3.33(b) shows the bode plot for the derived controller, where both controller frequencies chosen are near the natural frequencies of the system and slightly smaller than their actual target frequencies, which is as expected from the simulation results. The controller gains also remain well within their stability bounds indicating the closed-loop system should remain stable even if there is a siginificant error in the system identification. Unfortunately, due to the very strong feedthrough, further reduction in the closed loop system norm is unfeasible.

Finally, the designed controllers are applied to the experimental system for vibration suppression in Fig. 3.34(a). The plant is subjected to the summation of two 4.5 V sinusoidal inputs near its first two resonant frequencies for ten seconds (not shown). After this point, the input signal is switched off and the PPF controllers are turned on and suppress the vibrations effectively. Fig. 3.34(b) shows the generated control signal (by the data acquisition card) which is well within the actuation limits of the piezoelectric transducer and amplifier.

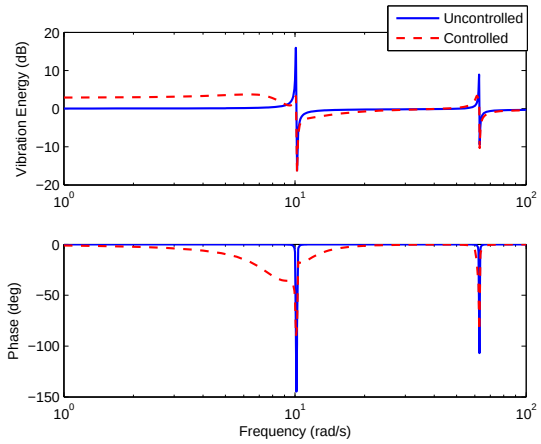

(a) Uncontrolled vs. Controlled

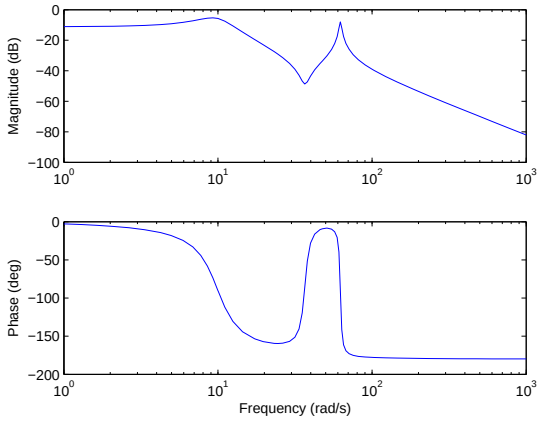

(b) GA designed PPF

Fig. 3.33 Bode plots

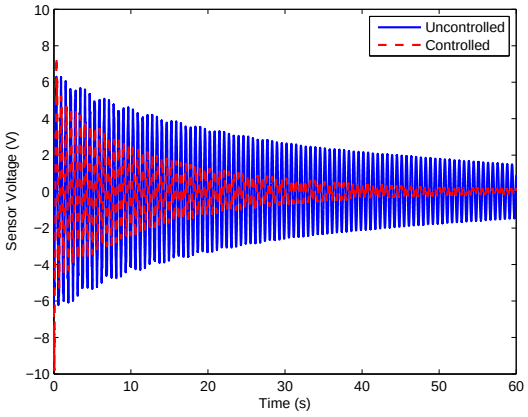

(a) Sensor voltage with and without control

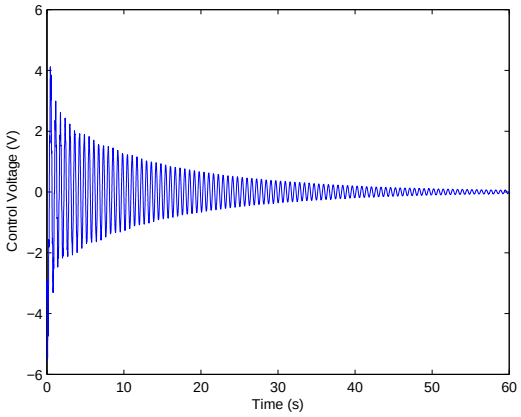

(b) Control voltage

Fig. 3.34 Results of vibration suppression

4 Dynamics and Control of Piezoelectric Actuators for Nanopositioning

Piezoelectric actuators form the basis for many high-precision positioning stages and are finding use in many fields from nanomachining to atomic force microscopy. Piezoelectric actuators operate via the converse piezoelectric effect whereby an applied electric field generates strain in the material. As piezolectric stack-actuators are monolithic in nature, they exhibit no stiction or friction effects, and thus have very precise positioning capabilities, typically only limited by the resolution and noise level of the system electronics. While the total displacement exhibited by the actuator is typically very small, they have a very large bandwidth, and are capable of generating large forces making their application in micro-/nanopositioning stages quite natural.

Piezoelectrics are typically represented by linear models, however, they have two main nonlinearities associated with them, hysteresis and creep. These two effects can lead to a positioning error of as much as 10-15% in the operating range

of a piezoelectric actuator. In general, hysteresis is modeled as a rate-independent nonlinearity that depends upon the current and previous inputs to the actuator. Typically, these nonlinearities are encapsulated through phenomenological modeling and many models have been proposed such as the Preisach, Prandtl-Ishlinskii, Maxwell slip, and Bouc-Wen models among others [119]. The hysteresis effect however, is frequently asymmetrical, and a modified Prandtl-Ishlinskii model that includes saturation operators can be implemented [120]. The creep effect, on the other hand, is characterized by a slow drift in the displacement of a piezoelectric actuator over longer time scales. It is thought to manifest itself through the slow switching of the remnant piezoelectric dipoles in the material that are not aligned with the electric field. There are a few models of creep such as the logarithmic model, fractional order model, and a model that consists of the weighted sum of a finite set of differential equations [121].

For the control of piezoelectrics, a common approach is to try to develop precise models of the hysteresis and creep effects, and then invert them for feedforward control [122, 123]. An interesting method was provided in [124] whereby hysteresis reduction is accomplished through use of a 'phaser', a unitary gain operator that shifts a periodic signal by a phase angle. The problem with the feedforward control method is that it is not robust to disturbances, or changes in the material itself or its operating environment, as the thermal environment of the actuator can substan-

tially change its behaviour. A further drawback of these methods is that a large set of parameters must typically be identified. To overcome these limitations, a variety of feedback controllers have been developed to control the motion of the actuator including sliding mode [125], model reference adaptive control [126], and a back-stepping controller [127]. In [128] ZVD input shapers are combined with PI control to damp the resonance of the actuator and provide tracking control. In [129] the dynamics of the actuator are linearized using high-gain feedback control and then an inverse model of the linear vibrational dynamics is used to formulate a feedforward command. For large bandwidth operation three conventional vibration controllers were compared and then combined with integral control for tracking [130]. For precision positioning of instruments, such as a tunable 2-D Fabry-Perot interferometer, synchronization of multiple actuators is required. Synchronization control has been widely applied to mechanical systems [131]. In [132] a simple yet powerful strategy for synchronization was presented and then augmented to provide adaptive compensation in [133]. For the positioning mechanism of a 2-D Fabry-Perot interferometer, it is desired to synchronize three piezoelectric actuators in parallel to control the movement of the top plate, which sits on a large flexure hinge. For this, in Section 4.3, a state feedback integral plus double integral controller is developed to synchronize three actuators to form the basis of this mechanism.

A problem in the analysis of feedback control for piezoelectric actuators is how

to account for the hysteresis effect in the stability analysis of the system. Compounding this problem is the fact that these actuators all typically require some type of integral control action in order to achieve their desired position, as a constant voltage must be maintained for this to occur, and to counteract the creep effect. The problem with integral control is that the analysis is complicated by the presence of a simple pole at the origin, and hence, represents the critical case for stability. In [134], an analysis similar to that of the circle criterion was developed for a nonautonomous nonlinearity, with a possibly time-varying integral gain, for a class of nonlinearities. In Section 4.4, it is shown that the hysteresis operator belongs to this class of nonlinearities, and then a simplified version of this criterion is developed based on [134] for an LTI system, with an autonomous nonlinearity, and a constant integral gain. Using this criteria, conditions are derived for the maximal regulating gain such that the system is globally asymptotically stable. This analysis is then extended to an integral synchronization controller for multiple piezoelectric actuator systems in Section 4.5. Maximum gains are once again derived for the controller, and then global asymptotic stability of the system is shown through a Lyapunov analysis.

This chapter begins by outlining the experimental system in Section 4.1 and its dynamic model in Section 4.2. In Section 4.3 the integral plus double integral synchronization control strategy is developed. Asymptotic stability of the system is

first investigated for tracking constant reference signals, and then bounded-input-bounded-output (BIBO) stability of the system is discussed for tracking waveforms. Two models of the system are developed, a linear transfer function model, and a nonlinear phenomenological model, for HITL experiments. Next, in Section 4.4, an output feedback integral control law is analyzed for systems with an input nonlinearity. For this, a different dynamic model is formulated that consists of the hysteresis nonlinearity in series with the linear transfer function model. Maximum gains are derived such that the system is globally asymptotically stable, and then experiments are conducted to verify the analysis. Finally, in Section 4.5 an integral synchronization controller is developed for two piezoelectric actuators. The analysis of Section 4.4 is extended to the synchronization controller, and it is shown to be globally asymptotically stable. Then, a HITL model is developed, and experiments are conducted to verify the analysis, and show the effect of different synchronization gains.

4.1 Experimental System

The experimental system consists of a Physik Instrumente P-753.1CD integrated piezoelectric actuator/stage equipped with a capacitive sensor with an accuracy to within 0.05 nm. Power and signal conditioning is supplied by PI's E-625 amplifier/servo-controller unit with a small delay of 100 μs. An xPC real-time tar-

get computer has been configured that can achieve greater than a 100 kHz sample rate for simple A/D and D/A tasks with more advanced controllers able to run at greater than 20 kHz in real-time. The target computer is connected to the piezo system through a National Instruments PCI-6289 card with 16-bit outputs and 18-bit inputs for positioning at the nanometer level. The experimental system can be seen in Fig. 4.1.

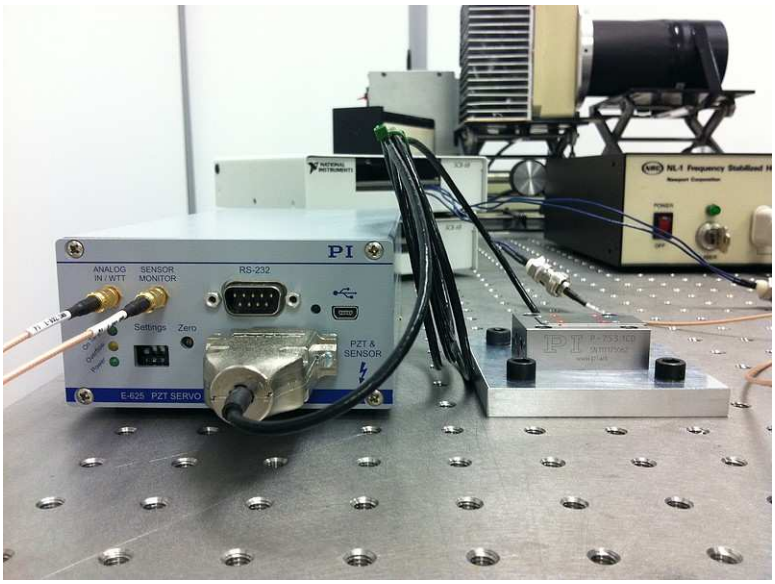

Fig. 4.1 Piezoelectric nanopositioning stage with amplifier

4.2 Dynamic Modeling

The dynamic model of a piezoelectric actuator can be described by a linear transfer function under small signal conditions. For larger signals, a phenomeno-

logical model based on the modified Prandtl-Ishlinskii model of hysteresis can be used. These models can be combined with a creep model, consisting of the sum of a weighted set of first order differential equations, to model the full response of the piezoelectric actuator.

4.2.1 Linear Model

The E-625 amplifier comes with a built-in notch filter that can be used to filter out signals that may excite the nanopositioners first resonant frequency. A linear transfer function model with the notch filter can be identified from a least squares procedure as

$$G(s) = \frac{k\omega^2}{s^2 + 2\zeta\omega s + \omega^2} = \frac{6.8757 \times 10^6}{s^2 + (5.2516 \times 10^3)s + 7.6396 \times 10^6} \tag{4.1}$$

and the frequency response of the model versus the experimental system can be seen in Fig. 4.2(a).

To obtain the full frequency response of the system, the notch filter must be disabled via a jumper in the E-625 unit. The linear model order will rise as the combined frequency response of the piezoelectric and the amplifier must be considered. This is due to the fact that the piezoelectric actuator's first resonant frequency is at approximately 7042 Hz while the amplifiers rolloff is at approximately 1266 Hz. The transfer function of the entire system can then be approximately described by

the transfer function of the piezo in series with the amplifier transfer function as

$$\begin{aligned} G(s) &= \frac{k_f\omega_f^2}{s^2+2\zeta_f\omega_f s+\omega_f^2} \times \frac{k_p\omega_p^2}{s^2+2\zeta_p\omega_p s+\omega_p^2} \\ &= \frac{1.093\times 10^{17}}{s^4+(2.29\times 10^4)s^3+(2.134\times 10^9)s^2+(3.107\times 10^{13})s+1.239\times 10^{17}} \end{aligned} \tag{4.2}$$

This transfer function was found from a least squares procedure and the frequency response of the actuator versus its model can be seen in Fig. 4.2(b).

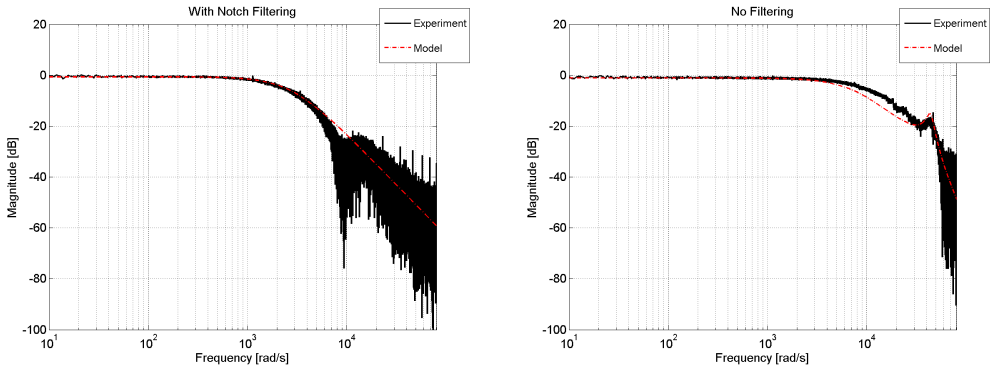

(a) System with notch filter (b) Full system response

Fig. 4.2 Frequency response

4.2.2 Hysteresis Model

The basic block of the Prandtl-Ishlinskii operator can be given as

$$\psi_a(u,w) = \max\{u(t)-a, \min\{u(t)+a, w\}\} \tag{4.3}$$

where $u(t)$ is the control input, and a is the control input threshold value (the magnitude of backlash). The hysteresis operator can be defined recursively as [135]

$$\Psi_a[u](t) = \begin{cases} \psi_a(u(0), \epsilon) \\ \psi_a(u(t), \Psi_a[u](t_i)) \text{ for } t_i < t \leq t_{i+1} \end{cases} \tag{4.4}$$

where $0 = t_0 < t_1 < ... < t_{N-1}$ is a partition of $\mathbb{R}_+$ such that the function u is monotone on each of the subintervals $[t_i, t_{i+1}]$, and ϵ is the initial consistency condition which represents the internal state of the piezoelectric actuator before $u(0)$ is applied at $t = 0$. It is usually, but not necessarily, initialized to zero, representing that the actuator starts from a deenergized state[1].

The generalized operator is given by the weighted summation of a finite number of hysteresis operators as

$$\psi(u(t)) = w_h^T \Psi[u](t) \tag{4.5}$$

where $w_h^T = [\ w_{h_0} \quad w_{h_1} \quad ... \quad w_{h_m}\ ]$ which denotes the slope (or gain) of each individual backlash operator and $\Psi = [\ \Psi_{a_0} \quad \Psi_{a_1} \quad ... \quad \Psi_{a_m}\ ]^T$. Each of the backlash operators will have a threshold width of $2a$ beyond the initial loading curve with $0 = a_0 < a_1 < ... < a_m$. As $a_0 = 0$ it can be seen that the first operator will always be used as it describes the general linear response of the actuator weighted by a factor w_{h_0}. The subsequent operators are only used when the control inputs are greater than their respective threshold values a_i.

[1]Here we have defined the hysteresis operator as $\Psi_a[u]$, where it can possess an initial state. It is more commonly written as in [135], with a non-zero initial condition as $\Psi_a[u, \epsilon]$ to denote its dependence on its initial state.

The standard Prandtl-Ishlinskii operator is symmetric about the center point of its loop, but in experiment it can be observed that the loop is in fact asymmetric. A saturation operator can be combined in series with the hysteresis operator to yield this asymmetric behaviour [120]. The saturation operator can be taken as a weighted linear superposition of linear-stop or one-sided dead zone operators. The dead-zone operator is a nonconvex, asymmetrical, memory-free nonlinear operator [120] that can be given by

$$\Phi_d[\psi](t) = \begin{cases} \max\{\psi(t) - d, 0\} \text{ if } d > 0 \\ \psi(t) \text{ if } d = 0 \end{cases} \tag{4.6}$$

and the full response of the hysteresis becomes

$$\phi(u(t)) = w_s^T \Phi[\psi](t) = w_s^T \Phi[w_h^T \Psi[u]](t) \tag{4.7}$$

where $w_s^T = [\ w_{s_0} \quad w_{s_1} \quad ... \quad w_{s_p}\ ]$ is the weight vector, $d = [\ d_0 \quad d_1 \quad ... \quad d_p\ ]$ where $0 = d_0 < a_n < d_1 < ... < d_p$ is the saturation threshold and $\Phi = [\ \Phi_{d_0} \quad \Phi_{d_1} \quad ... \quad \Phi_{d_p}\ ]^T$. In general, the threshold values for a_i are chosen to be evenly spaced across the input range, however, the threshold values for the saturation operator need not be equally spaced. In fact, the threshold values of the saturation operator are in general not equally spaced, and can be difficult to obtain.

4.2.3 Creep Model

A first order differential equation is used to represent the creep as

$$\frac{1}{\gamma_1}\dot{x}_{c_1}(t) + x_{c_1}(t) = u(t) \tag{4.8}$$

where $u(t)$ is the input. In general, to get a good match, a weighted linear superposition of multiple creep systems is taken as

$$\dot{x}_c = A_c x_c + B_c u \tag{4.9}$$

$$y_c = C x_c \tag{4.10}$$

where $\gamma = [\ \gamma_1 \quad \gamma_2 \quad ... \quad \gamma_q\ ]^T$, $A_c = diag\{\gamma\}$, $B_c = \gamma$ and $C = w_c^T$, where w_c is a weight vector determined by a least squares fit to the experimental data. Here, the γ are typically generated as $\gamma_j = 1/(10^{j-4})$ where $j = 1 \ldots q$.

Eq. 4.8 possesses an explicit integral solution

$$x_{c_1}(t) = e^{-\gamma_1 t} x_{c_1}(0) + \gamma_1 \int_0^t e^{\gamma_1(\tau - t)} u(\tau) d\tau \tag{4.11}$$

where $x_{c_1}(0)$ is the initial condition. If their are implementation issues due to the continuous time representation (with high sample rates being unachievable for the HITL experiments), the discrete time version of the creep operator can be taken with a rectangular approximation to the integral as

$$x_{c_1}(t) = e^{-\gamma_1 T_s} x_{c_1}(t-1) + (1 - e^{-\gamma_1 T_s}) u(t-1) \tag{4.12}$$

Once again, the creep operator may be written as a finite sum of creep operators with weights w_c as

$$y_c(t) = w_c^T x_c \tag{4.13}$$

where the γ are typically generated as $\gamma_j = 1/(10^{j-1}T_s)$ with sample time T_s.

4.3 State Feedback Integral plus Double Integral Synchronization Tracking Control

The linear dynamics of a three piezo parallel system can be described as

$$M\ddot{q} + C\dot{q} + Kq = u(t) \tag{4.14}$$

or written in full as

$$\begin{bmatrix} m_1 & 0 & 0 \\ 0 & m_2 & 0 \\ 0 & 0 & m_3 \end{bmatrix} \begin{bmatrix} \ddot{q}_1 \\ \ddot{q}_2 \\ \ddot{q}_3 \end{bmatrix} + \begin{bmatrix} c_1 & 0 & 0 \\ 0 & c_2 & 0 \\ 0 & 0 & c_3 \end{bmatrix} \begin{bmatrix} \dot{q}_1 \\ \dot{q}_2 \\ \dot{q}_3 \end{bmatrix} + \begin{bmatrix} k_1 & 0 & 0 \\ 0 & k_2 & 0 \\ 0 & 0 & k_3 \end{bmatrix} \begin{bmatrix} q_1 \\ q_2 \\ q_3 \end{bmatrix} = u(t)$$

The control for integral synchronization tracking control can be formulated as

$$u(t) = K_i \int_0^t e^*(\tau)d\tau \tag{4.15}$$

with $e^*(t)$ defined as [132]

$$e^*(t) = e(t) + BT^T T \int_0^t e(\tau)d\tau \tag{4.16}$$

where $e(t)$ is defined as $e(t) = q_d - q$ where q_d is the desired vector. K_i can be

defined as

$$K_i = \begin{bmatrix} k_{i_1} & 0 & 0 \\ 0 & k_{i_2} & 0 \\ 0 & 0 & k_{i_3} \end{bmatrix} \tag{4.17}$$

and the synchronization gain matrix K_s may be defined as

$$K_s = K_i B T^T T \tag{4.18}$$

where $B = diag\{B_1, B_2, B_3\}$ and T is the coupling matrix that is chosen such that $T^T T > 0$ which may be taken for example as

$$T = \begin{bmatrix} 1 & -1 & -1 \\ -1 & 1 & -1 \\ -1 & -1 & 1 \end{bmatrix} \tag{4.19}$$

Hence $u(t)$ may be given by

$$u(t) = K_i \int_0^t e(\tau) d\tau + K_s \int_0^t \int_0^\tau e(\tau_1) d\tau_1 \tag{4.20}$$

which, with T taken as in Eq. 4.19, can be written in full as

$$\begin{aligned} u(t) \;=\; & \begin{bmatrix} k_{i_1} & 0 & 0 \\ 0 & k_{i_2} & 0 \\ 0 & 0 & k_{i_3} \end{bmatrix} \int_0^t \begin{bmatrix} e_1(\tau) \\ e_2(\tau) \\ e_3(\tau) \end{bmatrix} d\tau \\ & + \begin{bmatrix} 3k_{i_1}B_1 & -k_{i_1}B_1 & -k_{i_1}B_1 \\ -k_{i_2}B_2 & 3k_{i_2}B_2 & -k_{i_2}B_2 \\ -k_{i_3}B_3 & -k_{i_3}B_3 & 3k_{i_3}B_3 \end{bmatrix} \int_0^t \int_0^\tau \begin{bmatrix} e_1(\tau_1) \\ e_2(\tau_1) \\ e_3(\tau_1) \end{bmatrix} d\tau_1 \end{aligned} \tag{4.21}$$

4.3.1 Tracking Reference Values

Assuming nominally linear dynamics of the piezoelectric actuator, each system can be represented as

$$\dot{x}_i = A_i x_i + B_i u_i \tag{4.22}$$

with output equation

$$y_i = C_i x_i \tag{4.23}$$

where $x_i = [\ x_{i1} \quad x_{i2}\ ]^T$ and

$$A_i = \begin{bmatrix} 0 & 1 \\ -\omega_i^2 & -2\zeta_i\omega_i \end{bmatrix} \quad B_i = \begin{bmatrix} 0 \\ g_i\omega_i^2 \end{bmatrix} \quad C_i = [\ 1 \quad 0\ ] \tag{4.24}$$

and A_i are assumed to be Hurwitz.

The state equation for each system can be augmented with two integrators as

$$\begin{aligned} \dot{x}_i &= A_i x_i + B_i u_i \\ \dot{\sigma}_i &= e_i \\ \dot{\eta}_i &= \sigma_i \end{aligned} \tag{4.25}$$

where $e_i = C_i x_i - r$ and r is the constant reference, hence $\sigma_i = \int e_i$ and $\eta_i = \int\int e_i$.

This equation can be rewritten in matrix form as

$$\begin{bmatrix} \dot{x}_i \\ \dot{\sigma}_i \\ \dot{\eta}_i \end{bmatrix} = \begin{bmatrix} A_i & 0 & 0 \\ C_i & 0 & 0 \\ 0 & 1 & 0 \end{bmatrix} \begin{bmatrix} x_i \\ \sigma_i \\ \eta_i \end{bmatrix} + \begin{bmatrix} B_i \\ 0 \\ 0 \end{bmatrix} u_i + \begin{bmatrix} 0 \\ -1 \\ 0 \end{bmatrix} r \tag{4.26}$$

or as

$$\dot{z}_i = \hat{A}_i z_i + \hat{B}_i u_i + \hat{E} r \tag{4.27}$$

with output equation $y_i = \hat{C}_i z_i$ with $\hat{C}_i = [\ C_i \quad 0 \quad 0\ ]$.

Clearly, in this case a linear state feedback can be designed as

$$u_i = -K_{x_i} x_i - K_{\sigma_i}\sigma_i - K_{\eta_i}\eta_i = -\hat{K}_i z_i \tag{4.28}$$

where K_{η_i} must be nonsingular.

For the three-piezo system, the state equation can be assembled as

$$\begin{bmatrix} z_1 \\ z_2 \\ z_3 \end{bmatrix} = \begin{bmatrix} \hat{A}_1 & 0 & 0 \\ 0 & \hat{A}_2 & 0 \\ 0 & 0 & \hat{A}_3 \end{bmatrix} \begin{bmatrix} z_1 \\ z_2 \\ z_3 \end{bmatrix} + \begin{bmatrix} \hat{B}_1 & 0 & 0 \\ 0 & \hat{B}_2 & 0 \\ 0 & 0 & \hat{B}_3 \end{bmatrix} u + \begin{bmatrix} \hat{E} & 0 & 0 \\ 0 & \hat{E} & 0 \\ 0 & 0 & \hat{E} \end{bmatrix} r \quad (4.29)$$

or

$$z = \tilde{A}z + \tilde{B}u + \tilde{E}r \quad (4.30)$$

Clearly, the three piezo system is uncoupled with the current state feedback. For the synchronization control, coupling takes place in the feedback gain matrix as

$$\tilde{K} = \begin{bmatrix} K_{x_1} & K_{\sigma_1} & K_{\eta_1} & 0 & 0 & -K_{c_2} & 0 & 0 & -K_{c_3} \\ 0 & 0 & -K_{c_1} & K_{x_2} & K_{\sigma_2} & K_{\eta_2} & 0 & 0 & -K_{c_3} \\ 0 & 0 & -K_{c_1} & 0 & 0 & -K_{c_2} & K_{x_1} & K_{\sigma_1} & K_{\eta_3} \end{bmatrix} \quad (4.31)$$

where K_{c_i} are the cross-coupling terms for the synchronization control as defined by $K_s = K_i B T^T T$.

The equilibrium point of the system will satisfy

$$\begin{aligned} 0 &= A_i x_{i_{ss}} + B_i u_{i_{ss}} \\ 0 &= e_{i_{ss}} = C_i x_{i_{ss}} - r \\ 0 &= \sigma_{i_{ss}} \\ u_{i_{ss}} &= -K_{x_i} x_{i_{ss}} - K_{\eta_i} \eta_{i_{ss}} + K_{c_j} \eta_{j_{ss}} + K_{c_k} \eta_{k_{ss}} \end{aligned} \quad (4.32)$$

where the indices $i \neq j \neq k$ represent the piezo number. By changing coordinates with $\xi = [\ \xi_1 \quad \xi_2 \quad \xi_3\ ]^T$ and ξ_i defined as

$$\xi_i = [z_i - z_{i_{ss}}] = \begin{bmatrix} x_i - x_{i_{ss}} \\ \sigma_i - \sigma_{i_{ss}} \\ \eta_i - \eta_{i_{ss}} \end{bmatrix} \quad (4.33)$$

the closed loop system can be written as

$$\dot{\xi} = (\tilde{A} - \tilde{B}\tilde{K})\xi \quad (4.34)$$

With K_{η_i} nonsingular, $\tilde{K}$ can be designed such that $\tilde{A} - \tilde{B}\tilde{K}$ is Hurwitz [136]. Hence as $t \to \infty$ it can be seen that $C_i x_{i_{ss}} = y_i \to r$, $e \to 0$, $\sigma_i = \int e \to 0$ and $u_{i_{ss}}$ will approach a constant determined by the double integrals of the errors. From Eq. 4.16 it can also be seen that $e^*(t) \to 0$ as $t \to \infty$, hence synchronization of the systems has occurred. This control will ensure asymptotic regulation under all parameter perturbations that do not destroy the stability of the closed-loop system.

4.3.2 Tracking Waveforms: Bounded Input Bounded Output Stability

In this section, the stability of the synchronization controller will be considered for tracking of continuous waveforms. To facilitate this, some variables from the preceding section must be redefined. To start, the state vector z_i remains the same, except that the integral term must be redefined as $\sigma_i = \int x_{i1}$. Hence, Eq. 4.30 is rewritten as

$$z = \tilde{A}z + \tilde{B}u \tag{4.35}$$

where $\tilde{A}$ and $\tilde{B}$ remain defined in the same way as in Eq. 4.29. For the three actuator system, $z \in \mathbb{R}^{3n\times 1}$, $\tilde{A} \in \mathbb{R}^{3n\times 3n}$, $\tilde{B} \in \mathbb{R}^{3n\times 3}$, $u \in \mathbb{R}^{3\times 1}$, where n contains the augmented states for the integral terms. The output equation can be written as $y = \tilde{C}z(t)$ with $\tilde{C} \in \mathbb{R}^{3\times 3n}$, and $y \in \mathbb{R}^{3\times 1}$.

Once again, proceeding with the state feedback approach we have

$$u(t) = \tilde{K}(z_d(t) - z(t)) \tag{4.36}$$

where $\tilde{K} \in \mathbb{R}^{3\times 3n}$ is the same as in Eq. 4.31 and contains the integral, synchronization, and coupling gains. The desired state vector is written as $z_d \in \mathbb{R}^{3n\times 1}$, allowing the state error to be defined as

$$e(t) = z_d(t) - z(t) \tag{4.37}$$

This requires that the desired trajectory in each of the state variables be known which implies that the reference trajectory must be sufficiently smooth for the necessary number of derivatives to exist, and that they are known.

To show BIBO stability, we will change to state error coordinates. Starting from Eq. 4.35 we have

$$\begin{aligned} \dot{z}(t) &= \tilde{A}z(t) + \tilde{B}u(t) \\ &= \tilde{A}(z_d(t) - e(t)) + \tilde{B}\tilde{K}e(t) \\ &= \tilde{A}z_d(t) - \tilde{A}e(t) + \tilde{B}\tilde{K}e(t) \\ &= \tilde{A}z_d(t) - \bar{A}e(t) \end{aligned} \tag{4.38}$$

where $\bar{A} = \tilde{A} - \tilde{B}\tilde{K}$ and $\tilde{K}$ is once again chosen such that $\bar{A}$ is Hurwitz. With $\dot{e}(t) = \dot{z}_d(t) - \dot{z}(t)$, Eq. 4.38 can be rewritten as

$$\dot{e}(t) = \bar{A}e(t) + \dot{z}_d(t) - \tilde{A}z_d(t) \tag{4.39}$$

To prove stability, choose the Lyapunov function

$$V(t) = e^T P e \tag{4.40}$$

where $P = P^T > 0$. Hence the derivative of the Lyapunov function will be

$$\begin{aligned} \dot{V}(t) &= \dot{e}^T P e + e^T P \dot{e} \\ &= (\bar{A}e + \dot{z}_d - \tilde{A}z_d)^T P e + e^T P(\bar{A}e + \dot{z}_d - \tilde{A}z_d) \\ &= e^T(\bar{A}^T P + P\bar{A})e + 2e^T P(\dot{z}_d - \tilde{A}z_d) \end{aligned} \tag{4.41}$$

with $\bar{A}^T P + P\bar{A} = -Q$ as the solution of the Lyapunov equation. Defining $\xi(t) = \dot{z}_d - \tilde{A} z_d$ as the difference between the derivative of the desired state vector and that of the unforced system, we have

$$\begin{aligned} \dot{V}(t) &= -e^T Q e + 2e^T P \xi \\ &= -e^T Q e + 2\xi^T P e \end{aligned} \tag{4.42}$$

To prove bounded-input-bounded-output stability of Eq. (4.42) consider the LTI, strictly proper system given in Eqs. (4.35), where $\tilde{K}$ is chosen to stabilize the system. Choosing the reference trajectory (hence $z_d(t)$ and $\dot{z}_d(t)$) such that $\xi(t)$ is bounded such that $||\xi(t)|| < \bar{\xi}$. Next, consider first that the term $-e^T Q e$ in Eq. (4.42) is both strictly negative and quadratic in $e(t)$ and the term $2\xi^T(t) P e(t)$ is bounded and linear in $e(t)$. For any $\bar{\xi}$ there exists a finite $\bar{e} \in \mathbb{R}_+$ sufficiently large to ensure that for all $\{e(t)\text{: } ||e(t)|| > \bar{e}\}$ we have that $\dot{V}(t) < 0$ [137].

4.3.3 Experimental Setup and Results

To conduct HITL simulations of the parallel three-axis positioning system, the first axis is taken as the experimental piezoelectric actuator with the notch filter disabled in the control unit. The second axis is taken as the linear model with the notch filter enabled as in Fig. 4.2(a). The linear model with the notch filter is used due to sample time constraints as both models are being run in real-time along with the experimental system and the control law. The nonlinear model that is used for

the third axis is given by the summation of the hysteresis and creep operators as

$$y(t) = \phi(t) + y_c(t) \tag{4.43}$$

At a controlled system bias point, the nonlinear model can be identified by a nonlinear least squares technique as shown in Fig. 4.3. However, for the HITL simulations, a model identified at a different bias point (approximately 0.5 V higher) will be used. The different bias point will give a different behaviour of the piezoelectric as seen in Fig. 4.4. The parameters of this model are once again found by a nonlinear least squares technique. Here, seven hysteresis operators with threshold values $\vec{r} = [0 \quad 0.1285 \quad 0.2571 \quad 0.3857 \quad 0.5142 \quad 0.6428 \quad 0.7714]$ and weights $\vec{w}_h = [0.1280 \quad 0.0426 \quad 0.0595 \quad 0.0544 \quad 0.0602 \quad 0.0426 \quad 0.0282]$ are used. Next, five creep operators are used with $T_s = 0.001$ seconds, and with weights $\vec{w}_c = [0.6442 \quad 0.1902 \quad 0.0264 \quad 0.0560 \quad 0.0175]$. Finally, three saturation operators are used with threshold values found as $\vec{d} = [0 \quad 0.2873 \quad 0.5370]$ with respective weights $\vec{w}_s = [0.5574 \quad 0.2613 \quad 0.0617]$.

The system is set up to run with a sample rate of 10 kHz with $K_i = diag\{100, 100, 100\}$, $B = diag\{40, 40, 40\}$ and T is chosen as in Eq. 4.19.

4.3.3.1 Step: 300nm

For the piezoelectric, it is desired to follow a stair-type waveform, with individual steps of 300 nm. The response of the two models and the experimental system to

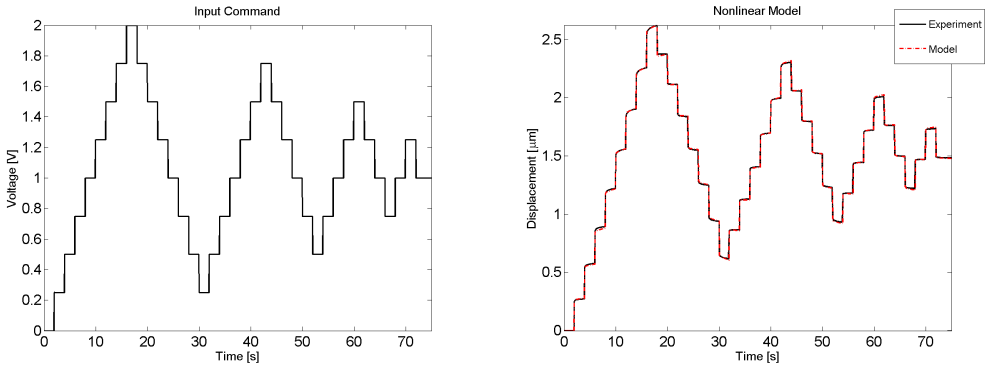

(a) Input voltage command for identification (b) Actual displacement vs. model

Fig. 4.3 Experimental results

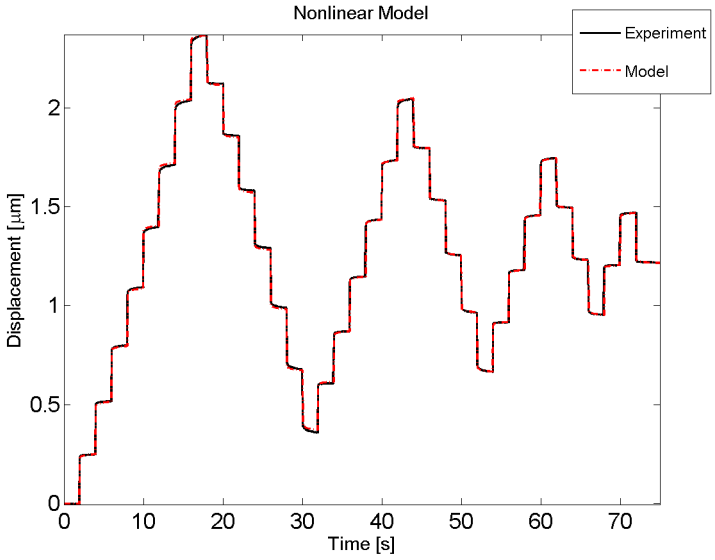

Fig. 4.4 Actual displacement vs. model for HITL simulation

the input can be seen in Fig. 4.5. The piezo, linear, and nonlinear model all exhibit different responses for different reasons. For the linear model, it was identified under small signal conditions, and for the nonlinear model, it was identified at a

different operating bias point.

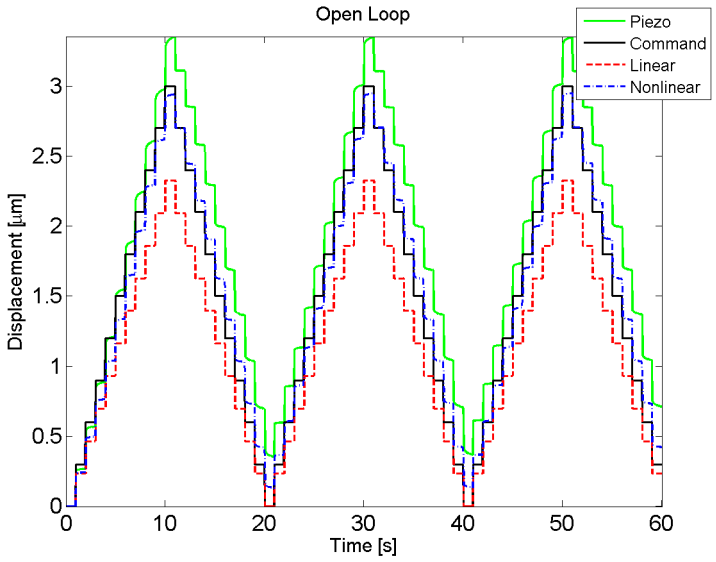

Fig. 4.5 Open loop experiments with 300 nm step

For comparison purposes, the response of the systems with individual integral controllers is shown in Fig. 4.6(a) for the full waveform, Fig. 4.6(c) for the step response, and Fig. 4.6(e) for the post-processed (analog Butterworth filtered) results. It can be seen that while the integral control has fair step tracking performance, the signals will all achieve different final values, which is undesirable. In Fig. 4.6(b) synchronization control for the full waveform can be seen, while in Fig. 4.6(d) shows the step response, and Fig. 4.6(f) shows the post-processed results. It can be seen in this case that all three systems are closely coupled together and achieve the desired reference value. Fig. 4.6(f) is further magnified in Fig. 4.7 where it can be

seen that the three systems responses are quite tightly bound, even in the presence of noise disturbances in the experimental system.

4.3.3.2 Step: 20nm

It is clearly desirable to have positioning capabilities smaller than the 300 nm step shown in the previous case. In this section, it is desired for the system to follow a waveform consisting of 20 nm steps. The open loop response of the system can be seen in Fig. 4.8, and it is interesting to note how different the response of the experimental system is from the larger 300 nm step size shown in Fig. 4.5.

Once again, for comparison purposes, the response of the systems with individual integral controllers is shown in Fig. 4.9(a) for the full waveform, Fig. 4.9(c) for the step response, and Fig. 4.9(e) for the filtered step response. Synchronization control for the full waveform can be seen in Fig. 4.9(b), while the step response can be seen in Fig. 4.9(d), and Fig. 4.9(f) shows the filtered response. Once again, it can be seen that the synchronization control holds the signals values together quite well, even in the rather noisy environment. It is worth noting that the controller itself is run without any filtering inside the loop as it depends entirely on integral control, and hence is fairly robust to noise. With more advanced signal processing techniques, it should be possible to reduce the achievable step size to the nanometer level.

4.3.3.3 Sine Wave Tracking

In this section, the controller is configured to track a sine wave with a peak-to-peak displacement of 2 μm at frequencies of 1, 5, 10, and 20 Hz. For this, the gains can be tuned much larger to make the region converged to smaller, as overshoot is not a critical factor. However, the gains cannot be made larger indefinitely before driving the closed loop system unstable. Here, the gains are chosen as $K_i = diag\{1250, 1250, 1250\}$, $B = diag\{250, 250, 250\}$ and T is chosen as in Eq. 4.19.

Fig. 4.10 shows the open loop response of the system to a sinusoidal input. The uncontrolled response will always lag the input and has substantial errors near the peaks and troughs of the waveform. In Fig. 4.11(a) the response of the synchronization control can be seen for a 1 Hz sine wave, and its response at the peak is magnified in Fig. 4.11(b). While the error is very small, the waveforms aren't particularly synchronized at this point, although they are on the ascending and descending branches of the wave. Fig. 4.12–4.14 shows the response of the controller to increasing frequency of the sinusoidal waveform, and in Fig. 4.15 the max error (at the peak) versus frequency is shown. Clearly, as the frequency of the waveform increases, the error also increases, although it is worth noting, the actuators are all still relatively held together by the synchronization controller.

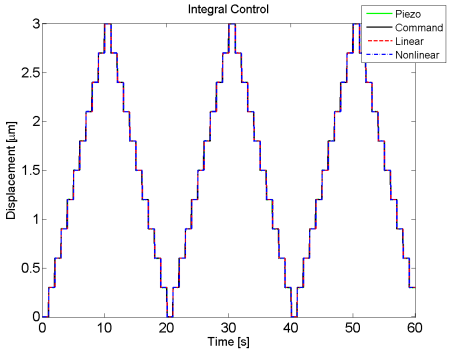

(a) Integral control

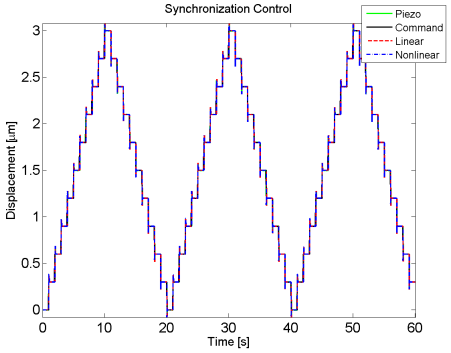

(b) Synchronization control

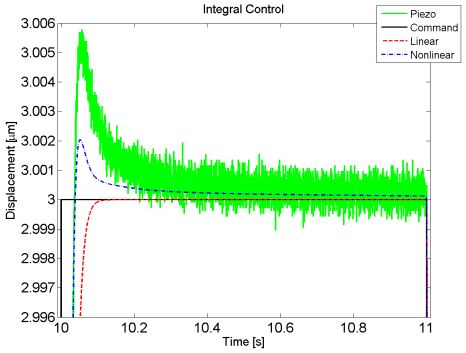

(c) Integral control step response

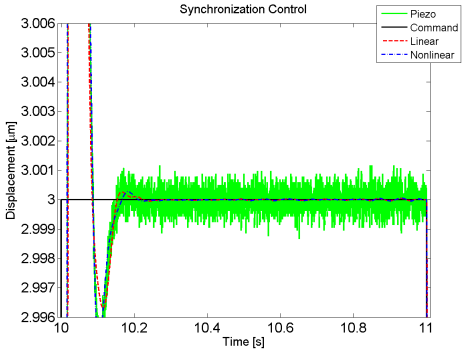

(d) Synchronization control step response

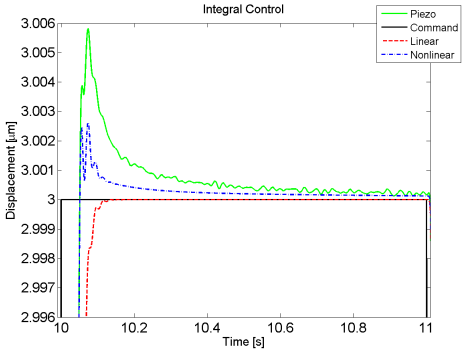

(e) Integral control step response filtered

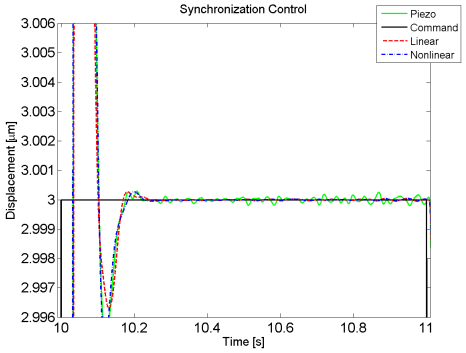

(f) Synchronization control step response filtered

Fig. 4.6 Experimental results with 300 nm step

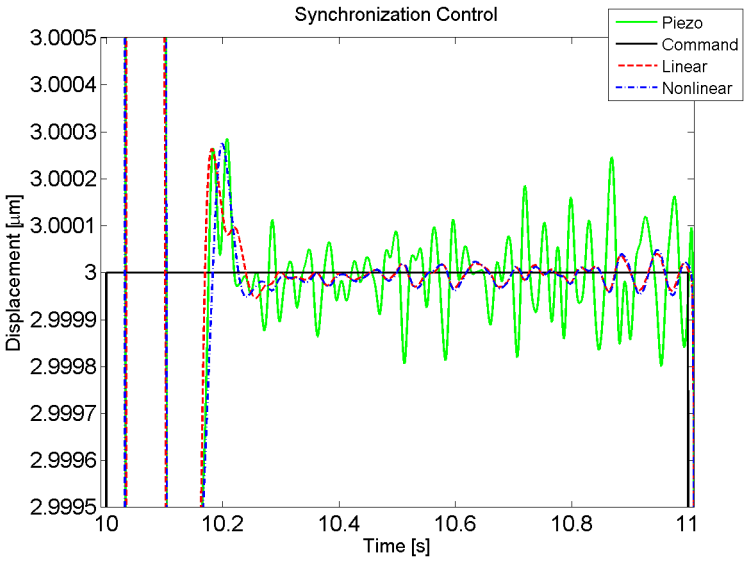

Fig. 4.7 Magnification of Fig. 4.6(f)

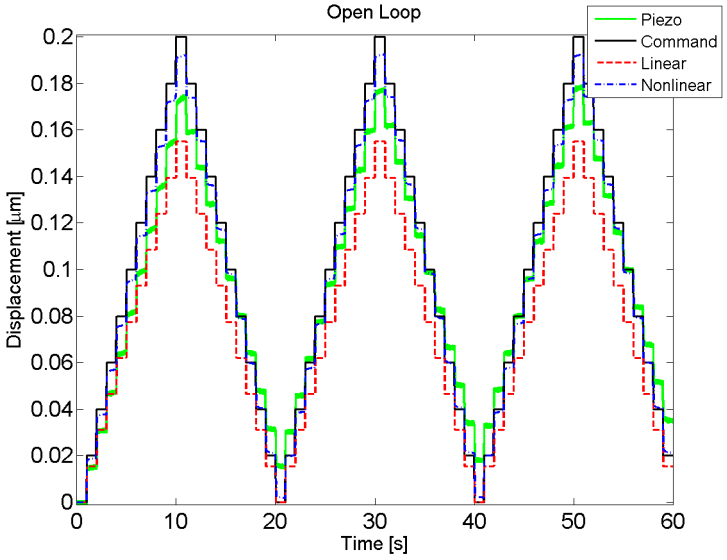

Fig. 4.8 Open loop experiments with 20 nm step

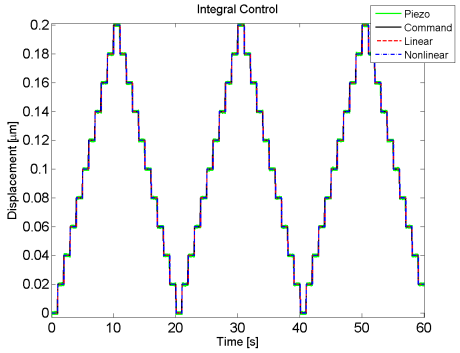

(a) Integral control

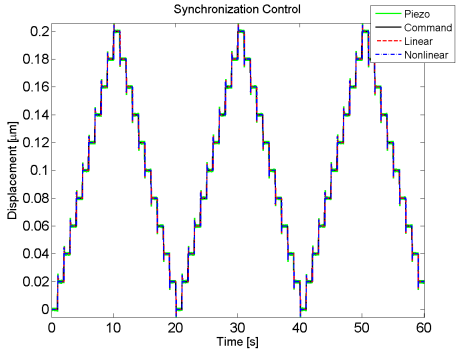

(b) Synchronization control

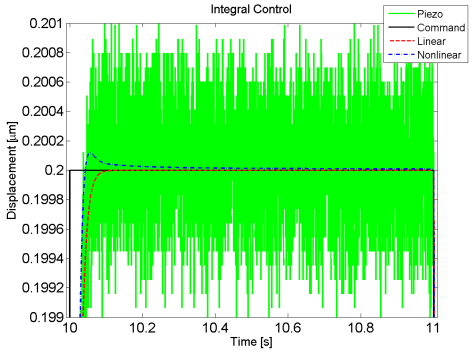

(c) Integral control step response

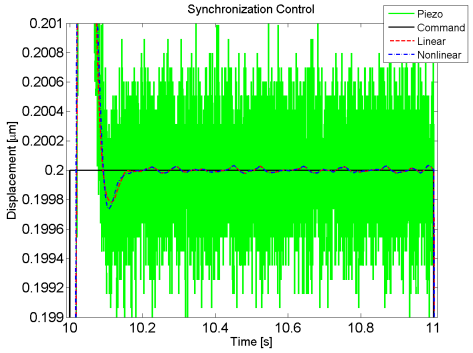

(d) Synchronization control step response

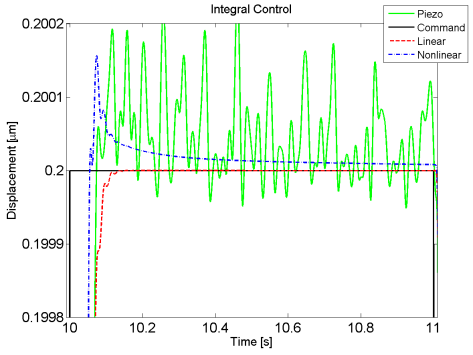

(e) Integral control step response filtered

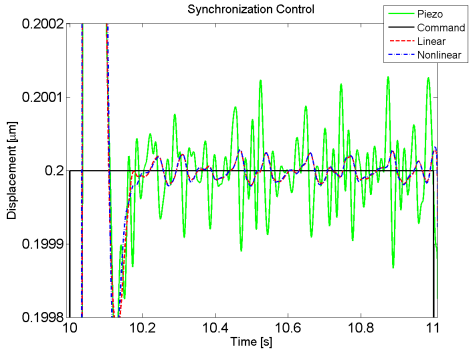

(f) Synchronization control step response filtered

Fig. 4.9 Experimental results with 20 nm step

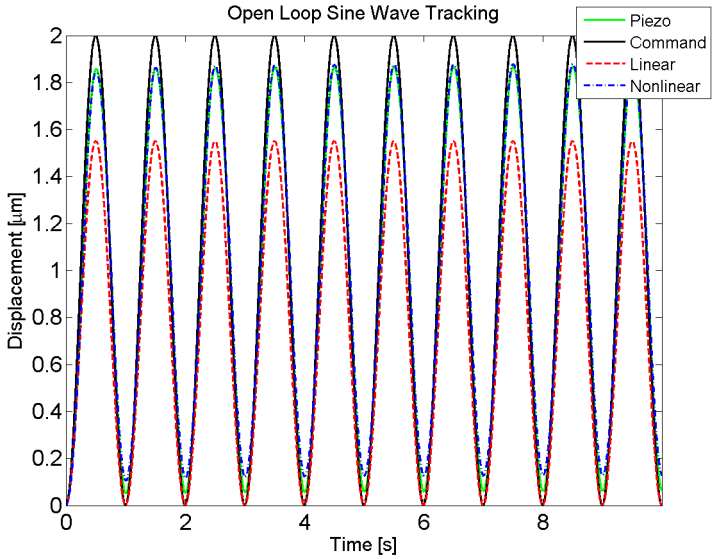

Fig. 4.10 Open loop response for a 1 Hz sine wave

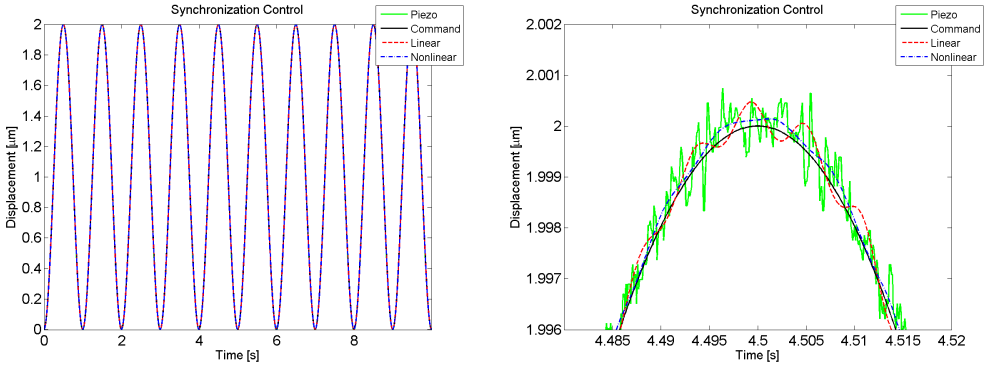

(a) Synchronization control (b) Magnified

Fig. 4.11 Tracking of a sine wave at 1 Hz

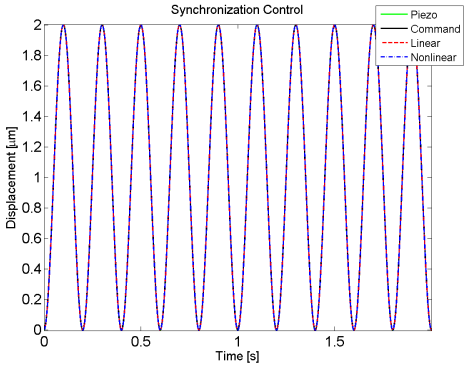

(a) Synchronization control

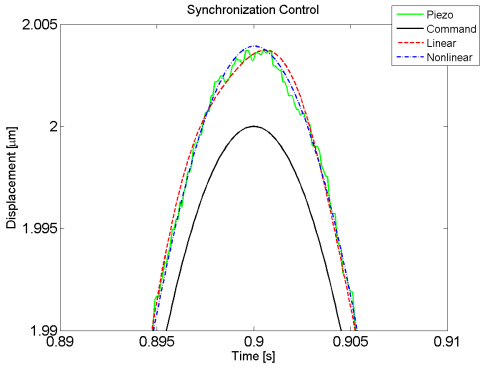

(b) Magnified

Fig. 4.12 Tracking of a sine wave at 5 Hz

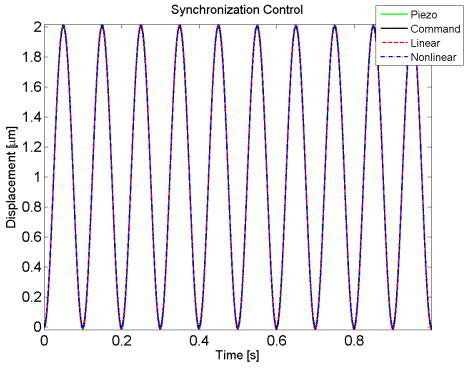

(a) Synchronization control

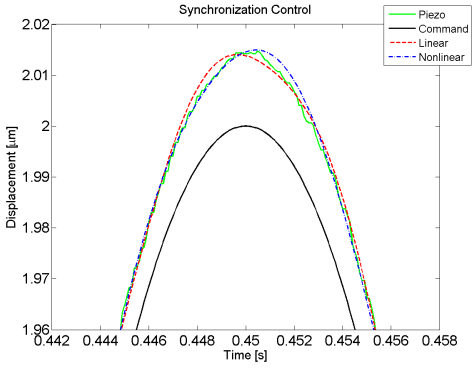

(b) Magnified

Fig. 4.13 Tracking of a sine wave at 10 Hz

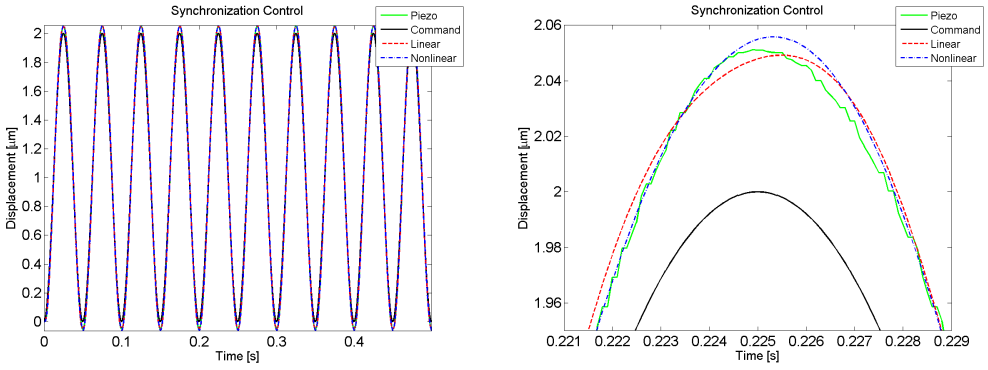

(a) Synchronization control (b) Magnified

Fig. 4.14 Tracking of a sine wave at 20 Hz

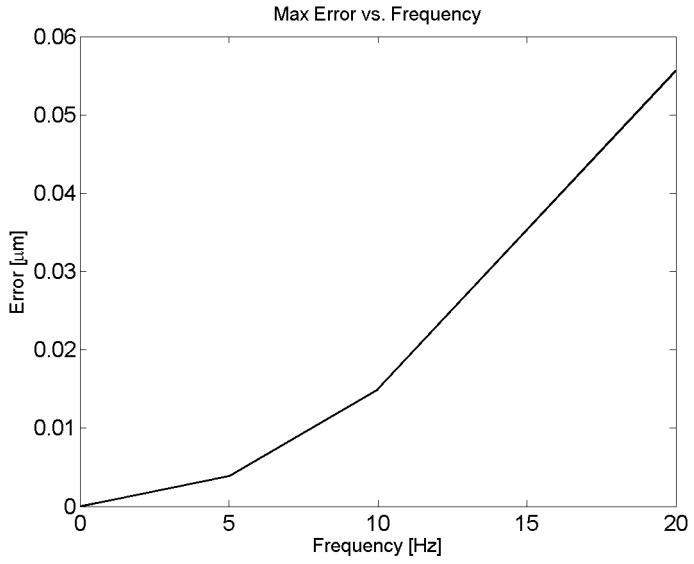

Fig. 4.15 Maximum error vs. waveform frequency

4.4 Output Feedback Integral Control with Input Nonlinearities

The piezoelectric actuators dynamic model can be represented as a single-input-single-output linear state space system, with its inherent nonlinearities considered as a nonlinearity on the input. This can be written as

$$\dot{x} = Ax + B\phi(u) \tag{4.44}$$

$$y = Cx + D\phi(u) \tag{4.45}$$

where $x \in \mathbb{R}^n$, $A \in \mathbb{R}^{n\times n}$, $B \in \mathbb{R}^{n\times 1}$, $C \in \mathbb{R}^{1\times n}$, $D \in \mathbb{R}$, and $u,\ y \in \mathbb{R}$, $\phi : \mathbb{R}_+ \times \mathbb{R} \to \mathbb{R}$. With $G(s) = C(sI - A)^{-1}B + D$, this can be represented grapically as in Fig. 4.16. The input nonlinearity of the piezoelectric actuator can be represented by the Prandtl-Ishlinskii phenomenological model of hysteresis as presented in Section 4.2.2.

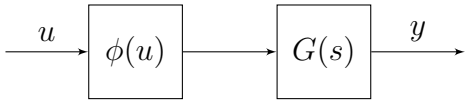

Fig. 4.16 Plant block diagram

4.4.1 Integral Control with Input Nonlinearities

The state space representation of a single-input-single-output system with input nonlinearities is given in Eq. 4.44–4.45 where it is assumed that A is Hurwitz. In transfer function form, $G(s) = C(sI - A)^{-1}B + D$, and it is assumed that the static gain $G(0) = D - CA^{-1}B > 0$. With integral control, the feedback sytem can be seen in Fig. 4.17 and the system of equations can be written as

$$\dot{x} = Ax + B\phi(u) \tag{4.46}$$

$$y = Cx + D\phi(u) \tag{4.47}$$

$$\dot{u} = k[r - y] \tag{4.48}$$

where $r \in \mathbb{R}$ is the constant reference to be tracked.

The control system will be stable for any $K^* > 0$ such that

$$1 + K^* \mathrm{Re}\left[\frac{G(iw)}{iw}\right] \geq 0 \tag{4.49}$$

and the maximal gain $K \in \mathbb{R}$ (K ¿ 0) can be defined as

$$\inf_{\omega \in \mathbb{R},\, \omega \neq 0} \mathrm{Re}\left[\frac{G(iw)}{iw}\right] = -\frac{1}{K} \tag{4.50}$$

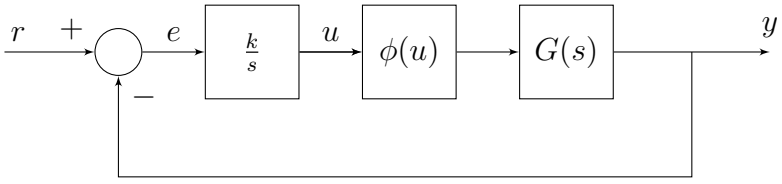

Fig. 4.17 System block diagram

which is closely related to the circle criterion. In fact, finding K is most easily done from a Nyquist plot of $G(iw)/(iw)$ where the plot can touch, but otherwise must lie to the right of the vertical line defined by $-\frac{1}{K}$. For heavily damped systems, this may present a large reduction in the maximum gain possible, as the condition is conservative in nature. Borrowing from the circle criterion, it can be seen that essentially we are claiming that the maximum gain of the nonlinearity times that of the integral controller will belong to the sector (0, K).

For the nonlinearity $\phi()$, it will be imposed that it must be piecewise continuously differentiable and non-decreasing, $\beta\phi(\beta) \geq 0$, and is globally Lipschitz with Lipschitz continuity constant λ. Since ϕ is nondecreasing, hence $\phi^{\nabla}(\beta) \geq 0$, where $\phi^{\nabla}(\beta)$ is defined as $\min\{\phi'_{-}(\beta), \phi'_{+}(\beta)\}$, where $\phi'_{-}(\beta)$ and $\phi'_{+}(\beta)$ are the left and right limits and $\phi^{\nabla}(\beta) = \phi'(\beta)$ whenever ϕ' exists. Hence, we can take $k^* = K/\lambda$, then choose $k, k_* > 0$, such that $k < k_* < k^*$. Hence k^* represents the maximum gain of the integral controller (since the gain due to the input nonlinearity has been removed) such that the system remains stable and k_* such that the system is asymptotically stable. It will be presumed that the initial value problem given by Eq. 4.46–4.48 with $x(0) = x_0$ and $u(0) = u_0$ has a unique solution.

4.4.1.1 Lyapunov Stability

To prove Lyapunov stability, a coordinate change will first be employed. Defining $z(t) = x(t) + A^{-1}B\phi(u)$, hence $\dot{z}(t) = \dot{x}(t) + A^{-1}B\phi^{\nabla}(u)\dot{u}$ we have that Eq. 4.46 becomes

$$\begin{aligned} \dot{z} - A^{-1}B\phi^{\nabla}(u)\dot{u} &= A(z - A^{-1}B\phi(u)) + B\phi(u) && (4.51) \\ \dot{z} &= Az + A^{-1}B\phi^{\nabla}(u)\dot{u} && (4.52) \end{aligned}$$

Let $v = \phi(u) - \phi(u^*)$, hence $\dot{v} = \phi^{\nabla}(u)\dot{u}$, then

$$\dot{z} = Az + A^{-1}B\dot{v} \tag{4.53}$$

Next, employing the coordinate transform on the output equation, it becomes

$$\begin{aligned} y &= Cx + D\phi(u) && (4.54) \\ &= C(z - A^{-1}B\phi(u)) + D\phi(u) && (4.55) \\ &= Cz + (D - CA^{-1}B)\phi(u) && (4.56) \\ &= Cz + G(0)(v + \phi(u^*)) && (4.57) \\ &= Cz + G(0)v + G(0)\phi(u^*) && (4.58) \end{aligned}$$

Defining $w = y - G(0)\phi(u^*)$ we have that

$$w = Cz + G(0)v \tag{4.59}$$

Now, the integral control equation will become, with $\eta = \phi^{\nabla}(u)$

$$\begin{aligned}
\dot{v} &= \phi^{\nabla}(u)\dot{u} && (4.60)\\
&= \eta k[r - y] && (4.61)\\
&= \eta[kr - kCz - kG(0)v - kG(0)\phi(u^*)] && (4.62)\\
&= \eta[-kCz - kG(0)v] && (4.63)\\
&= -kw\eta && (4.64)
\end{aligned}$$

where the fact that $r = G(0)\phi(u^*)$ was used.

Assembling Eq.'s 4.53, 4.59, and 4.64 we have that

$$\begin{aligned}
\dot{z} &= Az + A^{-1}B\dot{v} && (4.65)\\
w &= Cz + G(0)v && (4.66)\\
\dot{v} &= -kw\eta && (4.67)
\end{aligned}$$

which can be written in matrix form as

$$\begin{aligned}
\begin{bmatrix} \dot{z} \\ \dot{v} \end{bmatrix} &= \begin{bmatrix} A & 0 \\ 0 & 0 \end{bmatrix} \begin{bmatrix} z \\ v \end{bmatrix} + \begin{bmatrix} A^{-1}B \\ 1 \end{bmatrix} \dot{v} && (4.68)\\
w &= \begin{bmatrix} C & G(0) \end{bmatrix} \begin{bmatrix} z \\ v \end{bmatrix} && (4.69)\\
\dot{v} &= -kw\eta && (4.70)
\end{aligned}$$

which is equivalent to

$$\begin{aligned}
\begin{bmatrix} \dot{z} \\ \dot{v} \end{bmatrix} &= \begin{bmatrix} A & 0 \\ 0 & 0 \end{bmatrix} \begin{bmatrix} z \\ v \end{bmatrix} - \begin{bmatrix} A^{-1}B \\ 1 \end{bmatrix} kw\eta && (4.71)\\
w &= \begin{bmatrix} C & G(0) \end{bmatrix} \begin{bmatrix} z \\ v \end{bmatrix} && (4.72)
\end{aligned}$$

Taking the Lyapunov function candidate as $V = z^T P z + G(0)v^2$, it's time derivative is given as

$$\begin{aligned}
\dot{V} &= \dot{z}^T P z + z^T P \dot{z} + 2G(0)v\dot{v} && (4.73)\\
&= (Az + A^{-1}B\dot{v})^T P z + z^T P(Az + A^{-1}B\dot{v}) + 2G(0)v\dot{v} && (4.74)\\
&= z^T A^T P z + \dot{v}(A^{-1}B)^T P z + z^T P A z + z^T P A^{-1} B\dot{v} + 2G(0)v\dot{v} && (4.75)\\
&= z^T(A^T P + PA)z + 2z^T P A^{-1} B\dot{v} + 2G(0)v\dot{v} && (4.76)
\end{aligned}$$

with $G(0)v = w - Cz$ we have

$$\begin{aligned}
\dot{V} &= z^T(A^T P + PA)z + 2z^T P A^{-1} B\dot{v} + 2(w - Cz)\dot{v} && (4.77)\\
&= z^T(A^T P + PA)z + 2z^T P A^{-1} B\dot{v} + 2w\dot{v} - 2z^T C^T\dot{v} && (4.78)\\
&= z^T(A^T P + PA)z + 2z^T(PA^{-1}B - C^T)\dot{v} + 2w\dot{v} && (4.79)\\
&= \begin{bmatrix} z \\ v \end{bmatrix}\begin{bmatrix} A^T P + PA & PA^{-1}B - C^T \\ (A^{-1}B)^T P - C & -2\Delta \end{bmatrix}\begin{bmatrix} z \\ v \end{bmatrix} + 2\Delta\dot{v}^2 + 2w\dot{v} && (4.80)
\end{aligned}$$

with $\dot{v} = -kw\eta$. There exists a $Q < 0$ (see [134]) such that

$$Q = \begin{bmatrix} A^T P + PA & PA^{-1}B - C^T \\ (A^{-1}B)^T P - C & -2\Delta \end{bmatrix} \quad (4.81)$$

where $P = P^T > 0$, $P \in \mathbb{R}^{n\times n}$, we then have

$$\begin{aligned}
\dot{V} &= \begin{bmatrix} z \\ v \end{bmatrix} Q \begin{bmatrix} z \\ v \end{bmatrix} + 2\Delta k^2 w^2\eta^2 + 2w^2 k\eta && (4.82)\\
&= \begin{bmatrix} z \\ v \end{bmatrix} Q \begin{bmatrix} z \\ v \end{bmatrix} + 2kw^2\eta(\Delta k\eta - 1) && (4.83)\\
&= \begin{bmatrix} z \\ v \end{bmatrix} Q \begin{bmatrix} z \\ v \end{bmatrix} - 2kw^2\eta(1 - \Delta k\eta) && (4.84)
\end{aligned}$$

Here, $k > 0$, $w^2 \geq 0$, $\eta = \phi^{\nabla}(u(t)) \geq 0$ since ϕ is non-decreasing. With $\Delta = \frac{1}{k_* \lambda}$ we have that $1 - \Delta k\eta = 1 - \frac{k\eta}{k_* \lambda} > 0$ since $k_* > k$ and $\lambda > \eta$. Hence,

$$\begin{aligned} \dot{V} &= \begin{bmatrix} z \\ v \end{bmatrix} Q \begin{bmatrix} z \\ v \end{bmatrix} - 2kw^2\eta(1 - \Delta k\eta) && (4.85) \\ \dot{V} &\leq \begin{bmatrix} z \\ v \end{bmatrix} Q \begin{bmatrix} z \\ v \end{bmatrix} && (4.86) \\ \dot{V} &< 0 && (4.87) \end{aligned}$$

4.4.1.2 Properties of the Hysteresis Nonlinearity

The Prandtl-Ishlinskii operator is piecewise monotonic which means that the operator $\Psi_a[u]$ is a monotone function of t in any time interval where the input u is monotone with respect to t. If the operator is monotone, all local extrema of the output $\Psi_a[u]$ must correspond to local extrema of u, and no new ones can be created. $\Psi_a[u]$ is continuous at each $t \in \mathbb{R}_+$, $t \neq t_i$ and is both left and right continuous at t_i [135]. The play operator is Lipschitz continuous on the dense subset $C_{pm}(\mathbb{R}_+) \times \mathbb{R}$ of $C(\mathbb{R}_+) \times \mathbb{R}$ [135]. Consequently, Ψ_a can be uniquely extended onto $C(\mathbb{R}_+) \times \mathbb{R}$ and is Lipschitz continuous [121, 135]. Clearly, the same arguments can be made for the saturation operator as were made for the play operator.

To see the global Lipschitz condition of the modified PI operator, take (in a slight abuse of notation),

$$\|\phi(u) - \phi(v)\| \leq \lambda \|u - v\| \qquad (4.88)$$

$$\|w_s^T\Phi[w_h^T\Psi[u]] - w_s^T\Phi[w_h^T\Psi[v]]\| \leq \lambda\|u-v\| \tag{4.89}$$

$$\|w_s^T\|\|\Phi[w_h^T\Psi[u]] - \Phi[w_h^T\Psi[v]]\| \leq \lambda\|u-v\| \tag{4.90}$$

Employing the fact that $\|\Phi[u] - \Phi[v]\| \leq \|u-v\|$ (ie. has a Lipschitz constant of 1), we then have that

$$\|w_s^T\|\|w_h^T\Psi[u] - w_h^T\Psi[v]\| \leq \lambda\|u-v\| \tag{4.91}$$

$$\|w_s^T\|\|w_h^T\|\|\Psi[u] - \Psi[v]\| \leq \lambda\|u-v\| \tag{4.92}$$

and since $\|\Psi[u] - \Psi[v]\| \leq \|u-v\|$ (again, has a Lipschitz constant of 1), we have that $\|w_s^T\|\|w_h^T\| \leq \lambda$. Given that the weights w_h and w_s represent the slopes of each operator, choosing the Taxicab norm (or 1-norm) places a bound on the maximum slope of the hysteresis operator in its input-output space, hence $\|w_s^T\|_1\|w_h^T\|_1 \leq \lambda$.

4.4.1.3 A Simple Illustrative Example

As a simple example, consider the second order system given by

$$\dot{x} = \begin{bmatrix} 0 & 1 \\ -\omega^2 & -2\zeta\omega \end{bmatrix} + \begin{bmatrix} 0 \\ g\omega^2 \end{bmatrix}\phi(u) \tag{4.93}$$

$$y = \begin{bmatrix} 1 & 0 \end{bmatrix} \tag{4.94}$$

with $\omega = 10$, $g = 0.9$, and $\zeta = 0.2$. From the Routh-Hurwitz condition, we can easily find that for integral control, the gain range for stability is

$$0 < K_{RH}^* \leq \frac{2\zeta\omega}{g} = 4.444 \tag{4.95}$$

and can set $K_{RH} = \sup\{K^*_{RH}\}$ while from Eq. 4.49 we can evaluate the Nyquist plot of $\frac{G(i\omega)}{i\omega}$ (see Fig. 4.18) to find $K = 4.2667$.

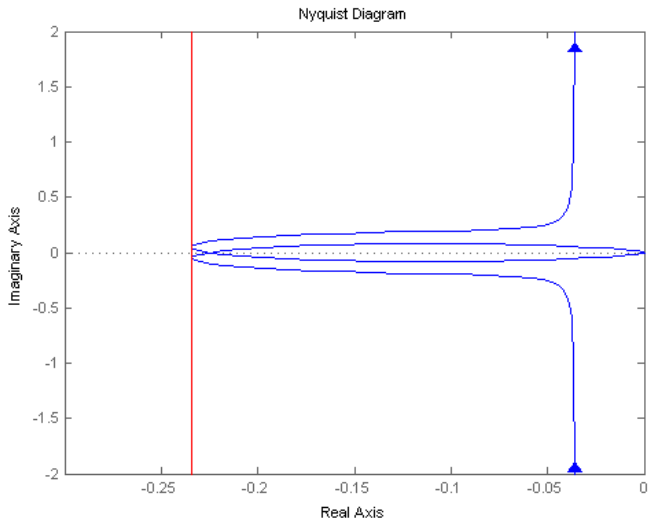

Fig. 4.18 Nyquist plot of $\frac{G(i\omega)}{i\omega}$

For second order systems, as $\zeta \to 0$, K will tend towards K_{RH}, hence the condition of Eq. 4.49 is conservative, and will become more so for heavily damped systems. As the threshold a increases, in general so could the maximum gain, however, this would require exact knowledge of the thresholds and weights. As a tends towards zero, it is apparent that the maximum allowable gain will approach that of strictly the linear system scaled by $\|w_h^T\|_1$. As a simple example, take the first hystersis operator with $a_1 = 0.01$, with weight $w_{h_1} = 1.2 = \lambda$, and $k = k_N = K - 0.001$. With this gain k, the system will be unstable. In this case, taking

$k = k_N/w_{h_1}$ the system is stable as can be seen in Fig. 4.19.

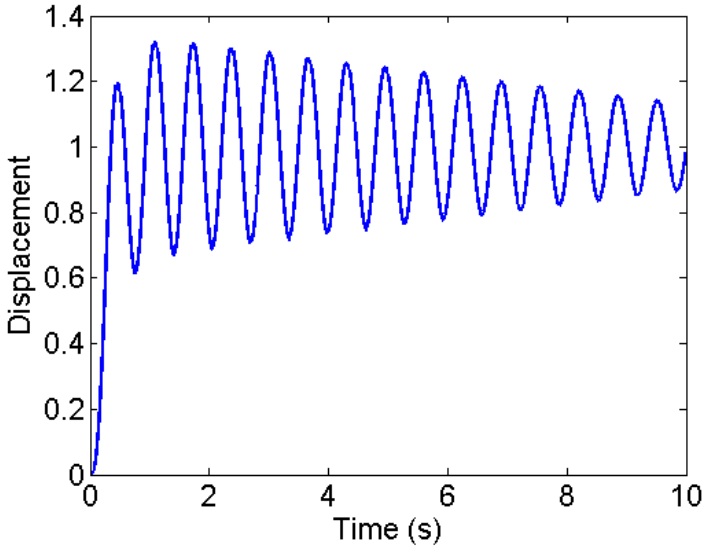

Fig. 4.19 Integral control with $k = k_N/\lambda$

Now, including the linear portion of the saturation operator as $d_0 = 0$ with $w_{s_0} = 0.9$ and one saturation operator with $d_1 = 0.75$ and $w_{s_1} = 1.4$, the response with $k = k_N/w_{h_1}$ will again be unstable. Choosing $k = k_N/(w_{h_1}(w_{s_0} + w_{s_1}))$ results in the stable response seen in Fig. 4.20

4.4.2 Application to the Piezoelectric Actuator

With the notch filter off, the linear portion of the actuator response can be described very precisely by an eighth order transfer function as

$$G(s) = \frac{\beta_0}{s^8 + \alpha_7 s^7 + \alpha_6 s^6 + \alpha_5 s^5 + \alpha_4 s^4 + \alpha_3 s^3 + \alpha_2 s^2 + \alpha_1 s + \alpha_0} \tag{4.96}$$

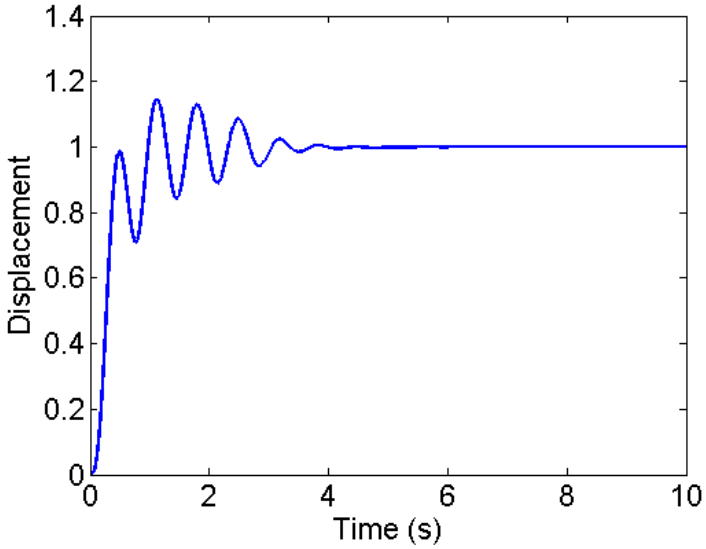

Fig. 4.20 Integral control with $k = k_N/(w_{h_1}(w_{s_0} + w_{s_1}))$

This transfer function was found from a least squares fit in the frequency domain and the frequency response of the actuator versus its model can be seen in Fig. 4.4.2 with its identified parameters found in Table 4.1. The transfer function represents that of the actuator from input voltage to output displacement.

Table 4.1 Linear transfer function model parameters

Parameter	β	α
0	2.3390e+035	2.6321e+035
1		6.7826e+031
2		6.7762e+027
3		3.6852e+023
4		1.3854e+019
5		3.1715e+014
6		7.1636e+009
7		6.9612e+004

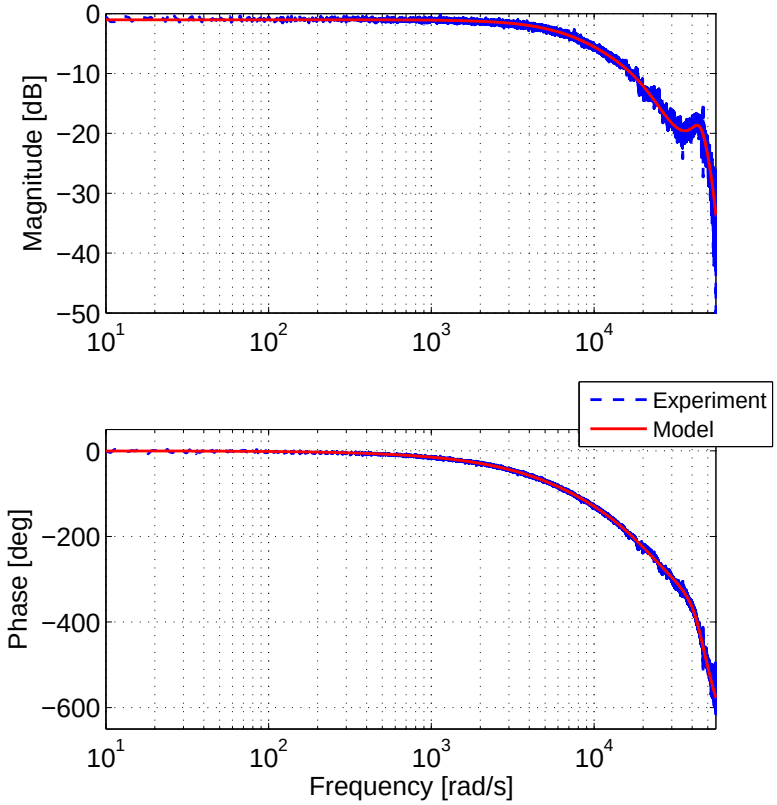

Fig. 4.21 Frequency response

At a controlled system bias point, the nonlinear model can be identified by a nonlinear least squares technique as shown in Fig. 4.22. Here, seven hysteresis operators, and five saturation operators are identified and their values and respective weights can be seen in Table 4.2. The choice of 10 Hz for identification was made as it is much easier to identify the hysteresis parameters when creep is not present, which is generally the case for sinusoids greater than 1 Hz. Creep was not consid-

ered in the analysis of the stability problem, as the creep response is much slower than that of the dynamics of the system.

Table 4.2 Identified parameters of the piezoelectric

Parameter	0	1	2	3	4	5	6
a	0	0.1667	0.3333	0.5	0.6667	0.8333	1
w_h	1.0540	0.0546	0.0481	0.0445	0.0163	0.0642	0.2258
d	0	1.0001	1.1102	1.6517	1.9773		
w_s	1.028	0.0068	0.0050	0.0037	0.0035		

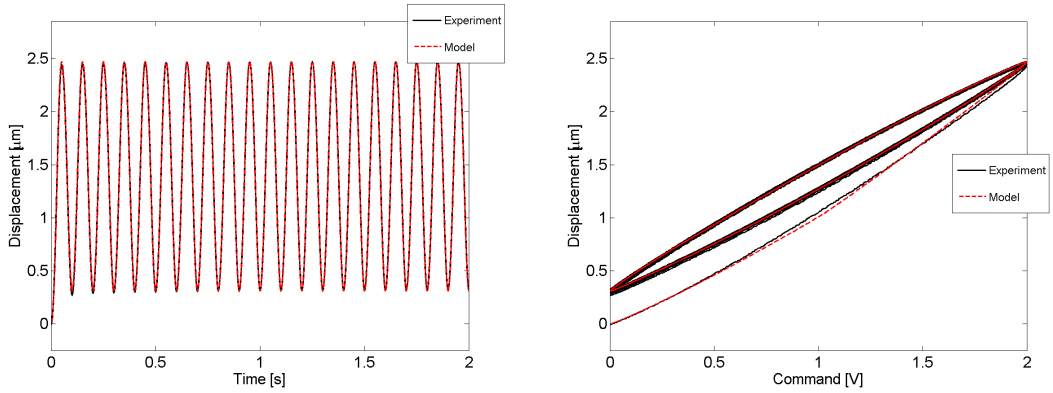

(a) Hysteresis identification (b) Input-output

Fig. 4.22 Experiments and identified model for hysteresis

From the identified nonlinear parameters, we can calculate, $\|w_h^T\|_1 = 1.5078$, and $\|w_s^T\|_1 = 1.0481$. From the Nyquist plots in Fig. 4.23 we can calculate $K \leq \frac{1}{2.2898\times 10^4} = 4.3671 \times 10^3$. Hence, $k^* = K/\lambda = \frac{K}{\|w_h^T\|_1 \|w_s^T\|_1} = 2.7634 \times 10^3$. Hence, defining $k = 2.762 \times 10^3$ ensures that $k < k_* < k^*$, and global asymptotic stability of the system.

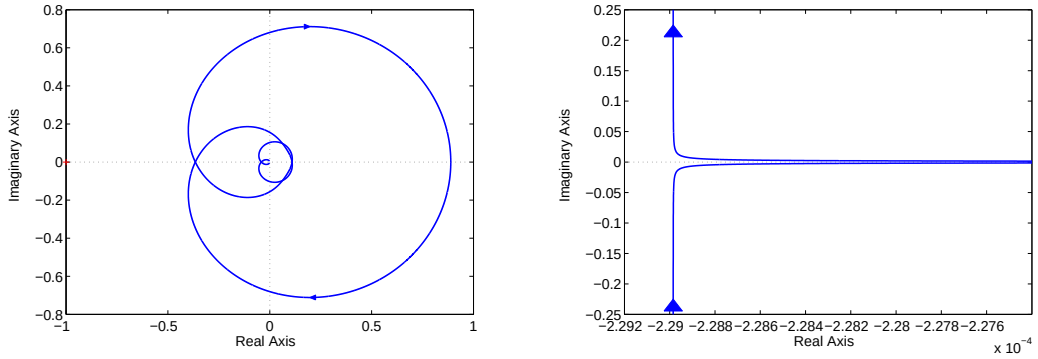

(a) Linear system

(b) Linear system with unity gain integral control (magnified)

Fig. 4.23 Nyquist plots

An experiment is set up to verify that this gain ($k = 2.762 \times 10^3$) is indeed stable. The xPC target machine is configured to run at 100 kHz, to move the piezoelectric actuator from 0 to 2.4μm. The result can be seen in Fig. 4.24(a) which confirms that the system is indeed asymptotically stable, and as expected, there is an overshoot, with a fast settling time and no steady state error. The control signal generated in volts can also be seen in Fig. 4.24(b). While this gain is quite large, much higher integral gains could be chosen with the system remaining asymptotically stable, however, this is due to the conservative nature of the condition, and the lack of a dominant resonance mode in the system. For some piezoelectric actuators with more dominant resonances at lower frequencies (or with amplifiers with larger bandwidths), the condition will yield closer to the true maximum possible integral

gain. It should also be noted that the fitted parameters of w_h and w_s depend on a variety of conditions, including the accuracy of their identification, and should be used with care in their definition of λ. The appropriateness of the choice of gain will also depend on a variety of issues not considered in the analysis, including sample rate, system noise, quantization effects, time delay, and other effects that are always encountered in practice.

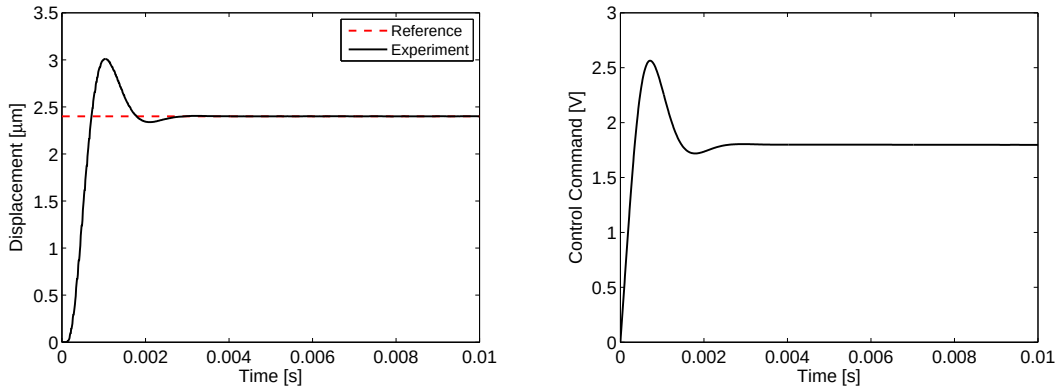

(a) System response (b) Control output

Fig. 4.24 Experiment with maximum integral gain

4.5 Output Feedback Integral Synchronization Control with Input Nonlinearities

It is desired to synchronize two systems described by linear, finite-dimensional, state space systems subject to input nonlinearities. While the derivation is pre-

sented for two systems, the extension to more systems is relatively straightforward. For this, an integral synchronization control law is designed as

$$u(t) = \begin{bmatrix} u_1(t) \\ u_2(t) \end{bmatrix} = K \int_0^t [r - y(\tau)] d\tau = \begin{bmatrix} k & -k_c \\ -k_c & k \end{bmatrix} \int_0^t \begin{bmatrix} r - y_1(\tau) \\ r - y_2(\tau) \end{bmatrix} d\tau \quad (4.97)$$

where $u \in \mathbb{R}^2$, $y \in \mathbb{R}^2$, $K \in \mathbb{R}^{2\times 2}$ with $K = K^T > 0$, and $r \in \mathbb{R}$ is the constant reference to be tracked.

With integral control, the system of equations can be written as

$$\dot{x}_1 = A_1 x_1 + B_1 \phi_1(u_1) \quad (4.98)$$

$$y_1 = C_1 x_1 + D_1 \phi_1(u_1) \quad (4.99)$$

$$\dot{u}_1 = k[r - y_1] - k_c[r - y_2] \quad (4.100)$$

$$\dot{x}_2 = A_2 x_2 + B_2 \phi_2(u_2) \quad (4.101)$$

$$y_2 = C_2 x_2 + D_2 \phi_2(u_2) \quad (4.102)$$

$$\dot{u}_2 = k[r - y_2] - k_c[r - y_1] \quad (4.103)$$

where it is assumed that A_1 and A_2 are Hurwitz. In transfer function form, $G_1(s) = C_1(sI - A_1)^{-1}B_1 + D_1$, and it is assumed that the static gain $G_1(0) = D_1 - C_1 A_1^{-1} B_1 > 0$ with the same assumptions on $G_2(s)$ and $G_2(0)$.

For the uncoupled systems, they will be stable for any $K^* > 0$ such that $I + K^* \frac{G(iw)}{iw}$ is positive real, where I is the identity matrix, and $G(iw)$ is the 2×2

transfer function matrix given by

$$G(iw) = \begin{bmatrix} G_1(iw) & 0 \\ 0 & G_2(iw) \end{bmatrix} \tag{4.104}$$

To find the maximal gain for each system, first from the complex frequency response we can establish

$$\inf_{\omega\in\mathbb{R},\,\omega\neq 0} \mathrm{Re}\left[\frac{G_1(iw)}{iw}\right] = -\frac{1}{k_{1_*}} \tag{4.105}$$

$$\inf_{\omega\in\mathbb{R},\,\omega\neq 0} \mathrm{Re}\left[\frac{G_2(iw)}{iw}\right] = -\frac{1}{k_{2_*}} \tag{4.106}$$

Then, the maximum gain matrix can be defined as

$$K_* = \begin{bmatrix} k_{1_*} & 0 \\ 0 & k_{2_*} \end{bmatrix} \tag{4.107}$$

The Lipschitz constant for each nonlinearity given by λ_1, λ_2 gives rise to the definition of

$$\Lambda = \begin{bmatrix} \lambda_1 & 0 \\ 0 & \lambda_2 \end{bmatrix} \tag{4.108}$$

Hence, we can take $\bar{K} = \Lambda^{-1}K_*$, then choose $K, \tilde{K} > 0$, such that $K < \tilde{K} < \bar{K}$. Hence $\bar{K}$ represents the maximum gain of the integral control (since the gain due to the input nonlinearity has been removed) such that the system remains stable and $\tilde{K}$ such that the system is asymptotically stable. The synchronization gain matrix $K = K^T > 0$ with $K < \tilde{K}$ is defined as

$$K = \begin{bmatrix} k & -k_c \\ -k_c & k \end{bmatrix} \tag{4.109}$$

We can now also define for later use, $\Delta = \Lambda^{-1}\tilde{K}^{-1}$.

4.5.1 Lyapunov Stability

To prove Lyapunov stability, a coordinate change will first be employed. Defining $z_1(t) = x_1(t) + A_1^{-1}B_1\phi_1(u_1)$, hence $\dot{z}_1(t) = \dot{x}_1(t) + A_1^{-1}B_1\phi_1^{\nabla}(u_1)\dot{u}_1$ we have that Eq. 4.98 becomes

$$\begin{aligned} \dot{z}_1 - A_1^{-1}B_1\phi_1^{\nabla}(u_1)\dot{u}_1 &= A_1(z_1 - A_1^{-1}B_1\phi_1(u_1)) + B_1\phi_1(u_1) && (4.110) \\ \dot{z}_1 &= A_1 z_1 + A_1^{-1}B_1\phi_1^{\nabla}(u_1)\dot{u}_1 && (4.111) \end{aligned}$$

Let $v_1 = \phi_1(u_1) - \phi_1(u_1^*)$, hence $\dot{v}_1 = \phi_1^{\nabla}(u_1)\dot{u}_1$, then

$$\dot{z}_1 = A_1 z_1 + A_1^{-1}B_1\dot{v}_1 \tag{4.112}$$

and with a similar coordinate change and $v_2 = \phi_2(u_2) - \phi_2(u_2^*)$ on Eq. 4.101 it becomes

$$\dot{z}_2 = A_2 z_2 + A_2^{-1}B_2\dot{v}_2 \tag{4.113}$$

Next, employing the coordinate transform on the output equation, it becomes

$$\begin{aligned} y_1 &= C_1 x_1 + D_1\phi(u_1) && (4.114) \\ &= C_1(z_1 - A_1^{-1}B_1\phi_1(u_1)) + D_1\phi(u_1) && (4.115) \\ &= C_1 z_1 + (D_1 - C_1A_1^{-1}B_1)\phi_1(u_1) && (4.116) \\ &= C_1 z_1 + G_1(0)(v_1 + \phi_1(u_1^*)) && (4.117) \\ &= C_1 z_1 + G_1(0)v_1 + G_1(0)\phi_1(u_1^*) && (4.118) \end{aligned}$$

Defining $w_1 = y_1 - G_1(0)\phi_1(u_1^*)$ we have that

$$w_1 = C_1 z_1 + G_1(0) v_1 \tag{4.119}$$

where again employing a similar definition for the second system we have that

$$\begin{aligned} y_2 &= C_2 z_2 + G_2(0) v_2 + G_2(0)\phi_2(u_2^*) && (4.120)\\ w_2 &= y_2 - G_2(0)\phi_2(u_2^*) && (4.121)\\ w_2 &= C_2 z_2 + G_2(0) v_2 && (4.122) \end{aligned}$$

Now, the integral control equation will become, with $\eta_1 = \phi_1^{\nabla}(u_1)$

$$\begin{aligned} \dot{v}_1 &= \phi_1^{\nabla}(u_1)\dot{u}_1 && (4.123)\\ &= \eta_1(k[r-y] - k_c[r-y2]) && (4.124)\\ &= \eta_1(k[r - C_1 z_1 - G_1(0)v_1 - G_1(0)\phi_1(u_1^*)] - k_c[r - C_2 z_2 - G_2(0)v_2 - G_2(0)\phi_2(u_2^*)) \\ &= \eta_1(-k[C_1 z_1 + G_1(0)v_1] + k_c[C_2 z_2 + G_2(0)v_2]) && (4.125)\\ &= -\eta_1 k w_1 + \eta_1 k_c w_2 && (4.126) \end{aligned}$$

In the exact same fashion, the integral control equation can be redefined for the second system as

$$\dot{v}_2 = -\eta_2 k w_2 + \eta_2 k_c w_1 \tag{4.127}$$

Assembling Eq.'s 4.112, 4.113, 4.119, 4.122, 4.126 and 4.127 we have that

$$\dot{z}_1 = A_1 z_1 + A_1^{-1} B_1 \dot{v}_1 \tag{4.128}$$

$$\dot{z}_2 = A_2 z_2 + A_2^{-1} B_2 \dot{v}_2 \tag{4.129}$$

$$w_1 = C_1 z_1 + G_1(0) v_1 \tag{4.130}$$

$$w_2 = C_2 z_2 + G_2(0) v_2 \tag{4.131}$$

$$\dot{v}_1 = -\eta_1 k w_1 + \eta_1 k_c w_2 \tag{4.132}$$

$$\dot{v}_2 = -\eta_2 k w_2 + \eta_2 k_c w_1 \tag{4.133}$$

which can be written in matrix form as

$$\begin{bmatrix} \dot{z}_1 \\ \dot{z}_2 \\ \dot{v}_1 \\ \dot{v}_2 \end{bmatrix} = \begin{bmatrix} A_1 & 0 & 0 & 0 \\ 0 & A_2 & 0 & 0 \\ 0 & 0 & 0 & 0 \\ 0 & 0 & 0 & 0 \end{bmatrix} \begin{bmatrix} z_1 \\ z_2 \\ v_1 \\ v_2 \end{bmatrix} + \begin{bmatrix} A_1^{-1} B_1 & 0 \\ 0 & A_2^{-1} B_2 \\ 1 & 0 \\ 0 & 1 \end{bmatrix} \begin{bmatrix} \dot{v}_1 \\ \dot{v}_2 \end{bmatrix} \tag{4.134}$$

$$\begin{bmatrix} w_1 \\ w_2 \end{bmatrix} = \begin{bmatrix} C_1 & 0 \\ 0 & C_2 \end{bmatrix} \begin{bmatrix} z_1 \\ z_2 \end{bmatrix} + \begin{bmatrix} G_1(0) & 0 \\ 0 & G_2(0) \end{bmatrix} \begin{bmatrix} v_1 \\ v_2 \end{bmatrix} \tag{4.135}$$

$$\begin{bmatrix} \dot{v}_1 \\ \dot{v}_2 \end{bmatrix} = -\begin{bmatrix} \eta_1 & 0 \\ 0 & \eta_2 \end{bmatrix} \begin{bmatrix} k & -k_c \\ -k_c & k \end{bmatrix} \begin{bmatrix} w_1 \\ w_2 \end{bmatrix} \tag{4.136}$$

which is equivalent to

$$\begin{bmatrix} \dot{z}_1 \\ \dot{z}_2 \\ \dot{v}_1 \\ \dot{v}_2 \end{bmatrix} = \begin{bmatrix} A_1 & 0 & 0 & 0 \\ 0 & A_2 & 0 & 0 \\ 0 & 0 & 0 & 0 \\ 0 & 0 & 0 & 0 \end{bmatrix} \begin{bmatrix} z_1 \\ z_2 \\ v_1 \\ v_2 \end{bmatrix} - \begin{bmatrix} A_1^{-1} B_1 & 0 \\ 0 & A_2^{-1} B_2 \\ 1 & 0 \\ 0 & 1 \end{bmatrix} \begin{bmatrix} \eta_1 & 0 \\ 0 & \eta_2 \end{bmatrix} \begin{bmatrix} k_1 & -k_c \\ -k_c & k_2 \end{bmatrix} \begin{bmatrix} w_1 \\ w_2 \end{bmatrix} \tag{4.137}$$

$$\begin{bmatrix} w_1 \\ w_2 \end{bmatrix} = \begin{bmatrix} C_1 & 0 \\ 0 & C_2 \end{bmatrix} \begin{bmatrix} z_1 \\ z_2 \end{bmatrix} + \begin{bmatrix} G_1(0) & 0 \\ 0 & G_2(0) \end{bmatrix} \begin{bmatrix} v_1 \\ v_2 \end{bmatrix} \tag{4.138}$$

In a simpler form, we have that

$$\begin{bmatrix} \dot{z} \\ \dot{v} \end{bmatrix} = \begin{bmatrix} A & 0 \\ 0 & 0 \end{bmatrix} - \begin{bmatrix} A^{-1}B \\ I \end{bmatrix} \eta K w \tag{4.139}$$

$$w = Cz + Gv \tag{4.140}$$

where the obvious definitions have been made.

Taking the Lyapunov function candidate as $V = z^T P z + v^T G v$, it's time derivative is given as

$$\dot{V} = \dot{z}^T P z + z^T P \dot{z} + \dot{v}^T G v + v^T G \dot{v} \tag{4.141}$$

$$= (Az + A^{-1}B\dot{v})^T P z + z^T P (Az + A^{-1}B\dot{v}) + 2\dot{v}^T G v \tag{4.142}$$

$$= z^T A^T P z + \dot{v}(A^{-1}B)^T P z + z^T P A z + z^T P A^{-1} B \dot{v} + 2\dot{v}^T G v \tag{4.143}$$

$$= z^T (A^T P + PA) z + 2 z^T P A^{-1} B \dot{v} + 2\dot{v}^T G v \tag{4.144}$$

with $Gv = w - Cz$ we have

$$\dot{V} = z^T (A^T P + PA) z + 2 z^T P A^{-1} B \dot{v} + 2\dot{v}^T (w - Cz) \tag{4.145}$$

$$= z^T (A^T P + PA) z + 2 z^T P A^{-1} B \dot{v} + 2\dot{v}^T w - 2\dot{v}^T C z \tag{4.146}$$

$$= z^T (A^T P + PA) z + 2 z^T (P A^{-1} B - C^T) \dot{v} + 2\dot{v}^T w \tag{4.147}$$

$$= \begin{bmatrix} z \\ v \end{bmatrix} \begin{bmatrix} A^T P + PA & PA^{-1}B - C^T \\ (A^{-1}B)^T P - C & -2\Delta \end{bmatrix} \begin{bmatrix} z \\ v \end{bmatrix} + 2\dot{v}^T \Delta \dot{v} + 2\dot{v}^T w$$

with $\dot{v} = -\eta K w$. There exists a $Q < 0$ (see [134]) such that

$$Q = \begin{bmatrix} A^T P + PA & PA^{-1}B - C^T \\ (A^{-1}B)^T P - C & -2\Delta \end{bmatrix} \tag{4.148}$$

where

$$P = P^T = \begin{bmatrix} P_1 & 0 \\ 0 & P_2 \end{bmatrix} > 0 \tag{4.149}$$

And we can now write

$$\begin{aligned} \dot{V} &= \begin{bmatrix} z \\ v \end{bmatrix} Q \begin{bmatrix} z \\ v \end{bmatrix} + 2\dot{v}^T \Delta \dot{v} + 2\dot{v}^T w & (4.150) \\ \dot{V} &= \begin{bmatrix} z \\ v \end{bmatrix} Q \begin{bmatrix} z \\ v \end{bmatrix} + 2w^T K^T \eta^T \Delta \eta K w - 2w^T K^T \eta^T w & (4.151) \\ &= \begin{bmatrix} z \\ v \end{bmatrix} Q \begin{bmatrix} z \\ v \end{bmatrix} + 2w^T K^T \eta^T (\Delta \eta K - I) w & (4.152) \\ &= \begin{bmatrix} z \\ v \end{bmatrix} Q \begin{bmatrix} z \\ v \end{bmatrix} - 2w^T K^T \eta^T (I - \Delta \eta K) w & (4.153) \end{aligned}$$

Here, $K = K^T > 0$, $\eta = \eta^T \geq 0$ since η is non-decreasing, and $\Delta = \Delta^T > 0$. However, in the general case, the matrices η and K do not commute (ie. $\eta K \neq K\eta$), and positive semi-definiteness of the quadratic form cannot be easily shown due to the asymmetry of the term $\Gamma = K^T \eta^T (I - \Delta \eta K)$. In general, in synchronization control, it is assumed that the dynamical systems are identical [138–140]. In this case, if the systems are identical, the proof is much simpler. This condition now holds for properly chosen k and k_c, with

$$\xi = I - \Delta \eta K = \begin{bmatrix} 1 - \frac{\eta k}{\tilde{k}\lambda} & \frac{\eta k_c}{\tilde{k}\lambda} \\ \frac{\eta k_c}{\tilde{k}\lambda} & 1 - \frac{\eta k}{\tilde{k}\lambda} \end{bmatrix} > 0 \tag{4.154}$$

where $\xi = \xi^T > 0$, and employing the fact that $K = K^T > 0$ and $\eta = \eta^T \geq 0$ yields that $\Gamma = \Gamma^T \geq 0$ since both the nonlinearities contained in η are equivalent.

However, assuming the nonlinearities of two real physical systems are equivalent is a rather large assumption. In the general case, we have that $\eta_1 \neq \eta_2$, hence

$\Gamma \neq \Gamma^T$. In this case, the quadratic form given by $2w^T K^T \eta^T (I - \Delta\eta K)w$ is positive semidefinite if and only if the symmetric part of Γ given by $\Gamma_{sym} = \frac{1}{2}(\Gamma + \Gamma^T)$ is positive semidefinite. This condition is difficult to verify analytically, and typically must be solved numerically. For proper choices of k and k_c, it can be shown that Γ_{sym} is positive semidefinite, hence

$$\dot{V} = \begin{bmatrix} z \\ v \end{bmatrix} Q \begin{bmatrix} z \\ v \end{bmatrix} - 2w^T K^T \eta^T (I - \Delta\eta K)w \tag{4.155}$$

$$\dot{V} \leq \begin{bmatrix} z \\ v \end{bmatrix} Q \begin{bmatrix} z \\ v \end{bmatrix} \tag{4.156}$$

$$\dot{V} < 0 \tag{4.157}$$

4.5.2 Output Feedback Synchronization Experiments

To run the HITL simulations, an appropriate model must first be constructed. As such, the frequency response of the piezoelectric actuator is obtained and then approximated by a fourth order transfer function as

$$G_H(s) = \frac{\beta_0}{s^4 + \alpha_3 s^3 + \alpha_2 s^2 + \alpha_1 s + \alpha_0} \tag{4.158}$$

The static gain of the transfer function is then decreased, and the resonance of the actuators portion of the response is shifted to approximately 5272 Hz. The rolloff of the amplifier is then also modified slightly to 1000 Hz simply so that the response of the model is not the same as that of the actuator. A nonlinear model was identified from experimental data, with the identification structure as shown

in Fig. 4.26. This model includes the creep, or slow drift of the actuator, in the system identification problem. Creep was not considered in the analysis of the stability problem, as the creep response is much slower than that of the dynamical model. The nonlinear model was then perturbed from its nominal values such that the nonlinearity has a different response than that of the experimental system.

Table 4.3 Linear and nonlinear parameters of simulation model

Parameter	0	1	2	3	4	5
a	0	0.1667	0.3333	0.5	0.6667	0.8333
w_h	0.9442	0.0207	0.0404	0.0229	0.0601	0.0535
d	0	1.56	1.75	1.89	1.95	
w_s	0.9136	0.0002	0.0027	0.0036	0.0209	
w_c		0.1655	0.1020	0.0477	0.0237	0.1159
α	4.333e+16	1.4084e+13	1.2297e+9	1.9941e+4		
β	3.466e+16					

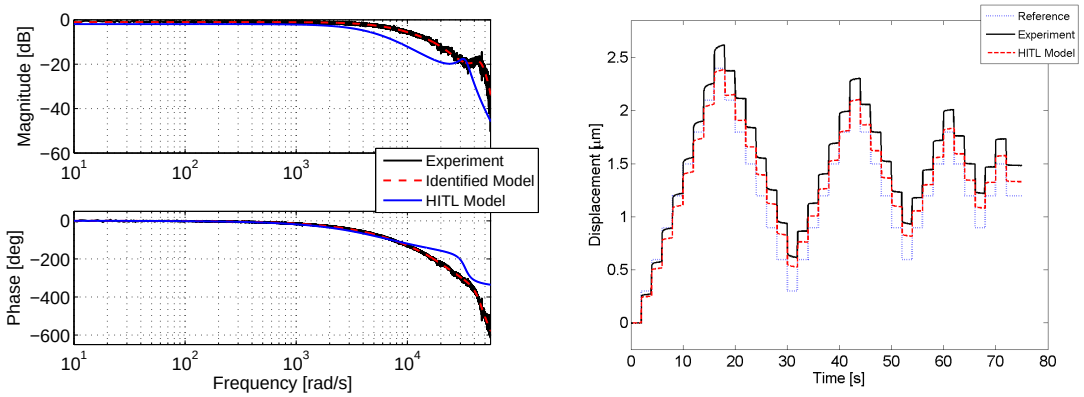

(a) Frequency response (b) Nonlinear response

Fig. 4.25 Comparison of HITL simulation model to experimental system

With the HITL simulation model established, the HITL experiments can now

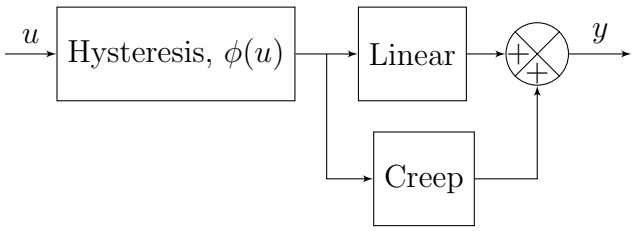

Fig. 4.26 Structure for system identification

be conducted. In open loop, the response of the actuator and the HITL model to a desired constant reference is shown in Fig. 4.27. The maximal regulating gains gain now be calculated from Eq. 4.105 and 4.106 as $k_{1_*} = \frac{1}{2.5989\times10^{-4}} = 3.8478\times10^3$ and $k_{2_*} = \frac{1}{2.2898\times10^{-4}} = 4.3671\times10^3$. We can then calculate $\lambda_1 = 1.0745$, and $\lambda_2 = 1.5803$. From this, we can define

$$\bar{K} = \Lambda^{-1}K_* = \begin{bmatrix} 3.5810\times10^3 & 0 \\ 0 & 2.7634\times10^3 \end{bmatrix} \tag{4.159}$$

For selection of the synchronization gain matrix, $K < \tilde{K} < \bar{K}$, it should be noted that when $\lambda_{min}(K)$ is small (where λ_{min} denotes the smallest eigenvalue of K, hence large k_c for fixed k), numerical issues can be encountered in implementation.

To perform the HITL experiments, three gain configurations are chosen for comparison in tracking a 2μm constant reference value: (a) k=1000, $k_c = 250$, (b) k=1000, $k_c = 500$, and (c) k=1000, $k_c = 750$. It can be seen that these gains are all well within the maximum stability limits of the uncoupled systems, and can be shown to satisfy $\Gamma_{sym} \geq 0$. Case (a) is shown in Fig. 4.28(a) and 4.28(b),

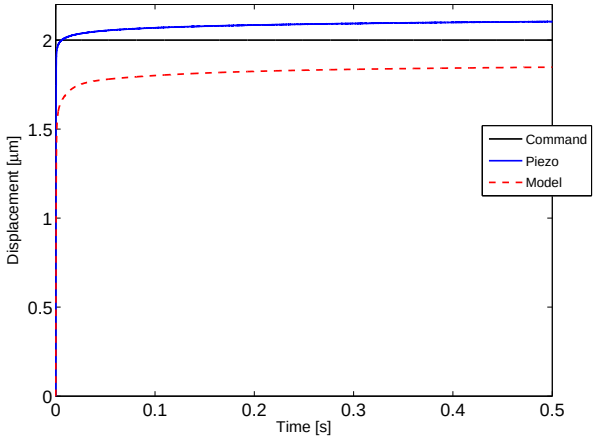

Fig. 4.27 Open loop response of experimental system and HITL model

where it can be seen that the actuators move together to the reference, with a large overshoot, and are tied together by the synchronization control, albeit not very tightly during the overshoot portion of their response. In Case (b), seen in Fig. 4.28(c) and 4.28(d), the synchronization gain is increased, which has the effect of reducing the overshoot, although slowing the system response, while more tightly synchronizing the actuators together. Case (c), shown in Fig. 4.28(e) and 4.28(f), once again uses a higher coupling gain, and once again, the overshoot is reduced, and the actuators are more closely held together, although at the expense of a slower convergence rate. This is due to the effect of the synchronization slowing down the speed of response of the system as it can be seen that in Case (c), the effective gain for $\dot{u}_1$ and $\dot{u}_2$ will be smaller due to the stronger synchronization of the systems caused by the larger coupling gains k_c. As the coupling gain k_c is increased, it can

also be seen that the noise becomes coupled across the systems. This is desirable if a high enough sample rate can be used, and the response can be filtered in the loop, such that any disturbances can be coupled across the systems such that they move together, with a very small phase lag, even in the presence of disturbances.

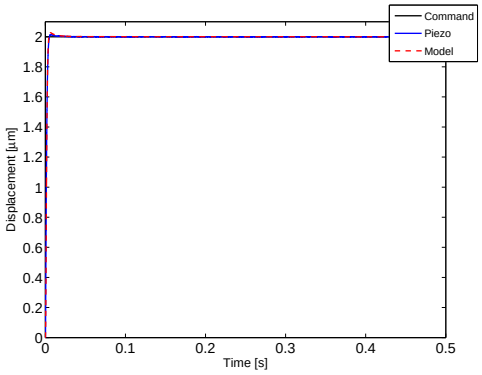

(a) $k = 1000$, $k_c = 250$

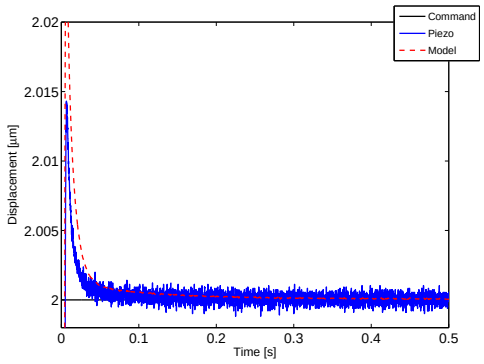

(b) $k = 1000$, $k_c = 250$, magnified

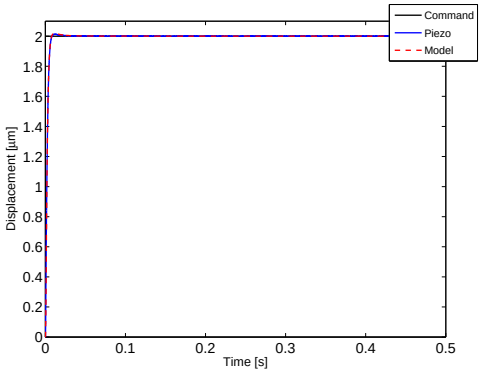

(c) $k = 1000$, $k_c = 500$

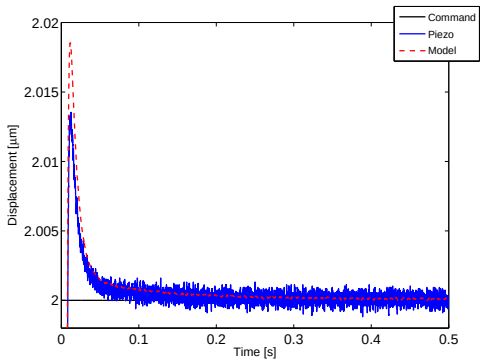

(d) $k = 1000$, $k_c = 500$, magnified

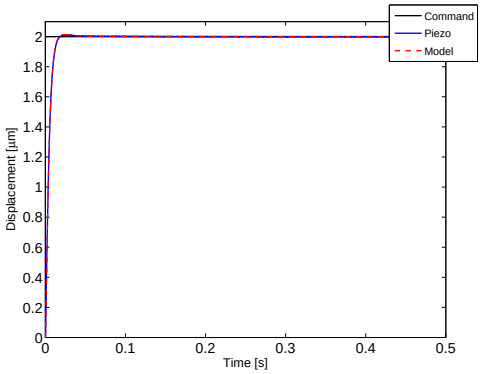

(e) $k = 1000$, $k_c = 750$

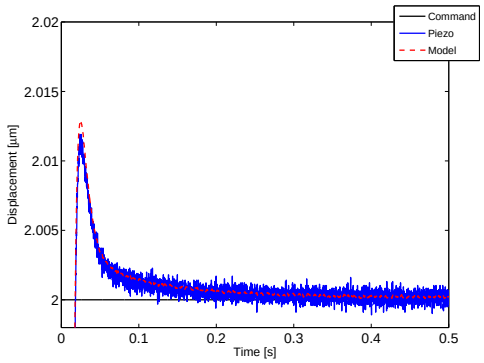

(f) $k = 1000$, $k_c = 750$, magnified

Fig. 4.28 HITL synchronization control results

5 Conclusions and Future Work

In this work, the use of smart materials for three applications was considered: flatness control of a membrane structure via boundary tensions supplied by shape memory alloys, piezoelectric actuators for vibration control, and control of a piezoelectric actuator/stage for nanopositioning of instrumentation.

In Chapter 2, the control of membrane structures by shape memory alloys located along the boundary of the membrane was studied. First, a genetic algorithm controller was developed and tested experimentally for minimization of the flatness of the membrane structure with the primary objective being to remove thermally-induced wrinkles. The proposed new genetic algorithm controller with online objective reweighting was then combined with two previously developed genetic algorithms, the standard and adaptive genetic algorithm. The consideration of optimal tension combinations was introduced when convergence in the membrane flatness was judged to be occurring, as their appears to be a rather broad plateau in the solution space. This was achieved by reweighting the objective function to

preferentially keep small tension combinations that produce very similar flatness values, hence the power required to actuate the SMAs can be reduced. The new controllers both performed well in reducing the membrane flatness and the total tension required. In the following section, the SMA controllers were revised to be pulse width modulated, proportional integral controllers, with duty cycling. This design was implemented to allow higher currents to the actuators, and hence faster simultaneous control of all twenty actuators while ensuring their safety. Three different types of PWM were implemented with duty cycling for the proportional integral controller and shown to perform quite well for simultaneous control of all twenty actuators. The revised SMA controllers were then used for maintaining the membrane shape under time-varying thermal loading by use of a simple PI controller.

Then, in Chapter 3, the dynamic modeling of a flexible manipulator was performed using the finite element method to include the effect of the piezoelectric sensor/actuator pair through Euler-Bernoulli beam theory. Input shaping was then used in combination with a proportional-derivative controller to slew the flexible beam in order to minimize the induced vibration during the maneuver. The residual vibration due to parameter uncertainty was then suppressed by the PZT actuator with the proposed multi-mode adaptive positive position feedback. An adaptation law based on the recursive least squares method was developed to update the

system's first two natural frequencies, which were then used by the multi-mode positive position feedback controller to suppress the residual vibrations. Simulations and several experimental scenarios were then run to show the effectiveness of the combination of input shaping and multi-mode adaptive positive position feedback control. This method offers advantages in vibration suppression over either of these control methods alone, particularly for systems where there are large frequency uncertainties. Then, as an alternative to the adaptive PPF, an offline system identification technique and controller optimization method were developed. First, the dynamic model of the flexible manipulator was augmented to include the effect of the feedthrough in the system due to the collocated nature of the sensor/actuator pair. Then, a system identification process, based upon an iterative genetic algorithm that condenses its search space at each iteration, was outlined for identifying a resonant system with feedthrough. This system identification technique was shown to accurately identify the transfer function of a flexible manipulator from both simulated and experimental data. A two-mode positive position feedback controller was then designed to suppress the first two modes of vibration of the flexible manipulator. To this end, the same genetic algorithm was used to minimize the H_∞-norm of the closed loop system and choose the PPF control parameters that guaranteed stability while resulting in optimal vibration suppression. Simulations and experiments were run through which the parameters chosen by the

genetic algorithm optimization were shown to result in very good suppression of the vibrations in the manipulator.

Finally, in Chapter 4, the use of piezoelectric actuators for nanopositioning of instrumentation was discussed. A linear transfer function model and a nonlinear phenomenological model based upon the modified Prandtl-Ishlinskii operator were developed for the system. To start, a state feedback integral plus double integral synchronization controller was developed for HITL simulations of a parallel three-axis positioning platform. Under nominally linear behaviour, the control was shown to be asymptotically stable for tracking of step inputs, and bounded-input-bounded-output stable for tracking of a class of waveforms. Next, an output feedback integral control law was examined for the piezoelectric actuator with explicit characterization of its hysteresis as an input nonlinearity to a linear state space system. From experiments, the piezoelectric actuator was identified and modeled as a series connection of the hysteresis nonlinearity and the linear dynamical model. From this, conditions on the maximum integral gain are derived such that the system is asymptotically stable. Finally, this work was extended to the case of output feedback integral synchronization control for systems with input nonlinearities. Global asymptotic stability conditions were derived, and then applied for HITL simulations of the controller. For this, a perturbed model of the piezoelectric actuator is used along with the actual system for the experiments, and

good performance of the synchronization law is shown.

5.1 Future Work

For the membrane, there is still a great deal of work to be done. To start, new finite elements allow much faster analysis of membrane structures than the S4R5 elements permit. This would be particularly useful for optimization of the membrane structure, in particular the size and depth of the elliptical boundary cuts. While the membrane must remain rectangular in nature for a SAR antenna, a more symmetrical design would be useful, while still giving respect to the required redundancy of the boundary control elements. One of the biggest steps forward for membrane technologies would be the capability to infer the state of the membrane from the state of its actuators. While quite difficult analytically, this would allow the actuators along the boundary to detect and correct the surface deviations of the membrane, as clearly the current vision based technique is not applicable in space. This would require extremely accurate models of the SMAs themselves in order to allow changes in the membrane to be uniquely detected from the SMA state. Clearly, these large membrane structures will also require deployment mechanisms, and more advanced support structures (as opposed to the current aluminum frame). Among these, the advances in inflatable structures, and shape memory polymer composites appear to be promising for the application of membrane technologies in

space.

A great deal of research has already been conducted on the single-link flexible manipulator and on flexible manipulators in general. With regards to manipulators with piezoelectric sensors and actuators, system level designs are still required to be performed such that the advantages of these systems make them truly desirable in space applications. For the flexible manipulator, a possible future research direction is in the consideration of the effect of hysteresis in the piezoelectric actuators for vibration control. An inverted model of the hysteresis could be used for open loop tracking of the applied control signal. This would ensure that the actuator follows the desired vibration control signal very closely. An alternative would be to implement a closed loop control method for tracking of the actuator directly, while the vibration control scheme runs in an outer control loop. One of the most interesting future areas of application are in composite structures, where piezoelectric fibres are being implanted into the structure to create strong and stiff structures with a large control authority.

The piezoelectric stack actuator has a number of future applications in nanopositioning. The work conducted here gives a framework for more complex controllers, and the first step is to integrate an integral resonant controller to the current integral controller. The resonant control would allow much higher integral control gains to be used as it will suppress the resonant mode of the actuator that becomes

excited due to the integral control action alone. This can then be extended to more complex nonlinear integral controllers. It also appears as though a less conservative condition for the stability of integral control for systems with hysteresis could be derived through a Popov-type argument. A future application of interest for the piezoelectric actuators is in the simultaneous nanopositioning and vibration control of six degree-of-freedom Stewart platforms (where they are already used for vibration control). The integral type synchronization control could be extended to this platform such that all six actuators motions remain coupled even in the presence of vibration disturbances. This would also allow a steering of instrumentation mounted on the top of the platform through a very fine range of motion.

A Complete List of Publications

Journal

[1] **R. Orszulik**, J. Shan. "Experimental Study on Active Vibration Control using Genetic Algorithm-Based System Identification and Optimized Positive Position Feedback," *Smart Materials and Structures*, 21(12), 2012, pp. 125014.

[2] **R. Orszulik**, J. Shan. "Fuzzy Logic Active Flatness Control of a Space Membrane Structure," *Acta Astronautica*, 77, 2012, pp. 68–76.

[3] **R. Orszulik**, J. Shan. "Active vibration control using genetic algorithm-based system identification and positive position feedback," *Smart Materials and Structures*, 21(5), 2012, pp. 055002.

[4] **R. Orszulik**, J. Shan. "Vibration Control Using Input Shaping and Adaptive Positive Position Feedback," *AIAA Journal of Guidance, Control and Dynamics*, 34(4), 2011, pp. 1031–1044.

[5] **R. Orszulik**, J. Shan. "Membrane Structure Active Flatness Control Using Genetic Algorithm with Online Objective Reweighting," *Acta Astronautica*, 68(11–12), 2011, pp. 2012-2024.

Conference

[1] **R. Orszulik**, J. Shan. "Shape Control of a Membrane Structure by Shape Memory Alloys." *63rd International Astronautical Congress*. Naples, Italy. October 1-5, 2012.

[2] J. Shan, **R. Orszulik**, M. Girin, G. Sinnathamby. "Flatness Measurement and Active Control for Membrane Structure." *IEEE International Conference on Mechatronics and Automation*. Chengdu, China. August 6-8, 2012.

[3] **R. Orszulik**, J. Shan. "A Simple PI Controller for Active Flatness and Tracking Control of a Space Membrane Structure." *AIAA Structures, Structural Dynamics and Materials Conference*. Honolulu, HI. April 23-26, 2012.

[4] **R. Orszulik**, J. Shan. "Finite Element Analysis of a Wrinkled Rectangular Membrane with Elliptical Boundary Cuts." *AIAA Structures, Structural Dynamics and Materials Conference*. Honolulu, HI. April 23-26, 2012.

[5] **R. Orszulik**, J. Shan. "Experimental Study on Combining a Simple Input Shaper and Adaptive Positive Position Feedback Control." *AIAA Guidance, Navigation and Control Conference*. Portland, OR. August 5-8, 2011.

[6] **R. Orszulik**, J. Shan. "Active Flatness Fuzzy Logic Control of Space Membrane Structure." *AIAA Guidance, Navigation and Control Conference*. Portland, OR. August 5-8, 2011.

[7] **R. Orszulik**, J. Shan. "Multi-Mode Adaptive Positive Position Feedback: An Experimental Study." *American Control Conference*. San Franciso, CA. June 29 - July 1, 2011.

[8] **R. Orszulik**, J. Shan. "Vibration Suppression of Flexible Manipulator by Combining Modified Input Shaping and Adaptive Positive Position Feedback Control." *AIAA Guidance, Navigation and Control Conference*. Toronto, ON. August 2-5, 2010.

[9] **R. Orszulik**, J. Shan. "Vibration Suppression using Adaptive Positive Position Feedback: An Experimental Study." *Proceedings of The Canadian Society for Mechanical Engineering Forum 2010*. Victoria, BC. June 7-9, 2010.

[10] M. Stachowsky, **R. Orszulik**, J. Shan. "Adaptive Input-Shaping for a Single-Link Flexible Manipulator." *Proceedings of The Canadian Society for Mechanical Engineering Forum 2010*. Victoria, BC. June 7-9, 2010.

[11] **R. Orszulik**, J. Shan. "Active Vibration Control using Adaptive Positive Position Feedback." *AIAA Guidance, Navigation and Control Conference.* Chicago, IL. August 10-13, 2009.

Bibliography

[1] Akella, P., Chen, X., Cheng, W., Hughes, D., and Wen, J. T., "Modeling and control of smart structures with bonded piezoelectric sensors and actuators," *Smart Materials and Structures*, Vol. 3, No. 3, 1994, pp. 344–353.

[2] Crawley, E. F. and de Luis, J., "Use of piezoelectric actuators as elements of intelligent structures," *AIAA Journal*, Vol. 25, No. 10, 1987, pp. 1373–1385.

[3] TZOU, H. S., LEE, H.-J., and ARNOLD, S. M., "Smart Materials, Precision Sensors/Actuators, Smart Structures, and Structronic Systems," *Mechanics of Advanced Materials and Structures*, Vol. 11, No. 4-5, 2004, pp. 367–393.

[4] Guay, P., Bousquet, P. W., Courau, E., and Mercier, F., "CASTOR damping experiment in-flight results," 2001.

[5] Hanieh, A., Preumont, A., and Loix, N., "Piezoelectric Stewart platform for general purpose active damping interface and precision control," *Proceedings*

of the 9th European Space Mechanisms and Tribology Symposium, 2001, pp. 331–334.

[6] Hanieh, A., *Active Isolation and Damping of Vibrations via Stewart Platform*, Ph.D. thesis, Universite Libre De Bruxelles, April 2003.

[7] Chen, H., Bishop, R., and Agrawal, B., "Payload Pointing and Active Vibration Isolation Using Hexapod Platforms," *44th AIAA/ASME/ASCE/AHS Structures, Structural Dynamics, and Materials Conference*, AIAA, Norfolk, VA, Apr. 7-10 2003, AIAA-2003-1643.

[8] Le Letty, R., Claeyssen, F., Lhermet, N., and Bouchilloux, P., "New amplified piezoelectric actuator for precision positioning and active damping," 1997.

[9] Park, G., Kim, M.-H., and Inman, D. J., "Integration of Smart Materials into Dynamics and Control of Inflatable Space Structures," *Journal of Intelligent Material Systems and Structures*, Vol. 12, No. 6, 2001, pp. 423–433.

[10] Sherrit, S., "Smart material/actuator needs in extreme environments in space," 2005.

[11] Janker, P., Claeyssen, F., Grohmann, B., Christmann, M., Lorkowski, T., LeLetty, R., sosniki, O., and Pages, A., "New Actuators for Aircraft and

Space Applications," *ACTUATOR 2008, 11th International Conference on New Actuators*.

[12] Le Letty, R., Lhermet, N., Patient, G., Claeyssen, F., and Lang, M., "Valves Based on Amplified Piezoelectric Actuators," *4th International Spacecraft Propulsion Conference*, Vol. 555 of *ESA Special Publication*, Oct. 2004.

[13] Peffer, A., Denoyer, K., Fosness, E., and Sciulli, D., "Development and transition of low-shock spacecraft release devices," *Aerospace Conference Proceedings, 2000 IEEE*, Vol. 4, 2000, pp. 277–284 vol.4.

[14] Willey, C., Huettl, B., and Hill, S., "Design and development of a miniature mechanisms tool-kit for micro spacecraft," May 2001.

[15] Akhras, G., "Smart Materials and Smart Systems for the Future," *Canadian Military Journal*, Vol. 1, No. 3, 2000, pp. 25–32.

[16] Godard, O. J., Lagoudas, M. Z., and Lagoudas, D. C., "Design of space systems using shape memory alloys," 2003.

[17] Saadat, S., Salichs, J., Noori, M., Hou, Z., Davoodi, H., Bar-on, I., Suzuki, Y., and Masuda, A., "An overview of vibration and seismic applications of NiTi shape memory alloy," *Smart Materials and Structures*, Vol. 11, No. 2, 2002, pp. 218.

[18] Kumar, P. and Lagoudas, D., "Introduction to Shape Memory Alloys," *Shape Memory Alloys*, Vol. 1, Springer US, 2008, pp. 1–51.

[19] Carpenter, B. and Lyons, J., "EO-1 Technology Validation Report: Lightweight Flexible Solar Array Experiment," Tech. rep., NASA Goddard Space Flight Center, Greenbelt, MD, August 2001.

[20] Freeman, J., Rudder, C., and Thomas, P., "MightySat II: On-orbit Lab Bench for Air Force Research Laboratory," *Proceedings of the 14th Annual AIAA/USU Conference on Small Satellites*, August 2000, SSC00-I-2.

[21] Moheimani, S. O. R. and Fleming, A. J., *Piezoelectric Transducers for Vibration Control and Damping*, Springer-Verlag London Ltd., Germany, 2006, pp. 9–26.

[22] Jordan, T. L. and Ounaies, Z., "Piezoelectric Ceramics Characterization," Tech. rep., ICASE: NASA Langley Research Center, 2001.

[23] Preumont, A., *Vibration Control of Active Structures: An Introduction*, Kluwer Academic Publishers, Norwell, Massachusetts, 2007, pp. 27, 40–45, 101–103.

[24] "IEEE Standard on Piezoelectricity," *ANSI/IEEE Std 176-1987*, 1988.

[25] "Piezoelectric systems," *Mechatronics*, Vol. 136, Springer Netherlands, 2006, pp. 95–130.

[26] Hodgson, D., Wu, M., and Biermann, R., *Shape Memory Alloys*, Metals Handbook, Vol. 2, 10th Edition, Properties and Selection. ASM International, pp. 897-902, 1991.

[27] Hartl, D. J. and Lagoudas, D. C., "Aerospace applications of shape memory alloys," *Proceedings of the Institution of Mechanical Engineers, Part G: Journal of Aerospace Engineering*, Vol. 221, No. 4, 2007, pp. 535–552.

[28] Wei, Z., Sandstrorm, R., and Miyazaki, S., "Shape-memory materials and hybrid composites for smart systems: Part I Shape-memory materials," *Journal of Materials Science*, Vol. 33, No. 15, 1998, pp. 3743–3762.

[29] Tanaka, K. and Nagaki, S., "A thermomechanical description of materials with internal variables in the process of phase transitions," *Ingenieur-Archiv*, Vol. 51, No. 5, 1982, pp. 287–299.

[30] Liang, C. and Rogers, C., "One-Dimensional Thermomechanical Constitutive Relations for Shape Memory Materials," *Journal of Intelligent Material Systems and Structures*, Vol. 1, No. 2, 1990, pp. 207–234.

[31] Brinson, L., "One-Dimensional Constitutive Behavior of Shape Memory Alloys: Thermomechanical Derivation with Non-Constant Material Functions and Redefined Martensite Internal Variable," *Journal of Intelligent Material Systems and Structures*, Vol. 4, No. 2, 1993, pp. 229–242.

[32] Boyd, J. and Lagoudas, D., "A Thermodynamic Constitutive Model for the Shape Memory Materials. Part I. The Monolithic Shape Memory Alloys," *International Journal of Plasticity*, Vol. 12, 1996, pp. 805842.

[33] Peng, F., Jiang, X., Hu, Y., and Ng, A., "Actuation Precision Control of SMA Actuators used for Shape Control of Inflatable SAR Antenna," *Acta Astronautica*, Vol. 63, 2008, pp. 578–585.

[34] Talley, C., Clayton, W., Gierow, P., Laue, G., McGee, J., and Moore, J., "Advanced membrane materials for improved solar sail capabilities," *43rd AIAA/ASME/ASCE/AHS/ASC Structures, Structural Dynamics, and Materials Conference*, AIAA, Denver, CO, Apr. 22-25 2002, AIAA-2002-1561.

[35] Wong, Y., Pellegrino, S., and Park, K., "Prediction of Winkle Amplitudes in Square Solar Sails," *44th AIAA/ASME/ASCE/AHS/ASC Structures, Structural Dynamics, and Materials Conference*, Norfolk, Virginia, Apr. 7-10 2003, AIAA-2003-1982.

[36] Gaspar, J., Mann, T., Behun, V., Wilkie, W., and Pappa, R., "Development of modal test techniques for validation of a solar sail design," *45th AIAA/ASME/ASCE/AHS/ASC Structures, Structural Dynamics and Materials Conference*, AIAA, Palm Springs, CA, Apr. 19-22 2004, AIAA-2004-1665.

[37] Meinel, A. and Meinel., M., "Inflatable membrane mirrors for optical passband imagery," *Optical Engineering*, Vol. 39, No. 2, 2000, pp. 541–550.

[38] de Blonk, B. J., *Optical-Level Structural Modelling of Membrane Mirrors for Spaceborne Telescopes*, Ph.D. thesis, Massachusetts Institute of Technology, 2003.

[39] Ruggiero, E. and Inman, D., "A comparison between SISO and MIMO modal analysis techniques on a membrane mirror satellite," *Journal of Intelligent Material Systems and Structures*, Vol. 16, No. 3, 2005, pp. 273–282.

[40] Fang, H. and Lou, M., "Analytical characterization of space inflatable structures - an overview," *40th AIAA/ASME/ASCE/AHS/ASC Structures, Structural Dynamics and Materials Conference*, AIAA, St. Louis, MO, Apr. 12-15 1999, AIAA-1999-1272.

[41] Johnston, J. D., "Finite Element Analysis of Wrinkled Membrane Structures for Sunshield Applications," *43rd AIAA/ASME/ASCE/AHS/ASC Struc-*

tures, Structural Dynamics, and Materials Conference, AIAA, Denver, Colorado, Apr. 22-25 2002, AIAA-2002-1456.

[42] Blandino, J. R., Johnston, J. D., and Dharamsi, U. K., "Corner Wrinkling of a Square Membrane Due to Symmetric Mechanical Loads," *Journal of Spacecraft and Rockets*, Vol. 39, No. 5, 2002, pp. 717–724.

[43] Pellegrino, S. and (Editors), S. D. G., *Deployable Structures: Theory and Applications*, Kluwer Academic Publishers, Dordrecht, The Netherlands, 2000.

[44] Meyer, C., Leifer, J., Lopez, B., Jones, D., and Caddell, B., "Zero- and One-g Comparison of Surface Profile in Single-Curved Parabolic Membrane," *Journal of Spacecraft and Rockets*, Vol. 42, No. 6, 2005, pp. 1101–1108.

[45] Ruggiero, E. and Inman, D., "Gossamer Spacecraft: Recent Trends in Design, Analysis, Experimentation, and Control," *Journal of Spacecraft and Rockets*, Vol. 43, No. 1, 2006, pp. 10–24.

[46] (Editor), C. H. M. J., *Gossamer Spacecraft: Membrane and Inflatable Structures Technology for Space Applications*, Progress in Astronautics and Aeronautics, AIAA, 2001.

[47] Wong, Y. W. and Pellegrino, S., "Wrinkled Membranes Part I:Experiments," *Journal of Mechanics of Materials and Structures*, Vol. 1, No. 1, 2006, pp. 1–23.

[48] Wong, Y. and Pellegrino, S., "Computation of Wrinkle Amplitudes in Thin Membrane," *43rd AIAA/ASME/ASCE/AHS/ASC Structures, Structural Dynamics, and Materials Conference*, AIAA, Denver, Colorado, Apr. 22-25 2002, AIAA-2002-1369.

[49] Tessler, A. and Wang, D. S. J., "Effective Modeling and Nonlinear Shell Analysis of Thin Membranes Exhibiting Structural Wrinkling," *Journal of Spacecraft and Rockets*, Vol. 42, No. 2, 2005, pp. 287–298.

[50] Tessler, A. and Sleight, D., "Geometrically Nonlinear Shell Analysis of Wrinkled Thin-Film Membranes with Stress Concentrations," *Journal of Spacecraft and Rockets*, Vol. 44, No. 3, 2007, pp. 582–588.

[51] Wong, Y. W. and Pellegrino, S., "Wrinkled Membranes Part III: Numerical Simulations," *Journal of Mechanics of Materials and Structures*, Vol. 1, No. 1, 2006, pp. 63–95.

[52] Wang, X., Zheng, W., and Hu, Y., "Active Flatness Control of Space Membrane Structures Using Discrete Boundary SMA Actuators," *Proceedings*

of the IEEE/ASME International Conference on Advanced Intelligent Machines, IEEE/ASME, Xi'an, China, July 2-5 2008.

[53] Williams, R., Inman, D., and Austin, E., "Local Effects of PVDF Patches on Inflatable Space-Based Structures," *42nd AIAA/ASME/ASCE/AHS/ASC Structures, Structural Dynamics, and Materials Conference and Exhibit*, AIAA, Seattle, WA, Apr. 16-19 2001.

[54] Miyazaki-Kawasaki, Y. and Furuya, H., "Static Shape Control of Membrane Structures by Piezoelectric Films Bonded Around Creases," *42nd AIAA/ASME/ASCE/AHS/ASC Structures, Structural Dynamics, and Materials Conference and Exhibit*, AIAA, Seattle, WA, Apr. 16-19 2001.

[55] Jenkins, C. and Schur, W., "Gore/Seam Architectures for Gossamer Structures," *AIAA Journal of Spacecraft and Rockets*, Vol. 39, No. 5, 2002, pp. 669–673.

[56] Kumon, M., Mizumoto, I., Iwai, Z., and Indou, A., "Shape Memory Alloy Actuator with Simple Adaptive Control," *Second International Conference on Innovative Computing, Information and Control*, September 2007, p. 429.

[57] Ahn, K. and Nguyen, B., "Position Control of Shape Memory Alloy Actuators Using Self Tuning Fuzzy PID Controller," *International Journal of Control, Automation, and Systems*, Vol. 4, No. 6, 2006, pp. 756–762.

[58] Ma, N., Song, G., and Lee, H., "Position control of shape memory alloy actuators with internal electrical resistance feedback using neural networks," *Smart Materials and Structures*, Vol. 13, No. 4, 2004, pp. 777–783.

[59] Peng, F., Hu, Y., and Ng, A., "Development of GA-Based Control System for Active Shape Control of Inflatable Space Structures," *Proceedings of the IEEE Conference on Control Applications*, IEEE, Toronto, Canada, Aug. 28-31 2005.

[60] Peng, F., Hu, Y., and Ng, A., "Testing of Membrane Space Structure Shape Control Using Genetic Algorithm," *Journal of Spacecraft and Rockets*, Vol. 43, No. 4, 2006, pp. 788–793.

[61] Peng, F., Jiang, X., Hu, Y., and Ng, A., "Application of SMA in Membrane Structure Shape Control," *IEEE Transactions on Aerospace and Electronic Systems*, Vol. 45, No. 1, 2009, pp. 85–93.

[62] Peng, F., Hu, Y., and Ng., A., "Testing of Inflatable-Structure Shape Control using Genetic Algorithms and Neural Networks," *AIAA Journal*, Vol. 45, No. 7, 2007, pp. 1771–1774.

[63] Dickinson, C. and Wen, J., "Feedback Control Using Shape Memory Alloy Actuators," *Journal of Intelligent Material Systems and Structures*, Vol. 9, 1998, pp. 242–250.

[64] Orszulik, R. and Shan, J., "A Simple PI Controller for Active Flatness and Tracking Control of a Space Membrane Structure," *53rd AIAA/ASME/ASCE/AHS/ASC Structures, Structural Dynamics and Materials Conference*, AIAA, Honolulu, HI, Apr. 23-26 2012.

[65] Dwivedy, S. K. and Eberhard, P., "Dynamic analysis of flexible manipulator, a literature review," *Mechanism and Machine Theory*, Vol. 41, No. 7, 2006, pp. 749–777.

[66] Sasiadek, J. Z. and Srinivasan, R., "Dynamic modeling and adaptive control of a single-link flexible manipulator," *Journal of Guidance, Control and Dynamics*, Vol. 12, No. 6, 1989, pp. 838–844.

[67] Jnifene, A. and Andrews, W., "Fuzzy Logic Control of the End-Point Vibration in an Experimental Flexible Beam," *Journal of Vibration and Control*, Vol. 10, No. 4, 2004, pp. 493–506.

[68] Meressi, T. and Paden, B., "Gain scheduled H-infinity controllers for a two link flexible manipulator," *Journal of Guidance, Control and Dynamics*, Vol. 17, No. 3, 1994, pp. 537–543.

[69] Albassam, B. A., "Optimal Near-Minimum-Time Control Design for Flexible Structures," *Journal of Guidance, Control and Dynamics*, Vol. 25, No. 4, 2002, pp. 618–625.

[70] Goh, C. J. and Caughey, T. K., "On the stability problem caused by finite actuator dynamics in the collocated control of large space structure," *International Journal of Control*, Vol. 41, No. 3, 1985, pp. 787–802.

[71] Song, G., Schmidt, S. P., and Agrawal, B. N., "Experimental robustness study of positive position feedback control for active vibration suppression," *Journal of Guidance, Control and Dynamics*, Vol. 25, No. 1, 2002, pp. 179–182.

[72] Fanson, J. L., *An Experimental Investigation of Vibration Suppression in Large Space Structures Using Positive Position Feedback*, Ph.D. thesis, California Institute of Technology, November 1986.

[73] Meyer, J. L., Harrington, W. B., Agrawal, B. N., and Song, G., "Vibration Suppression of a Spacecraft Flexible Appendage using Smart Material," *Smart Materials and Structures*, Vol. 7, No. 1, 1998, pp. 95–104.

[74] Shan, J. J., Liu, H. T., and Sun, D., "Slewing and Vibration Control of a Single-Link Flexible Manipulator by Positive Position Feedback (PPF)," *Mechatronics*, Vol. 15, No. 4, 2005, pp. 487–503.

[75] Singer, N. C. and Seering, W. P., "Preshaping command inputs to reduce system vibration," *ASME Journal of Dynamics Systems, Measurement and Control*, Vol. 112, No. 1, 1990, pp. 76–82.

[76] Smith, O. J. M., "Posicast control of damped oscillatory systems," *Proceedings of the IRE*, Vol. 45, No. 9, 1957, pp. 1249–1255.

[77] Singhose, W., "Command shaping for flexible systems: a review of the first 50 years," *International Journal of Precision Engineering and Manufacturing*, Vol. 10, No. 4, 2009, pp. 153–168.

[78] Banerjee, A. K., "Dynamics and Control of the WISP Shuttle-Antennae System," *Journal of Astronautical Sciences*, Vol. 41, No. 1, 1993, pp. 73–90.

[79] Magee, D. and Book, W. J., "Filtering schilling manipulator commands to prevent flexible structure vibration," *Proceedings of the American Control Conference*, Baltimore, MD, 1994.

[80] Singhose, W., Eloundou, R., and Lawrence, J., "Command Generation for Flexible Systems by Input Shaping and Command Smoothing," *Journal of Guidance, Control and Dynamics*, Vol. 33, No. 6, 2010, pp. 1697–1707.

[81] Khorrami, F., Jain, S., and Tzes, A., "Experimental results on adaptive nonlinear control and input preshaping for multi-link flexible manipulators," *Automatica*, Vol. 31, No. 1, 1995, pp. 83–97.

[82] Banerjee, A. K. and Singhose, W., "Command Shaping in Tracking Control of a Two-Link Flexible Robot," *Journal of Guidance, Control and Dynamics*, Vol. 21, No. 6, 1998, pp. 1012–1015.

[83] Tuttle, T. D. and Seering, W. P., "Vibration reduction in 0-g using input shaping on the MIT middeck active control experiment," *Proceedings of the American Control Conference*, Seattle, WA, 1995.

[84] Singhose, W., Bohlke, K., and Seering, W. P., "Fuel-Efficient Pulse Command Profiles for Flexible Spacecraft," *Journal of Guidance, Control and Dynamics*, Vol. 19, No. 4, 1996, pp. 954–960.

[85] Singhose, W., Derezinski, S., and Singer, N., "Extra-Insensitive Input Shapers for Controlling Flexible Spacecraft," *Journal of Guidance, Control and Dynamics*, Vol. 19, No. 2, 1996, pp. 385–391.

[86] Tuttle, T. D. and Seering, W. P., "Experimental Verification of Vibration Reduction in Flexible Spacecraft Using Input Shaping," *Journal of Guidance, Control and Dynamics*, Vol. 20, No. 4, 1997, pp. 658–664.

[87] Gorinevsky, D. and Vukovich, G., "Nonlinear Input Shaping Control of Flexible Spacecraft Reorientation Maneuver," *Journal of Guidance, Control and Dynamics*, Vol. 21, No. 2, 1998, pp. 264–270.

[88] Hu, Q. and Ma, G., "Vibration Suppression of Flexible Spacecraft During Attitude Maneuvers," *Journal of Guidance, Control and Dynamics*, Vol. 28, No. 2, 2005, pp. 377–380.

[89] Singhose, W., Biediger, E., Okada, H., and Matunaga, S., "Closed-Form Specified-Fuel Commands for On-Off Thrusters," *Journal of Guidance, Control and Dynamics*, Vol. 29, No. 3, 2006, pp. 606–611.

[90] Singhose, W. E., Seering, W. P., and Singer, N. C., "Input shaping for vibration reduction with specified insensitivity to modeling errors," *Proceedings of the Japan/USA Symposium on Flexible Automation*, Boston, MA, 1996, pp. 307–313.

[91] Singhose, W. E., Porter, L. J., and Singer, N. C., "Vibration reduction using multi-hump extra-insensitive input shapers," *Proceedings of the American Control Conference*, Seattle, WA, 1995.

[92] Kojima, H. and Singhose, W., "Adaptive Deflection-Limiting Control for Slewing Flexible Space Structures," *Journal of Guidance, Control and Dynamics*, Vol. 30, No. 1, 2007, pp. 61–67.

[93] Tzes, A. and Yurkovich, S., "An adaptive input shaping control scheme for vibration suppression in slewing flexible structures," *IEEE Transactions on Control Systems Technology*, Vol. 1, No. 2, 1993, pp. 114–121.

[94] Bodson, M., "An Adaptive Algorithm for the Tuning of Two Input Shaping Methods," *Automatica*, Vol. 34, No. 6, 1998, pp. 771–776.

[95] Kwak, M. K., Heo, S., and Jin, G. J., "Adaptive positive position feedback controller design for the vibration suppression of smart structures," *Smart Structures and Materials 2002: Modeling, Signal Processing, and Control*, SPIE, 2002, pp. 246–255.

[96] Baz, A. and Hone, J. T., "Adaptive Control of Flexible Structures Using Modal Positive Position Feedback," *International Journal of Adaptive Control and Signal Processing*, Vol. 11, No. 3, 1997, pp. 231–253.

[97] Rew, K., Han, J., and Lee, I., "Multi-Modal Vibration Control Using Adaptive Positive Position Feedback," *Journal of Intelligent Material Systems and Structures*, Vol. 13, No. 1, 2002, pp. 13–22.

[98] Zibo, Z. and Naghdy, F., "Application of genetic algorithms to system identification," *Evolutionary Computation*, IEEE, November 1995, pp. 777–782.

[99] Pereira, D. and Pinto, J., "Genetic algorithm based system identification and PID tuning for optimum adaptive control," *International Conference on Advanced Intelligent Mechatronics*, IEEE/ASME, July 2005, pp. 801–806.

[100] Duong, V. and Stubberad, A., "System Identification by Genetic Algorithm," *Aerospace Conference Proceedings*, IEEE, March 2002, pp. 2331 – 2338.

[101] Chipperfield, A., Fleming, P., and Fonseca, C., "Genetic Algorithm Tools for Control Systems Engineering," *Adaptive Computing in Engineering Design and Control*, September 1994.

[102] Darus, I. and Tokhi, M., "Genetic algorithm active vibration control of a flexible plate structures," *Proceedings of the 51st Annual Meeting of the ISSS*, International Society for the Systems Sciences, August 2007, pp. 1–12.

[103] Wang, G., "Application of hybrid genetic algorithm to system identification," *Structural Control and Health Monitoring*, Vol. 16, 2009, pp. 125–153.

[104] Kristinnsson, K. and Dumont, G., "System Identification and Control Using Genetic Algorithms," *IEEE Transactions on Systems, Man, and Cybernetics*, Vol. 22, No. 5, 1992, pp. 1033–1046.

[105] Schoen, M., Hoover, R., Chinvorarat, S., and Schoen, G., "System Identification and Robust Controller Design Using Genetic Algorithms for Flexible Space Structures," *Journal of Dynamic Systems, Measurement, and Control*, Vol. 131, No. 3, 2009, pp. 31003–11.

[106] Jin, Z., Yang, Y., and Soh, C., "Application of fuzzy GA for Optimal vibration control of smart cyclindrical shells," *Smart Materials and Structures*, Vol. 14, 2005, pp. 1250–1264.

[107] Moheimani, S., Vautier, B., and Bhikkaji, B., "Experimental Implementation of Extended Multivariable PPF Control on an Active Structure," *IEEE Transactions on Control Systems Technology*, Vol. 14, No. 3, 2006, pp. 443–455.

[108] Kwak, M. and Han, S., "Application of Genetic Algorithm to the Determination of Multiple Positive Position Feedback Controller Gains for Smart Structures," *Part of the SPIE Conference on Mathematics and Control in Smart Structures*, SPIE, March 1998, pp. 637–648.

[109] Kwak, M. and Shin, T., "Real-Time Automatic Tuning of Vibration Controllers for Smart Structures by Genetic Algorithms," *Part of the SPIE Conference on Mathematics and Control in Smart Structures*, SPIE, March 1999, pp. 679–690.

[110] Kwak, M. and Heo, S., "Real-Time Multiple-Parameter Tuning of PPF Controllers for Smart Structures by Genetic Algorithms," *Smart Structures and Materials 2000: Mathematics and Control in Smart Structures*, Vol. 3984, 2000, pp. 279–290.

[111] Junkins, J. L. and Kim, Y., *Introduction to Dynamics and Control of Flexible Structures*, American Institute of Aeronautics and Astronautics, Washington, DC, 1993, pp. 197–213.

[112] Bandyopadhyay, B., Manjunath, T., and Umapathy, M., *Modeling, Control and Implementation of Smart Structures: A FEM – State-Space Approach*, Springer-Verlag Berlin Heidelberg, Berlin, 2007, pp. 23–44.

[113] Inman, D. J., *Vibration with Control*, John Wiley and Sons, Ltd., West Sussex, 2006, pp. 57–71.

[114] Mohamed, Z. and Tokhi, M. O., "Command shaping techniques for vibration control of a flexible robot manipulator," *Mechatronics*, Vol. 14, No. 1, 2004, pp. 69–90.

[115] Ioannou, P. and Fidan, B., *Adaptive Control Tutorial*, Society for Industrial and Applied Mathematics, Philadelphia, 2006, pp. 13–48.

[116] Moheimani, S., "Experimental Verification of the Corrected Transfer Function of a Piezoelectric Laminate Beam," *IEEE Transactions on Control Systems Technology*, Vol. 8, No. 4, 2000, pp. 660–666.

[117] Lin, Y., Lee, T., Choi, B., and Saravanos, D., "An Application of Smart-Structure Technology to Rotor Blade Tip Vibration Control," *Journal of Vibration and Control*, Vol. 5, 1999, pp. 639–658.

[118] Baz, A. and Poh, S., "Performance of an Active Control System with Piezoelectric Actuators," *Journal of Sound and Vibration*, Vol. 126, No. 2, 1988, pp. 327–343.

[119] Minase, J., Lu, T.-F., Cazzolato, B., and Grainger, S., "A review, supported by experimental results, of voltage, charge and capacitor insertion method for driving piezoelectric actuators," *Precision Engineering*, Vol. 34, No. 4, 2010, pp. 692–700.

[120] Ang, W.-T., Khosla, P., and Riviere, C., "Feedforward Controller With Inverse Rate-Dependent Model for Piezoelectric Actuators in Trajectory-Tracking Applications," *Mechatronics, IEEE/ASME Transactions on*, Vol. 12, No. 2, 2007, pp. 134–142.

[121] Krejci, P. and Kuhnen, K., "Inverse control of systems with hysteresis and creep," *Control Theory and Applications, IEE Proceedings* -, Vol. 148, No. 3, 2001, pp. 185–192.

[122] Jung, H., Shim, J. Y., and Gweon, D., "Tracking control of piezoelectric actuators," *Nanotechnology*, Vol. 12, No. 1, 2001, pp. 14.

[123] Bashash, S. and Jalili, N., "Intelligence rules of hysteresis in the feedforward trajectory control of piezoelectrically-driven nanostagers," *Journal of Micromechanics and Microengineering*, Vol. 17, No. 2, 2007, pp. 342.

[124] Cruz-Hernandez, J. and Hayward, V., "Phase control approach to hysteresis reduction," *Control Systems Technology, IEEE Transactions on*, Vol. 9, No. 1, 2001, pp. 17–26.

[125] Zhong, J. and Yao, B., "Adaptive Robust Precision Motion Control of a Piezoelectric Positioning Stage," *IEEE Transactions on Control Systems Technology*, Vol. 16, No. 5, 2008, pp. 1039–1046.

[126] Liu, Y.-T., Chang, K.-M., and Li, W.-Z., "Model reference adaptive control for a piezo-positioning system," *Precision Engineering*, Vol. 34, No. 1, 2010, pp. 62 – 69.

[127] Shieh, H.-J. and Hsu, C.-H., "An Integrator-Backstepping-Based Dynamic Surface Control Method for a Two-Axis Piezoelectric Micropositioning Stage," *Control Systems Technology, IEEE Transactions on*, Vol. 15, No. 5, 2007, pp. 916–926.

[128] Chang, T. and Sun, X., "Analysis and control of monolithic piezoelectric nano-actuator," *Control Systems Technology, IEEE Transactions on*, Vol. 9, No. 1, 2001, pp. 69–75.

[129] Leang, K. and Devasia, S., "Feedback-Linearized Inverse Feedforward for Creep, Hysteresis, and Vibration Compensation in AFM Piezoactuators," *Control Systems Technology, IEEE Transactions on*, Vol. 15, No. 5, 2007, pp. 927–935.

[130] Aphale, S., Bhikkaji, B., and Moheimani, S. O. R., "Minimizing Scanning Errors in Piezoelectric Stack-Actuated Nanopositioning Platforms," *Nanotechnology, IEEE Transactions on*, Vol. 7, No. 1, 2008, pp. 79–90.

[131] Nijmeijer, H. and Rodriguez-Angeles, A., *Synchronization of Mechanical Systems*, World Scientific Publishing Co. Pte. Ltd., Singapore, 2003.

[132] Shan, J., Liu, H., and Nowotny, S., "Synchronized Trajectory Tracking Control of Multiple 3-DOF Experimental Helicopters," *IEE Proceedings on Control Theory and Applications*, Vol. 152, No. 6, 2005, pp. 683–692.

[133] Liu, H., Shan, J., and Sun, D., "Adaptive Synchronization Control of Mutltiple spacecraft formation flying," *ASME Transactions, Journal of Dynamic Systems, Measurement, and Control*, Vol. 129, No. 3, 2007, pp. 337–342.

[134] Fliegner, T., Logemann, H., and Ryan, E., "Low-gain integral control of continuous-time linear systems subject to input and output nonlinearities," *Automatica*, Vol. 39, 2003, pp. 455–462.

[135] Brokate, M. and Sprekels, J., *Hysteresis and Phase Transitions*, Vol. 121, Springer-Verlag.

[136] Khalil, H., *Nonlinear Systems*, Prentice Hall, New Jersey, 2002.

[137] Armstrong, B., Neevel, D., and Kusik, T., "New results in NPID control: Tracking, integral control, friction compensation and experimental results," *Control Systems Technology, IEEE Transactions on*, Vol. 9, No. 2, 2001, pp. 399–406.

[138] Suykens, J. and Vandewalle, J., "Synchronization Theory for Lur'e Systems: An Overview," 1999.

[139] Wu, C., "Synchronization in arrays of coupled nonlinear systems: passivity, circle criterion, and observer design," *Circuits and Systems I: Fundamental Theory and Applications, IEEE Transactions on*, Vol. 48, No. 10, 2001, pp. 1257–1261.

[140] Oguchi, T. and Nijmeijer, H., "A Synchronization Condition for Coupled Nonlinear Systems with Time-Delay: A Frequency Domain Approach," *International Journal of Bifurcation and Chaos*, Vol. 21, No. 09, 2011, pp. 2525–2538.